Pattern formation during diffusional transformations in the presence of triple junctions and lattice strain: Green's function methods

Von der Fakultät für Mathematik, Informatik und Naturwissenschaften der RWTH Aachen University zur Erlangung des akademischen Grades eines Doktors der Naturwissenschaften genehmigte Dissertation

vorgelegt von

Diplom-Physiker
Claas Hüter

aus Düsseldorf

Berichter: Universitätsprofessor Dr. Heiner Müller-Krumbhaar
Universitätsprofessor Dr. Walter Selke

Tag der mündlichen Prüfung: 8. Juli 2010

Zusammenfassung

Bei Fest-Fest-Phasentransformationen ist die Rolle elastischer Spannungen von offensichtlichem Interesse. Aufgrund der strukturellen Unterschiede der Phasen kommt es zu Gitterverzerrungen, welche zu elastischen Spannungen führen. Im Falle thermisch diffusiver Transformationen ermöglicht die Darstellung in geschlossener Form das Studium der essentiellen Aspekte der Transformation. Im Besonderen bemerken wir neben der fundamentalen Rolle verschiedener Typen strukturbedingter Spannungen für die Selektion asymptotisch dominanter Lösungen an sich auch den entscheidenden Einfluss der relativen Orientierung von Wachstumsrichtung und strukturellen Verzerrungen. Die gefundenen Lösungen zeigen deutlich höhere Transformationsgeschwindigkeiten im Vergleich zum klassischen dendritischen Wachstum.

In eutektoiden Transformationen können bei entsprechenden Keimen isolierte Bidendriten wachsen. Das Wachstumsverhalten dieser Struktur ist bei geringer Unterkühlung der Mutterphase dominant gegenüber dem klassisch dendritischen Wachstum.

Monotektische Transformationen aus entmischter flüssiger Phase zeigen asymmetrisches dendritisches Wachstum der festen Phase entlang der Flüssig-Flüssig Phasengrenze. Neben der dendritschen Selektion der Wachstumsgeschwindigkeit und der Krümmungsradien wird auch die Rotation der Dendritenspitze und die asymptotische laterale Verschiebung der Flüssig-Flüssig Phasengrenze determiniert.

Abstract

Obviously, the effect of elastic stresses in solid-solid transitions is of particular interest. Due to the structural differences of the phases, lattice strains appear, which lead to elastic stresses. The representation of the coupled elastic-thermal diffusional problem in closed form enables the investigation of the transitions essential physics. Specifically, the distinct elastic stresses induce selection of steady-state solutions where the relative orientation of growth direction and lattice strains proves to be of crucial importance. The obtained solutions show that elasticity-induced dendritic selection leads to higher transition velocities than classical dendritic growth.

In eutectoid transitions, twinned isolated dendrites can appear when the initial seed includes both emerging solid phases. At low undercooling of the mother phase, the growth velocity of this pattern is higher than the velocities known from classical dendritic growth.

In the case of monotectic transformations, we study the growth of an asymmetric solid dendrite along the liquid-liquid interface of the decomposed liquid phase. Apart from the dendritic selection of the transition velocity and the radii of curvature, the rotation of the triple junction and the asymptotic lateral shift of the liquid-liquid interface are calculated.

Contents

1 Overview

Since constructions containing steel are ubiquitously present in our day-to-day life, it is just natural to assume that a material of such a broad application is comprisingly understood. Surprisingly, it is not.

Of course, steel as irreplacable construction material must be understood to a certain level, otherwise none of us would find peaceful sleeping. This level of understanding bases on application-oriented knowledge.

Engineers can resort to this vast experience for the construction of various objects. Nevertheless, we still lack predictive models that describe steel behaviour on a fundamental level. When we look at the most important factors contributing to the behaviour of steel, the production process plays an essential role. Obviously, effects take place here which dominate the structure and thus the major physical properties of the material. The patterns which proved important in steel production include wedges, lamellae and dendrites. They mostly appear on microscopic length scales, i.e. micrometers, and form as interface of e.g. a solidification process [3]. Understanding the effects which determine the structure formation constitutes the fundamental challenge in pattern formation.

When we consider the rather general field of pattern formation, the most striking characteristic is its formal similarity of models which describe entirely different phenomena, like the formation of ice and the development of individual animal skins. A first dip into this widespread area of research is provided in [27], where already a large variety of formal aspects of pattern formation is discussed. Both phenomena can be understood as two instances of the so-called Stefan problem. Originally, the Stefan problem described the freezing of ice, and at the end of the 19th century, its foundations were laid out [77], [78]. Formally, a Stefan Problem requires the solution of a diffusion problem which includes boundary conditions on interfaces whose location and temporal evolution is unknown a priori.

The connection between Stefan problems and the production of steel is given by e.g. eutectic, peritectic and monotectic transitions. These three examples involve diffusion of a chemical constituent in a binary mixture, and they play a major role in steel manufacturing. Correspondingly, they have been subject of massive scientific investigation over many years.

Unfortunately, Stefan problems belong to the community of notoriously difficult problems to be solved comprehensively. Though since the 1960s, there is mathematical proof that solutions in three dimensions exist [65], this encouraging knowledge did not lead to an explicit solution of the associated problems.

Among the possible approaches to such diffusion-limited transformations as they occur in steel production, the method of our choice is the Green's function method, also referred to as boundary integral method. In comparison to other modelling techniques, like the phase field method, the great benefits of the Green's function method are its strictness and the concise representation of the nonlocal problem for further analytical treatment.

The Green's function method yields the solution of a nonlinear eigenvalue problem which we

obtain from steady-state formulations of the considered problems. Consequently, the solutions which we obtain correspond to the interface shapes the system exhibit when transients have grown out. The closed formulation which we obtain within this ansatz allows us to investigate fundamental aspects of the transitions without losing the nonlocal aspect of the governing equations.

Applied for analytic approaches, the Green's function method is specifically advantageous because the most influential analytic studies on classical dendritic growth have been conducted in this context[13] - and a common method is obviously helpful to exploit crucial similarities among the considered problems and classical dendritic growth. On various occasions we will take advantage of these similarities, the most striking examples being mappings of a few specific problems to classical dendritic growth.

For numerical investigations, the Green's function method also exhibits several advantages. Since the method reduces the treatment of a volume to the treatment of only the boundary of that volume, the computational expense is minimized, resulting in performant numerical schemes. Another advantage of the Green's function method is the achievable accuracy. Since the obtained equations are integral equations, the numerical scheme leads to higher accuracies compared to explicit PDE solvers.

The Green's function method is the formal basis of the considerations we present within this thesis, and the important physical connection between them is dendritic growth. In dendritic growth, the requirements for the existence of steady-state solutions are known. This knowledge guides the development of the models which we derive, it guides the numerical implementation, and it provides us with valuable nontrivial checks for our obtained results. In conclusion, we state that dendritic growth lays the foundation for the physical understanding of our work, and the Green's function method provides the basis for the formal aspect of our work.

The structure of this thesis reads as follows:

Chapter 2 supplies the necessary background knowledge to access this thesis. The linear theory of elasticity is briefly introduced, along with the required notations. The introduction to dendritic growth comprises the basic model of diffusion-limited growth, the famous Ivantsov solution and an introduction to selection mechanisms. Especially the latter are important to put our calculations in a wider context.

Chapter 3 is the first of the two large result chapters. This chapter is dedicated to thermal-diffusional phase transitions subjected to lattice strains. We distinguish single and bicrystal growth modes on a first level and further discriminate different types of lattice transitions. In addition, the orientation dependence of the transformations and the limiting case of zero transition velocity is investigated.

Chapter 4 is the second large result chapter. It includes our work on transitions which are limited by diffusion of a chemical constituent, where we focus on binary systems. We first recapitulate basics of eutectic growth to become familiar with the topic. Then, we describe the twinned isolated dendrite in eutectoid growth, which is the solid-solid transition analogue to eutectic transitions. It appears in the growth from seeds which contain both emerging phases. Finally, we consider monotectic transitions. In the scenario of a decomposed liquid phase, we investigate the asymmetric dendritic growth of the solid phase along the liquid-liquid interface.

Chapter 5 summarizes the outcome of our work.

2 Introduction

In this chapter, we introduce the subjects which lay the foundation for the systems we discuss within the scope of this thesis.

Section 2.1 provides basic notations for linear elasticity, introduces the Green's tensor of elastostatics and the plain strain configuration.

Section 2.2 includes the concept of lattice strains.

Section 2.3 contains an introduction to dendritic growth, specifically in solidification problems. The dominating effects are explained and basic asymptotic behaviour is discussed.

Section 2.4 presents a few technical points. First, we discuss an established approach within the field of dendritic growth in detail - the Green's function approach in the so-called symmetric model. This extensive study of the symmetric model is suggested as we will apply this type of symmetric model in two of the three systems which we investigate. The second main aspect of that section is selection principles. We will encounter this term quite often in this thesis, thus a few basic insights will prove helpful.

2.1 Linear Elasticity

We consider a solid body which is deformed due to some external force $\vec{F}^{ext}$. The deformation can be described by the change of position of every point in the body due to the external force. Be

$$\vec{u} = \vec{x}\,' - \vec{x} \tag{2.1}$$

the *displacement* belonging to point $\vec{x}$, meaning that the deformation is the shift of the bodypoint $\vec{x}$ to $\vec{x}\,'$. Of course, $\vec{u}$ is depending on $\vec{x}$, and knowing the displacement $\vec{u}$ as function of the position $\vec{x}$, the deformation is described completely by $\vec{u}(\vec{x})$.

Often it is preferred to discuss elastic problems in terms of strains instead of displacements. To describe the strain of the body, the symmetric strain tensor u_{ik} is defined,

$$u_{ik} = \frac{1}{2}\left(\frac{\partial u_i}{\partial x_k} + \frac{\partial u_k}{\partial x_i}\right), \tag{2.2}$$

it suffices to take only the first order derivations of the displacement into account, as we consider small distortions in general.

The formal requirements for this change of variables are represented by the Saint-Venant compatibility conditions:

$$\frac{\partial^2 u_{ij}}{\partial x_k \partial x_l} + \frac{\partial^2 u_{kl}}{\partial x_i \partial x_j} = \frac{\partial^2 u_{ik}}{\partial x_j \partial x_l} + \frac{\partial^2 u_{jl}}{\partial x_i \partial x_k}. \tag{2.3}$$

Apart from this linearization of the strain in Eq. (2.2), the linear relations of strains and stresses

state the second important approximation which our calculations are subjected to. These linear relations, known as Hooke's law, read for isotropic elasticity as

$$\sigma_{ij} = \frac{E}{1+\nu}\left(u_{ij} + \frac{\nu}{1-2\nu}\delta_{ij}u_{kk}\right) \tag{2.4}$$

$$u_{ij} = \frac{1}{E}[(1+\nu)\sigma_{ij} - \nu\delta_{ij}\sigma_{kk}], \tag{2.5}$$

in a more compact form also expressed as

$$u_{ij} = s_{ijkl}\sigma_{kl}, \tag{2.6}$$

$$\sigma_{ij} = c_{ijkl}u_{kl}. \tag{2.7}$$

The tensors of 4th order here are the tensors of elastic compliances (or elastic moduli) s_{ijkl} and elastic stiffness (or elastic coefficients) c_{ijkl}. We denote the elastic constants E, the modulus of elasticity, and ν, the Poisson ratio of tranverse contraction. It requires only these two elastic coefficients here since we will restrict ourselves to isotropic systems.

The stresses σ_{ik}, specifically the definition of the spatial indices, are illustrated in Fig. 2.1.

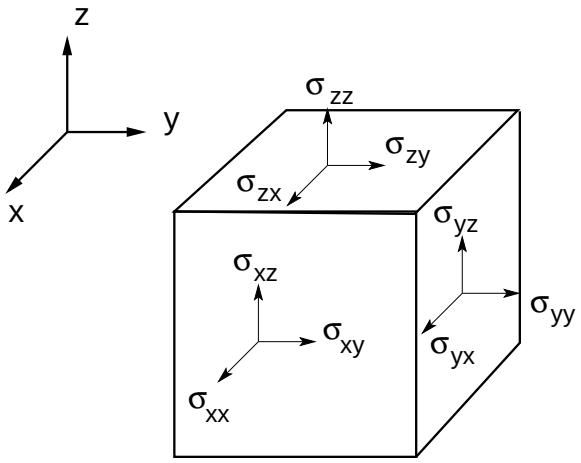

Figure 2.1: Illustration of the elastic stresses σ_{ik}.

Next, we introduce the equation of motion,

$$\frac{\partial\sigma_{ik}}{\partial x_j} + F_i^{ext} = \rho\frac{d^2u_i}{dt^2}, \tag{2.8}$$

where ρ is the mass density of the concerned body and F_i^{ext} an external force density. For the elastostatic regime which we will consider, it remains

$$\frac{\partial\sigma_{ik}}{\partial x_j} + F_i^{ext} = 0. \tag{2.9}$$

The boundary conditions for the elastic problem prescribe the displacements $\vec{u}$ or the stresses σ_{ik}. Usually, the type $\vec{u}_{|\partial V} = \vec{b}$ is labelled *fixed boundary condition*, the type $(\sigma_{ik}n_k)_{|\partial V} = P_i$ is labelled

open boundary condition, where $\vec{b}$ is the boundary displacement and P_i is a pressure. The special case $\vec{P} = 0$ is called *free boundary condition* or *free surface condition*.

Up to here, we presented the necessary equations and quantities which allow to define an elastic problem. As well, it becomes clear that the solution of such a problem will be quite challenging - if we consider Eqs. (2.9) and (2.6), we see that we are confronted with a system of coupled PDEs. For a rigorous and detailed analytic study of various specific elastic problems, we recommend [61] and [49].

In the range of this thesis, we will incorporate elastic effects by means of the Green's function technique, thus we introduce the Green's tensor of elastostatics and give only a brief example of a simple elastic problem afterwards.

2.1.1 Green's Tensor for Elastostatics

We present the Green's tensor of the 3D elastostatic isotropic problem, a reference for the detailed derivation is given at the end of this paragraph. Though isotropic elasticity suffices for the calculations which we perform within this thesis, it is also of interest for us to which effort we would need to go for the anisotropic elastic problems.

The governing equation for the elastostatic isotropic case without applied forces reads as

$$\frac{\partial \sigma_{ik}}{\partial x_k} = 0, \tag{2.10}$$

and in terms of the displacement field one obtains

$$\triangle \vec{u} + \frac{1}{1-2\nu} \vec{\nabla}(\vec{\nabla}\vec{u}) = 0, \tag{2.11}$$

where $\vec{\nabla}(\vec{\nabla}\vec{u}) = \triangle\vec{u} + \vec{\nabla} \times \vec{\nabla} \times \vec{u}$. The solution of the corresponding equation for the Green's Tensor,

$$\triangle \vec{u} + \frac{1}{1-2\nu} \vec{\nabla}(\vec{\nabla}\vec{u}) = -\frac{2(1+\nu)}{E} \vec{F}\delta(\vec{r}), \tag{2.12}$$

defines it as

$$g_{ik} = \frac{1+\nu}{8\pi(1-\nu)} \frac{1}{r} [(3-4\nu)\delta_{ik} + n_i n_k]. \tag{2.13}$$

A derivation of Eq. (2.13) is given in [49]. The Green's tensor at hands, the formal solution of the displacement, $\vec{u}$ can be written in a compact way as

$$u_i^{(\alpha)} = \int_{\partial V} d f' g_{ik}(\vec{r} - \vec{r}') F_k(\vec{r}'), \tag{2.14}$$

Here F_k is the k-component of a force surface density $F(\vec{r})$.

The introduced Green's Tensor is valid for isotropic elasticity, and few special cases can be obtained e.g. from [49] for crystals which exhibit anisotropic elasticity. However, within this thesis, we will not need the displacements but the strains, i.e. the derivatives of the displacements. Referring to [6, 56], the derivatives of the Green's Tensor can be obtained for arbitrary anisotropy. Though this reads promising, it turns out that the specific analytic calculation of Green's Tensors

for arbitrary anisotropy become enormously demanding and thus for most applications, numerical estimations are used.

2.1.2 Simple example: Stretching of a Bar

A brief example illustrates the meaning of a few of the just introduced elastic quantities. We consider the stretching of a bar, see Fig. 2.2.

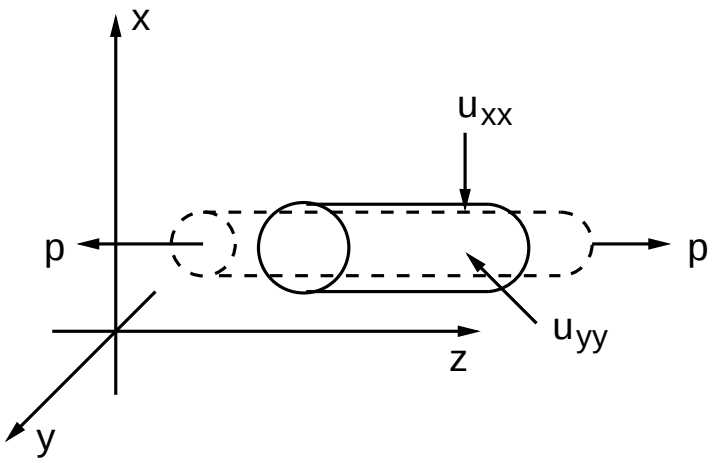

Figure 2.2: Stretching of a bar in z-direction. At the ends, stresses $\sigma_{zz} = p$ are applied, stretching the bar as $u_{zz} = p/E$ in z-direction. The transverse contraction is determined as $u_{xx} = u_{yy} = -\nu u_{zz}$.

Assume the bar is parallel to the z-axis, and at its ends are pulling forces which intend to stretch it and that affect the surfaces of the ends homogeneously, the forcing at the surface unit denoted as p. The sides of the bar are unaffected by any forcing, thus the stress tensor is $\sigma_{ik} = 0$ except of σ_{zz}, which is given as $\sigma_{zz} = p$. Using Hooke's law, one obtains $u_{zz} = p/E$, giving the stretching of the bar by the modulus of elasticity E, and $u_{xx} = u_{yy} = -\nu u_{zz}$, giving the tranverse contraction of the bar by the Poisson ratio of transverse contraction ν.

2.1.3 Plain Strain

The elastic problem of a body can be reduced effectively to two dimensions if one component of the displacement vector, e.g. u_z, vanishes and u_x, u_y only depend on x, y. This means the plain strain is in the xy plane, and thus the stress tensor is simplified as

$$\sigma_{xz} = 0 \tag{2.15}$$

$$\sigma_{yz} = 0 \tag{2.16}$$

$$\sigma_{zz} = \frac{\nu E}{(1+\nu)(1-2\nu)}(u_{xx} + u_{yy}). \tag{2.17}$$

From the equations of motion,

$$\frac{\partial \sigma_{ik}}{x_k} + F_i = \rho \frac{d^2 u_i}{dt^2}, \tag{2.18}$$

where we denote the volume force density by F_i, we obtain

$$\frac{\partial \sigma_{xx}}{\partial x} + \frac{\partial \sigma_{xy}}{\partial y} = 0 \tag{2.19}$$

$$\frac{\partial \sigma_{xy}}{\partial x} + \frac{\partial \sigma_{yy}}{\partial y} = 0, \tag{2.20}$$

when we consider the static case in absence of volume forces.

Apart from the equations of motion, in plain strain also the illustration of the strain tensor becomes easier. We give examples for three modes of deformation in plain strain [4]. Here the corresponding strain tensors are given as

$$\begin{pmatrix} u_{xx} & 0 & 0 \\ 0 & 0 & 0 \\ 0 & 0 & 0 \end{pmatrix} \tag{2.21}$$

for the simple elongation, see Fig. 2.3.

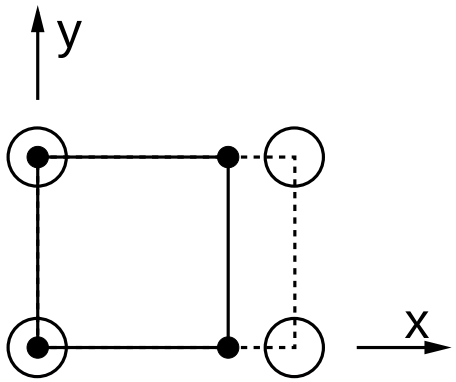

Figure 2.3: The simple elongation in x - direction, corresponding to Eq. (2.21). The massive black dots indicate the undeformed lattice, the empty circles the deformed lattice.

For a volume preserving pure shear strain, i.e. $\nabla \vec{u} = 0$, the tensor takes the form

$$\begin{pmatrix} u_{xx} & 0 & 0 \\ 0 & -u_{xx} & 0 \\ 0 & 0 & 0 \end{pmatrix} \tag{2.22}$$

and this case is illustrated in Fig. 2.4.

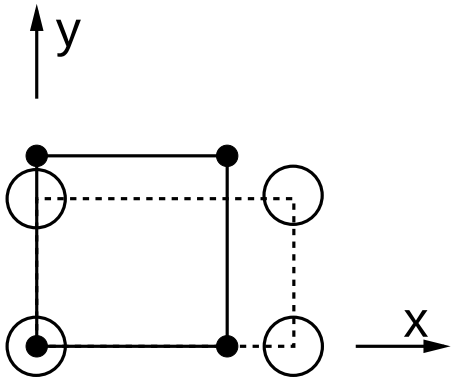

Figure 2.4: Belongs to (2.22): pure shear strain,the volume is preserved.

$$\begin{pmatrix} 0 & u_{xy} & 0 \\ 0 & 0 & 0 \\ 0 & 0 & 0 \end{pmatrix} \tag{2.23}$$

As an example of a nonsymmetric strain, the geometric meaning of tensor (2.23) is given in Fig. 2.5. It can be obtained as a symmetric pure shear associated with a rotation around the *z*-axis.

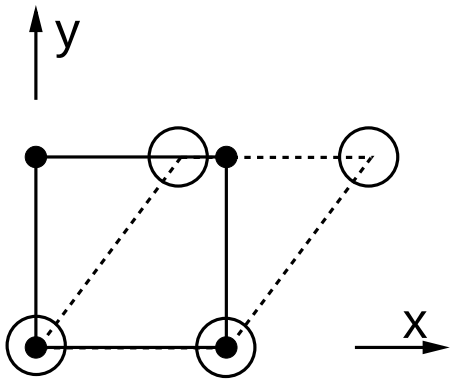

Figure 2.5: The strain is asymmetric - the x-component of the body points is changed as $u_{xy} \neq 0$, but the y-component remains unchanged as $u_{yx} = 0$.

The aforementioned strains constitute the basic 2D deformations a body can undergo. We will restrict to dicussions to symmetric strains within the scope of this thesis, and the superposition of the introduced basic deformations covers all considered cases.

2.2 Eigenstrain and Elastic Hysteresis

If no elastic forces are applied to a body, but a remaining strain is present, this is called *eigenstrain*. In analogy to ferromagnetism or ferroelectricity, the presence of eigenstrains is often named ferroelasticity. This analogy must be used cautiously, as the presence of eigenstrain only leads to a

hysteresis in phase transitions if these exhibit a coherent phase interface, see [20].

Eigenstrains can occur when a structural transition takes place. Here, the simplest example of an eigenstrain one can imagine is the uniform stretching of a simple cubic crystal with the lattice constant a , $a \to a'$. Then the eigenstrain is be $\epsilon_{ik} = \delta_{ik}(a' - a)/a$.

An example of a transition which occurs in a concrete system is given in [31]. Here, a hexagonal-orthorhombic transition is discussed. The change of the crystal shape is illustrated in Fig. 2.6.

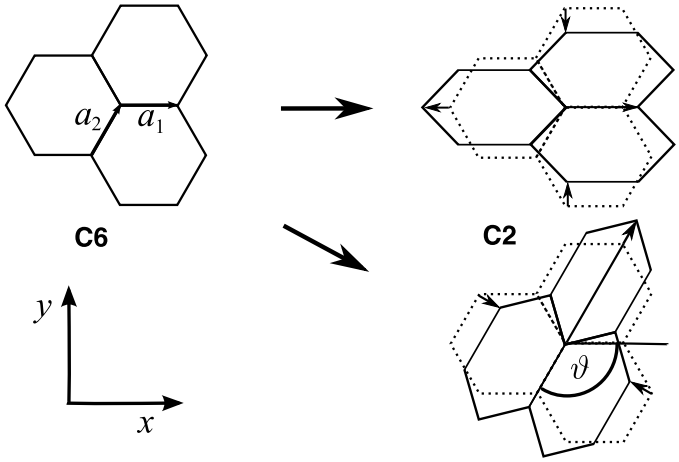

Figure 2.6: Schematic picture of the structure transition as discussed in [31]. The hexagonal lattice transforms to a hexagonal-orthorhombic lattice, which lowers the symmetry as $C_6 \mapsto C_2$. This fixes the possible angles as $\vartheta = 0, \pm 2\pi/3$.

To simplify the problem, we assume the crystal to be fixed between two parallel plates. We set the z-direction as the principal C_6-axis. Consequently, we obtain by proper choice of the orientation around the main axis in the hexagonal phase three possible states, due to the lowering of the symmetry $C_6 \mapsto C_2$. The used notations C_2, C_6 of the rotational groups indicate the counting of the rotational symmetry, meaning that the considered crystal is invariant under rotations around the principal C_i-axis by $n \cdot 2\pi/i$, n being a natural number. The eigenstrains of the system are then defined as $\epsilon_{xx} = -\epsilon \cos 2\vartheta$, $\epsilon_{yy} = \epsilon \cos 2\vartheta$, $\epsilon_{zz} = 0$ and $\epsilon_{xy} = -\epsilon \sin 2\vartheta$. Here we introduced the magnitude of the eigenstrain ϵ. Now that we illustrated the formal representation of the eigenstrains, we consider the free energy densities in a transition with eigenstrain.

2.2.1 Thermodynamic Effects of Lattice Strains

We consider the influence of lattice strains on the state of a system, represented in terms of thermodynamic potentials. First, we define the work in a system due to elastic deformation in the introduced linear limit.

$$\int \delta R dV = \int \frac{\partial \sigma_{ik}}{\partial x_k} \delta u_i dV \tag{2.24}$$

$$\int \delta R dV = -\frac{1}{2} \int \sigma_{ik} \delta \left(\frac{\partial u_i}{\partial x_k} + \frac{\partial u_k}{\partial x_i} dV \right) = - \int \sigma_{ik} \delta u_{ik} dV \tag{2.25}$$

Consequently, the free energy and the stress tensor are related as

$$dF = -S\,dT + \sigma_{ik}du_{ik} \tag{2.26}$$

$$\sigma_{ik} = \left(\frac{\partial F}{\partial u_{ik}}\right)_T \tag{2.27}$$

We denote the reference phase without eigenstrain as phase (α) and the onsetting phase with eigenstrain ϵ_{ik} as phase (β). Then, we obtain for phase (α)

$$F_\alpha = F_\alpha^0(T) + \frac{E_\alpha}{2(1+\nu_\alpha)}\left(\frac{\nu_\alpha}{1-2\nu_\alpha}\left(u_{ii}^{(\alpha)}\right)^2 + \left(u_{ik}^{(\alpha)}\right)^2\right), \tag{2.28}$$

and for the new phase (β)

$$F_\beta = F_\beta^0(T) + \frac{E_\beta}{2(1+\nu_\beta)}\left(\frac{\nu_\beta}{1-2\nu_\beta}\left(u_{ii}^{(\beta)} - \epsilon_{ii}\right)^2 + \left(u_{ik}^{(\beta)} - \epsilon_{ik}\right)^2\right). \tag{2.29}$$

The elastic coefficients are E_i, the elastic modulus, and ν_i, the Poisson ratio, and we denote the free energy density without elastic effects by $F_i^0(T), i = \alpha,\beta$. Obviously, the representation of the free energy is chosen here such that it is most convenient to consider the elastic effects. Since the stresses σ_{ik} can be understood as reaction of the system to deformations characterized by the strains u_{ik}, the application of Eqs. (2.26) to (2.29) should show how the stresses depend on the lattice strains. We define

$$\sigma_{ik}^{(\beta)} = \tilde{\sigma}_{ik}^{(\beta)} - \sigma_{ik}^{\epsilon(\beta)}, \tag{2.30}$$

where we discriminate those stresses independent of the lattice strains, labelled $\tilde{\sigma}_{ik}^{(\beta)}$, and the stresses corresponding strictly to the lattice strains, labelled $\sigma_{ik}^{\epsilon(\beta)}$. Consequently, we obtain for the stresses which depend restrictively on the lattice strains

$$\sigma_{ik}^{\epsilon(\beta)} = \frac{E}{1+\nu}\left(\epsilon_{ik} + \frac{\nu}{1-2\nu}\delta_{ik}\epsilon_{ik}\right). \tag{2.31}$$

The separability of the stresses which is reflected in Eq. (2.31) is in accordance with Hooke's law, Eq. (2.4). Eigenstrains can lead to an elastic hysteresis, if the phase interface is coherent [20]. We restrict our considerations to the cases of small distortions, which suggests that we may assume coherency of the interfaces, $u_i^{(\alpha)} = u_i^{(\beta)}$. The appropriate thermodynamical potential for the transition with coherent interface is obtained by a Legendre transformation from the free energy [70]. This modified free energy reads as

$$\tilde{F}_i = F_i - \sigma_{nn}^{(i)}u_{nn}^{(i)} - 2\sigma_{n\tau}^{(i)}u_{n\tau}^{(i)}, \tag{2.32}$$

where by n and τ we denote the normal and tangential coordinates in the local coordinate system, $i = \alpha,\beta$ indicate the phase. This potential is also discussed in [75], and an illustrative example for a planar interface is given in [76]. Briefly said, a system which obeys Eq. (2.32) can show a growth of the phase with higher elastic energy at cost of the phase with lower elastic energy, as the normal and shear contributions enter with negative sign.

2.3 Dendritic Growth

In this section, we give a short introduction to the topic of diffusional phase transitions, specifically solidification, to set up an appropriate basis for the subsequent discussions in the next sections.

We consider a diffusional phase transition when diffusion is the limiting process of the transition. The diffusing quantity either is a chemical component or heat, thus one would obtain diffusion equations for concentration fields or temperature fields as governing equation in the involved phases. For solidification of a pure undercooled melt, we consider heat diffusion as governing process. Before we represent the problem in formal detail, we first discuss two opposing effects which are crucial for the interface formation. The interfaces which we consider belong to the growth of a protuberance of the growing phase and we exclude the initial growth phase of the seed in our subsequent calculations. Namely, these two opposing effects are the Mullins-Sekerka instability and the Gibbs-Thomson effect.

2.3.1 Competing Effects: Mullins-Sekerka Instability vs. Gibbs-Thomson Effect

The Mullins-Sekerka instability effects the shape of the interface such that it lets protrusions grow [59, 60]. A protrusion in growth direction leads to an increase of the thermal gradient in front of that bulge, such that the local heat flow is increased - the protrusion grows further. The compression of the isotermals is illustrated in Fig. 2.7.

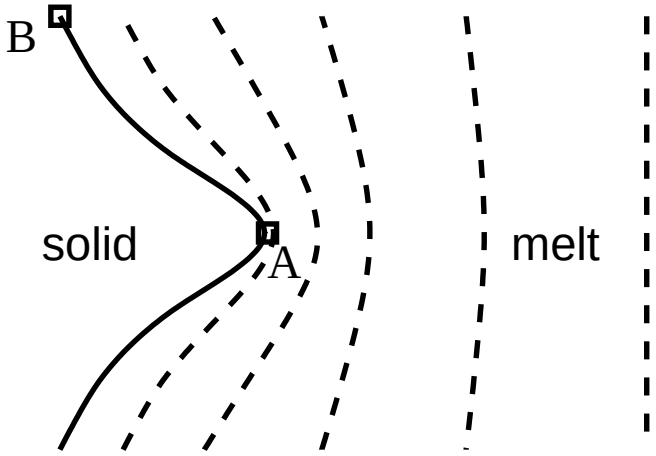

Figure 2.7: The Mullins-Sekerka instability. By the solid line, the interface is indicated, the dashed lines are the isothermals in front of the interface. The solid phase grows at expense of the melt. At point A in the sketch, the interface forms a bulge. This leads to an increase of the thermal gradient in front of the bulge, as the distance between the isothermals is reduced. Consequently, the diffusion of heat at point A is larger than at point B - the bulge will grow.

The growth of a stable interface thus requires a stabilizing effect. The Gibbs-Thomson effect reduces the interface temperature due to surface tension - the magnitude of the effect grows when the bulges become sharper. Denoting the surface tension by γ and the curvature by κ, the shift

scales as $\sim \gamma\kappa$. A schematic sketch of the Gibbs-Thomson effect versus the Mullins-Sekerka instability is given in Fig. 2.8.

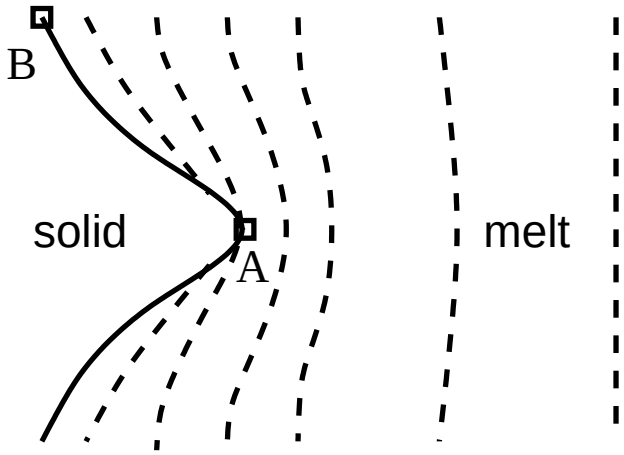

Figure 2.8: The Mullins-Sekerka instability with counteracting Gibbs-Thomson effect. By the solid line, the interface is indicated, the dashed lines are the isothermals in front of the interface. The growth direction points from the solid into the melt. At point *A* in the sketch, the interface forms a bulge. This leads to an increase of the thermal gradient in front of *A*, but the Gibbs-Thomson effect decreases the temperature on the interface such that the interface breaks the isothermals. Consequently, the change of the temperature gradients due to the protrusion is reduced.

To understand the Gibbs-Thomson effect, consider the interface on the molecular scale. The molecules of a planar interface have some typical number of nearest neighbour interactions. At equilibrium, there is a balance between new molecules included and molecules which are lost due to collisions. A curvature bump into the growth direction has its boundary molecules exposed, with less nearest neighbour interaction, and they are more susceptible to break out the lattice. At a temperature when the planar interface is in equilibrium a protrusion will melt back - the melting temperature of a protrusion is decreased. Conversely, on a negative curvature the boundary molecules have more nearest neighbours and consequently an increased binding. In effect, the melting temperature goes up.

The balance between Mullins-Sekerka instability and Gibbs-Thomson effect sets the length scale of the onsetting pattern. The Gibbs-Thomson effect introduces the capillarity length $d \sim \gamma$, and the Mullins-Sekerka instability introduces the diffusion length l_D, which determines the decay of a diffusion field.

The resulting length scale R behaves as $R \sim \sqrt{dl_D}$, which is suggested as taking the root of the product is the only combination which does not drastically prefer one lengthscale due to the different orders of magnitude they have. Consequently, as $l_D = 2D/\upsilon$, where υ is the growth velocity, the velocity then can be determined as $R^2\upsilon = const$. We shall find this assumption to be verified later in this thesis. We will encounter it represented as $dl_D/R^2 = const$, and the calculation of this constant turns out to be the main goal in the problem.

2.3.2 Free Boundary Problem

Definition of Free and Moving Boundary Problem

Prior to the subsequent discussion of systems which can be represented as moving boundary problem, we distinguish moving and free boundary problems as they are occasionally mixed up in literature.

We refer to [28, 29], a Free Boundary Problem (FBP) may be defined as a steady-state boundary value problem, which has to be solved in a domain, parts of whose boundaries, the free boundaries, are unknown and must be determined as part of the solution.

A Moving Boundary Problem (MBP) may be defined as a non-stationary or time-dependent boundary value problem, which has to be solved in a time-dependent space domain with moving boundaries. Specifically, moving boundary problems which are governed by a diffusion equation are called Stefan Problems.

Since the free or moving boundary has to be determined as part of the solution such problems are inherently non-linear.

Free Boundary Problem of Dendritic Growth

The aforementioned competition of the Mullins-Sekerka instability and the Gibbs-Thomson effect requires the inclusion of a curvature-dependent term, which is nonlinear in terms of the interface. The unknown position of the interface already renders the governing equation system inherently nonlinear even without the stabilizing influence of the surface tension. To support the subsequent consideration of this complicated free boundary problem, we shall briefly describe the basic physics which determines the solidification process, and present solutions for two special cases. We mention that the term 'free boundary problem' is briefly defined in the appendix, see 2.3.2.

When the solid grows in expense of the undercooled melt, the transition sets free the latent heat of the specific material. This heat must be transported away from the interface - if not, the just solidified area would melt back. Consequently, the propagation of the interface is limited by the transport of the latent heat set free. This condition of heat conservation sets the free boundary condition, determining the local interface velocity in dependence on the local gradient jumps of the temperature - which state the heat flow that is the transported latent heat.

The governing equations of the transport thus include a diffusion equation in each phase, the free boundary condition, and a yet unstated condition about the temperature at the interface. We refer here to the capillarity-limited growth with negligible kinetic effects, i.e. the interface temperature is the equilibrium transition temperature to a correction due to surface tension, the Gibbs-Thomson effect.

One could now try to solve the entire free boundary problem, which demands the solution of the temperature field and the interface. However, Kolodner developed the 'reduction' of the one-phase Stefan problem, see [47], which formally is close to our problem - the term Stefan problem originates to Stefan's studies on the freezing of ice [77, 78], it was transferred to model various diffusional phase transitions. A seminal book about the Stefan problem is [71].

Kolodner derived an integral equation for the interface. This reduction technique was transferred to the two phase problem, but within this introduction we will restrict ourselves to the so-called symmetric model. Here symmetry implies equal diffusion constants in both phases. Though this assumption demands some critical assessment, it simply turned out that the general asymmetric

case exhibits various additional difficulties, even if only steady-state solutions are subject of interest. The formal complexity of steady-state as well as dynamical case in the asymmetric model is easily recognized in [62].

Before we discuss the symmetric model, two specific scenarios for the solidification of an undercooled melt are worth some attention. Namely, the planar interface, be it the easiest geometry to consider, and the Ivantsov solution [38], which is a milestone in this topic.

Planar Interface

The first specific geometry is a planar front - for our purpose, it suffices to show that a planar interface moves at decreasing velocity, except for the case of unit undercooling. The dimensionless representation of the temperature is

$$u = c_p \frac{T - T_\infty}{L}, \tag{2.33}$$

where the control temperature T_∞ is applied in the melt infinitely far away from the interface. By c_p we denote the heat capacity, by L the latent heat per unit volume. The dimensionless undercooling reads as

$$\Delta = c_p \frac{T_M - T_\infty}{L}, \tag{2.34}$$

where T_M is the melting temperature. Unit undercooling is the limit of the validity of the diffusion-limited model of solidification, we mention that for unit undercooling $\Delta = 1$, the planar interface moves at a constant velocity.

For $\Delta < 1$, we determine the time-dependence of the interface velocity. When the planar interface moves into y-direction, with velocity υ, the diffusion equation reads as

$$D\frac{d^2u}{dy^2} = \frac{\partial u}{\partial t}, \tag{2.35}$$

and $u = 0$ in the melt far away from the interface. Here D is the thermal diffusion constant. A transformation to state the convenient ansatz $u(y,t) = \tilde{u}(w)$ is introduced by

$$w = \frac{y}{\xi(t)}, \tag{2.36}$$

where $\xi(t)$ is the position of the interface at time t. From Eq. (2.35) we obtain

$$\frac{\xi\dot{\xi}}{D} = -\frac{\frac{d^2\tilde{u}}{dw^2}}{w\frac{d\tilde{u}}{dw}} = \text{ const} = \text{C}, \tag{2.37}$$

where the l.h.s. of equation (2.37) is only time dependent and the right hand side only depending on w, thus

$$\frac{\xi\dot{\xi}}{D} = C, \tag{2.38}$$

the position of the interface, $\xi(t)$, depends on time as $\xi(t) \sim t^{1/2}$. The corresponding decrease of the propagation velocity, $\upsilon \sim t^{-1/2}$, can be understood as an accumulation of a melt layer of increasing thickness in front of the interface.

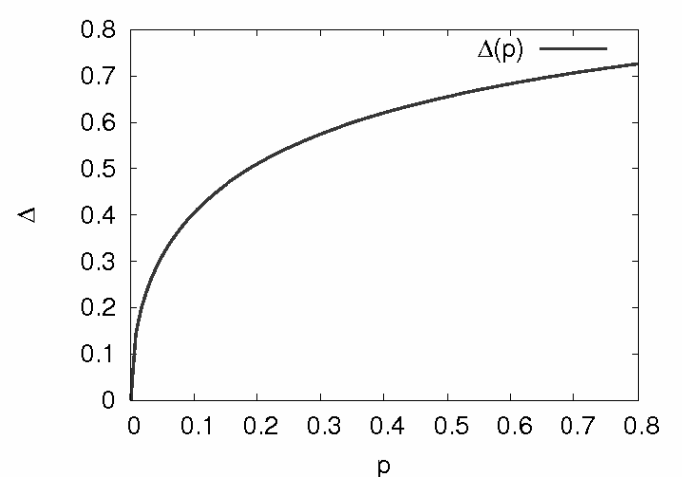

Figure 2.9: The undercooling Δ in dependence of the Peclet number p. Asymptotically, $\Delta \to 1$ for $p \to \infty$, which marks the limit of the diffusional regime of the transition.

Ivantsov Solution

We briefly introduce the Ivantsov solution for solidification, which Ivantsov found [38] when he assumed that the interface was isothermal at melting temperature T_M. He determined families of parabolas to be the solutions, which grow with time t as $y = \upsilon t - x^2/2R$ where (x, y) is the tip position, υ is the constant growth velocity along the y-axis and R denotes the radius of curvature of the tip.

The outcome was the Ivantsov relation for two and three dimensions,

$$\Delta = \sqrt{\pi p} e^p erfc\ \sqrt{p}, \tag{2.39}$$

in 2D, where *erfc* is the inverse errorfunction, and for three dimensions,

$$\Delta = pe^p E_1(p) = pe^p \int_R^\infty d\eta \eta^{-1} e^{-\eta/l_D}, \tag{2.40}$$

where E_1 is the exponential integral function and l_D is the diffusion length. By $p = R\upsilon/2D$ the Peclet number is defined, which is an implicit function of the undercooling Δ, see Fig. 2.9. The Peclet number sets only the product of growth velocity and radius, leaving the solution degenerate. This corresponds to the aforementioned necessity of a second lengthscale in the system.

Asymptotic Growth Behaviour

Assume we have steady-state solution, with a lengthscale selected by the interplay of Gibbs-Thomson effect and Mullins-Sekerka instability. The crystal grows into y-direction with growth velocity υ. When we consider the tail region of the crystal, this part asymptotically approaches a planar interface. For the steady state solution, the position of the interface, $\xi(x, t)$, depends on time like

$$\xi(x, t) = \xi(x) + \upsilon t, \tag{2.41}$$

at the tip specifically

$$\xi(x,t) = \upsilon t. \tag{2.42}$$

In the asymptotic region far away from the tip, the interface is approximatly planar, and as discussed in the previous paragraph, the planar interface $x(t)$ behaves like

$$x(t) \sim (Dt)^{1/2}. \tag{2.43}$$

Consequently, the asymptotic growth is related to the tip propagation as

$$\xi \sim \frac{\upsilon}{D} x^2. \tag{2.44}$$

The outcome of this handwaving calculation in form of Eq. (2.44) will serve as basis for the examination of the asymptotic behaviour the solutions exhibit which we calculate in the next chapters.

2.3.3 Short Retrospective on Dendritic Growth

We gave the basic ingredients for the solidification problem in the previous part of this section. The solidification process as we introduce it belongs to the field of dendritic growth, and we give now a short view on its development.

The growing crystal is expected to take a shape that exhibits the most efficient transport of the released latent heat. The investigation of this dominant shape was boosted by Ivantsov in 1947 when he partially solved the problem [38], determining the product of growth velocity and tip radius of curvature. However, the degeneracy of the solution predicted by Ivantsov remained a mystery. Experiments suggested that the growth velocity and tip radius were selected uniquely for a given undercooling. The inclusion of capillarity, as suggested by Temkin for example [80], turned out to solve the degeneracy problem, in principle. Unfortunately, implementing surface tension requires the solution of an analytically quite intractable problem, as the Gibbs-Thomson effect introduces an additional nonlinearity.

These difficulties gave rise to models which neglect the nonlocal interactions on the boundary, among them the geometrical model [21, 22, 46, 44]. The fundamental assumption there was the proportionality of the growth velocity to the curvature of the interface. Already this approach yields the existence of the so-called needle crystal solution, but it is unstable against infinitely small perturbations, and isotropic surface tension destroys the solutions.

To extend the geometrical model, the boundary layer model (BLM) incorporated a term to mimic the heat diffusion along the boundary to approximate non-local effects. Here the boundary layer is a regime of width l_D in front of the phase boundary, and the diffusion length l_D is assumed to be small, which restricts the model to high undercoolings. Furthermore, the BLM is expressed in the natural coordinates of the interface, averting the application to interfaces which do exhibit a complex structure, as higher order sidebranched dendrites. The boundary layer model was mainly developed in 1983 and 1984 by Ben-Jacob, Langer, Goldenfeld, Schon and Kotliar [24, 9], and it could also predict needle crystal solutions when the capillarity length is set to zero. Specifically, the BLM revealed the dependence of the solvability of the problem on the anisotropy of the surface tension [24], which turned out to be the crucial ingredient.

In the framework of nonlocal models, the representation as boundary integral equation leads

to the solution of a 'nonlinear' eigenvalue problem. Here the term 'nonlinear eigenvalue' was defined in the sense of Barenblatt and Zeldovich, see [5]. We emphasize the so-called marginal stability hypothesis [54], it was the first scaling analysis of dendritic growth. Langer and Müller-Krumbhaar hypothesized that dendrites grow at the margin of stability, and they suggested that the tip radius matches a critical wavelength λ_c. With Ivantsov's solution and the condition for morphological stability, they showed that $\lambda_c \sim \sqrt{l_D d}$, with thermal diffusion length l_D and the capillary length d. Consequently, by matching of the critical wavelength and the operating tip radius they obtained $\sigma := 2Dd/\upsilon R^2$, where σ is theoretically $\sigma = 0.0025$. We recognize that this so-called solvability parameter is the constant we introduced at the end of subsection 2.3.1. Experiments with succonitrile [34] supported this interpretation, though the assumption of growth at marginal stability finally turned out to be wrong.

Also, the integral equation was investigated for small magnitudes of anisotropy of the surface tension by means of perturbation techniques. As the curvature-dependent term contains the derivative of highest order, singular perturbation methods [81, 37, 10] need to be applied. Seminal lectures to singular perturbation theory are found in [81, 37, 10]. Among perturbation approaches, the method that turned out to become a cornerstone of the solution was developed by Kruskal and Segur, see [48]. In contrast to other linearizing approaches, they treated the problem in its entire nonlinearity, an introduction can be found in [12]. As already indicated by the boundary layer model, the necessity of anisotropy of the surface tension was revealed. For the three dimensional system, Brener and Ben Amar [7] derived the behaviour of the needle crystal in the tip region, and Brener [13] found the analytic solution for the entire interface in 1993 in the axisymmetric case.

One can alternatively introduce an additional degree of freedom which represents the phase state of the system [23, 32] to avoid the solution of the closed representation as highly nonlinear integral equation. This phase field changes from minimum to maximum on a length scale which thus models the transition with an interface of finite thickness. The phase field model does not need to track the interface positions explicitly, which is hard to do for complicated topologies, but for the cost of an increased computational expense; the numerical separation of this new lengthscale and the other length scales drastically increases the required number of grid points. The legitimacy of the phase-field model was proven when the limit of vanishing interface thickness and sharp-interface calculations were found to coincide, [32]. Specifically for liquid-solid transitions, the phase field model was mainly developed in the works of Fix [33], Langer [50] and Collins and Levine [25].

We want to stress the stability of the found solutions versus external fluctuations. In 1994, Müller-Krumbhaar, Brener, Ihle, Saito and Shiraishi [14] found that the dendrites were stable already for small magnitudes of anisotropy. Their analytic considerations for sidebranching in the three dimensional model predict the experimentally observed amplitudes of sidebranching. For the nonaxisymmetric case, this model in was published in 1994 by Brener and Temkin [15].

Finally, we make some remarks about the outcome of experiments in dendritic growth - for crystallization of an undercooled pure melt, we mention the experiments conducted with succonitrile (SCN). This material proved its merit for the experiments as it is chemically stable and close to identical diffusion constants in both phases. Also, heat transport occurs nearly exclusively via heat diffusion in SCN. A result of the experiments performed by Huang and Glicksman [35] in 1981 is shown in Fig. 2.10.

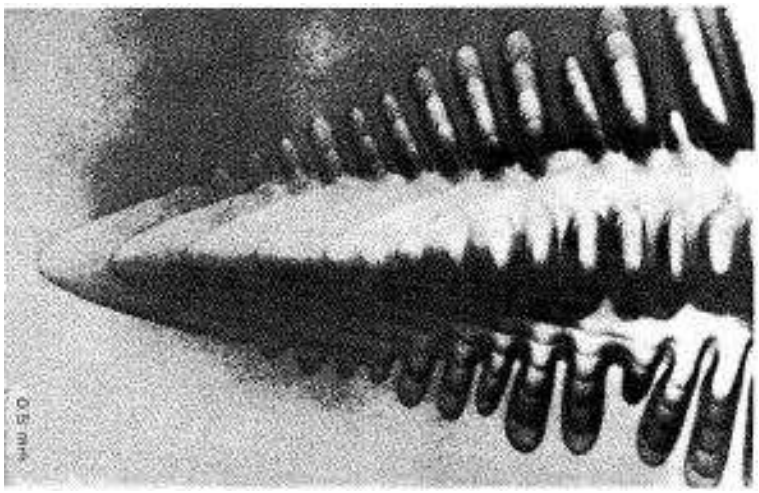

Figure 2.10: Time-exposure sequence of SCN [35]. The interface propagates at constant velocity, and secondary dendrites are nicely to see.

2.4 Green's Function Technique: The Symmetric Model

In the previous subsection, we gave a short overview of the development of the approaches to solidification , now we are only interested in one specific formulation. The formulation of the governing equations as integro-differential equation via Green's functions has proven to be a promising ansatz. Probably the most influential advances in this field have been made with application of this technique, at least in the last twenty years. For a full load of formal requirements for the derivations in this thesis, see e.g. [2] and [71].

The diffusion equations for both phases reads as

$$D^{(l)}\frac{\partial T^{(l)}}{\partial t} = \nabla^2 T^{(l)}, \tag{2.45}$$

$$D^{(s)}\frac{\partial T^{(s)}}{\partial t} = \nabla^2 T^{(s)}, \tag{2.46}$$

here we indicate the solid phase by s, the liquid phase by l. The temperature in the melt far away from the interface is given as control temperature T_∞. The inclusion of the Gibbs-Thomson effect sets the interface temperature as

$$T_{|int} = T_M\left(1 - \frac{\gamma\kappa}{L}\right). \tag{2.47}$$

Here T_M is the melting temperature, L the latent heat, γ the surface tension and the curvature κ is positive when the center of the curvature is in the solid phase:

$$\kappa = -\frac{\frac{d^2\xi}{dx^2}}{\left(1 + \left(\frac{d\xi}{dx}\right)^2\right)^{3/2}}, \tag{2.48}$$

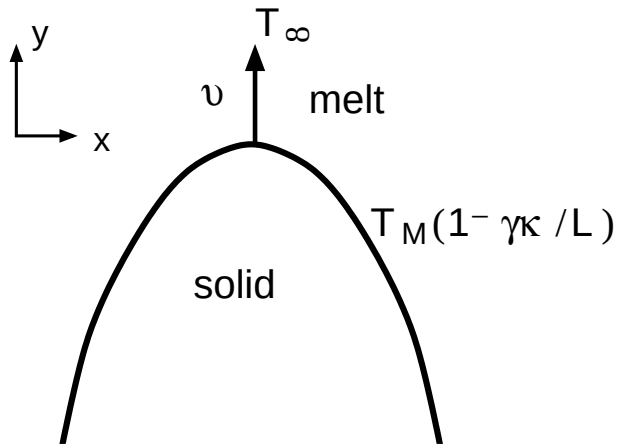

Figure 2.11: Schematic figure for the steady-state growth. At constant velocity υ, the solid phase grows at expense of the melt, which is at temperature $T = T_\infty$ far away from the interface. At the interface, we assume local equilibrium. The interface temperature is reduced due to the Gibbs-Thomson effect, which stabilizes the growth behaviour.

where ξ is the y-component of the interface position. The growth velocity is limited by the heat conservation at the interface as

$$\upsilon_n L = -\left[c_P^{(l)} D^{(l)} \nabla T^{(l)} - c_P^{(s)} D^{(s)} \nabla T^{(s)}\right] \vec{n}. \tag{2.49}$$

By $c_P^{(s),(l)}$ the heat capacity, by $D^{(s),(l)}$ the diffusion constant is denoted, and the normal $\vec{n}$ points into the melt. Applying to Eqs. (2.45) to (2.49), the Green's function method in principle requires the solution of the coupled diffusion equations by giving the integral representation for each phase, and the determination of the interface shape and its position. Such a more general approach can be found in section 4.2, where we need to leave the regime of this kind of symmetric model.

Instead, we introduce the model of symmetric phases. By this we mean that diffusion constants and the heat capacity are equal in both phases. Consequently, the temperature fields in both phases obey the same diffusion equation, and the problem folds down to solving one diffusion equation in the entire domain of both phases, see [53] and [51]. The problem still remains complicated, and we skip the time-dependency and look for steady-state solutions. We consider the diffusion equation in a frame of reference which is centered at the tip of the moving interface,

$$D\nabla^2 T + \upsilon \frac{\partial T}{\partial y} = 0. \tag{2.50}$$

Here D labels the diffusion constant. The dimensionless notation in rescaled variables is obtained

as

$$w = \frac{T - T_\infty}{L/c_P}, \tag{2.51}$$

$$\Delta = \frac{T_M - T_\infty}{L/c_P}, \tag{2.52}$$

$$d\kappa = -\frac{\frac{d^2\xi}{dx^2}}{\left(1 + \left(\frac{d\xi}{dx}\right)^2\right)^{3/2}} \frac{\gamma T_M}{L^2 c_P}, \tag{2.53}$$

d is the capillarity length and ξ denotes the y component of the interface. The dimensionless representation of Eq. (2.50) thus is obtained as

$$\nabla^2 w + \frac{2}{l_D} \frac{\partial w}{\partial y} = 0, \tag{2.54}$$

where we also divided by D, and $l_D = 2D/\upsilon$ is the diffusion length. For the local equilibrium, Eq. (2.47), we get

$$\Delta - d\kappa = w_{|int}, \tag{2.55}$$

where by $|int$ we indicate that the value at the interface is taken. The heat conservation, given as in Eq. (2.56), reads as

$$\upsilon_n = -D \left[\nabla w^{(l)} - \nabla w^{(s)}\right]_{|int} \vec{n}. \tag{2.56}$$

The closed representation of Eqs. (2.54) to (2.56) is derived by elimination of the temperature field in Eq. (2.55). The detailed procedure to eliminate the thermal field is presented now - we give the derivation in the spirit of the original symmetric model [53], which was developed for solid-solid transitions.

2.4.1 Elimination of the Temperature Field

In this subsection, the focus is on the explicit calculation of the closed representation of Eqs. (2.54) to (2.56). Consequently, it is quite technical, and if the reader is only interested in the result - that can be found in Eq. (2.66). We denote the not self-adjoint operator $\mathcal{L}$ which gives Eq. (2.54) as

$$\mathcal{L}_{\vec{x}}[w] = \nabla^2_{\vec{x}}\, w + \frac{2}{l_D} \frac{\partial w}{\partial y}. \tag{2.57}$$

We know that $\mathcal{L}_{\vec{x}}[w] = 0$ in the considered domain, which is bounded by S, see Fig. 2.12 and define the Green's function by

$$\mathcal{L}_{\vec{x}}\,[g(\vec{x} \mid \vec{x}\,')] = -\delta(\vec{x} - \vec{x}\,'), \tag{2.58}$$

$$\mathcal{L}^\dagger_{\vec{x}'}\,[g(\vec{x} \mid \vec{x}\,')] = -\delta(\vec{x} - \vec{x}\,'), \tag{2.59}$$

where by $\mathcal{L}^\dagger$ we denote the adjoint operator of $\mathcal{L}$, by g the Green's function of $\mathcal{L}$ and $\mathcal{L}^\dagger$. For our approach, we will only apply Eq. (2.59), but we want to stress here that the problem exhibits a

non-self-adjoint operator. The explicit definition of the Green's function reads as [57]

$$g(\vec{x} \mid \vec{x}\,') = \frac{1}{2\pi} \exp\left(-\frac{1}{l_D}(y - y')\right) K_0\left(\frac{1}{l_D}\eta(x, x')\right) \tag{2.60}$$

where K_0 is a modified Bessel function, and $\eta = \|\vec{x} - \vec{x}\,'\|$. We obtain for $w(\vec{x}) = \int_{V'} g\mathcal{L}[w] - w\mathcal{L}^{\dagger}[g]$:

$$w(\vec{x}) = \int_{V'} d^3x' \left[g(\nabla^2_{\vec{x'}}\, w) - w(\nabla^2_{\vec{x'}}\, g) + g\frac{2}{l_D}\frac{\partial w}{\partial y'} + w\frac{2}{l_D}\frac{\partial g}{\partial y'}\right] \tag{2.61}$$

to represent the thermal field w.

For the application of Green's theorem, we use the notation familiar in the boundary integral community, see Fig. 2.12, yielding the sign in front of the boundary integral in Eq. (2.62).

$$w(\vec{x}) = -\int_{S'} df' \left[w(\nabla_{\vec{x'}}\, g)\vec{n'} - g(\nabla_{\vec{x'}}\, w)\vec{n'}\right] + \int_{V'} d^3x' \underbrace{\left[g\frac{2}{l_D}\frac{\partial w}{\partial y'} + w\frac{2}{l_D}\frac{\partial g}{\partial y'}\right]}_{2/l_D\vec{\nabla}_{\vec{x'}}\,(0,gw,0)}, \tag{2.62}$$

where $df\ \vec{n} = d\vec{f}$ as shown in Fig. 2.12. The whole expression is reduced to an integral on the surface S, and we express w as

$$w(\vec{x}) = -\int_{S'} df' \left[w(\nabla_{\vec{x'}}\, g)\vec{n'} - g(\nabla_{\vec{x'}}\, w)\vec{n'} + \frac{2}{l_D} g w n'_y\right]. \tag{2.63}$$

To evaluate the integral representation of w as it is stated by Eq. (2.63), we proceed as follows: First, we assume the interface to be of finite length, and recall that the sole heat sources lie at the boundary, and far away from the interface in the liquid phase, $w = 0$. The sketch in Fig. 2.12 illustrates the geometry.

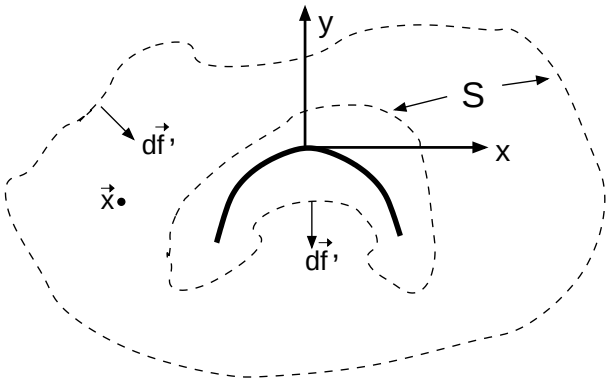

Figure 2.12: First we assume the interface is of finite length. The integration boundary is S, and $d\vec{f} = df\ \vec{n}$ is the surface differential. The point of observation is $\vec{x}$.

Then, we deform the surface S to enclose the interface, see Fig. 2.13. One recognizes here that there are two opposing $d\vec{f}$ for each point of the interface except at the ends.

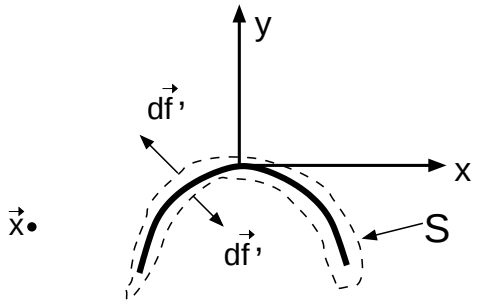

Figure 2.13: The integration contour approaches the interface.

We let the contour of integration enclose the interface to infinitesimal distance and extend the interface to infinity in the *xy*-plane, and consider an effective 2D system such that the surface integral reduces to an integral along the interface contour as

$$\int_S df \rightarrow \left[\int_{-\infty}^{\infty} dx \sqrt{1+\left(\frac{dy}{dx}\right)^2}\, \vec{n}_{(s)} + \int_{\infty}^{-\infty} -dx \sqrt{1+\left(\frac{dy}{dx}\right)^2}\, \vec{n}_{(l)} \right].$$

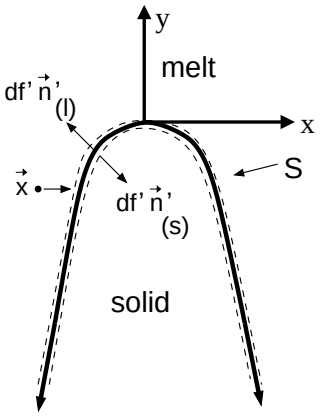

Figure 2.14: The integration contour is infinitesimaly close to the interface, the interface is extended to infinity in the *xy*-plane.

When the integration contour is infinitesimal close to the interface, we can as well set the point of observation infinitesimal close to the interface. The continuity of the temperature cancels all integrands proportional to it, and in 2D we obtain

$$w(\vec{x}) = -\left[\int_{-\infty}^{\infty} dx' \sqrt{1+\left(\frac{dy}{dx'}\right)^2}\, g\left(\nabla_{\vec{x}'} w_{|l} - \nabla_{\vec{x}'} w_{|s}\right) \vec{n}'_{(l)} \right], \tag{2.64}$$

where the jump of the gradient across the interface can be replaced by the free boundary condition,

Eq. (2.56). With [45] $\upsilon_n ds = \upsilon dx$, we obtain

$$w(\vec{x}) = \int_{-\infty}^{\infty} dx'\, g\frac{\upsilon}{D}. \tag{2.65}$$

The effective 2D closed representation of Eq. (2.54) to (2.56) finally takes the form

$$\Delta - \frac{d}{R}\kappa = \frac{p}{\pi}\int_{-\infty}^{\infty} dx' \exp(-p(y-y'))K_0(p\eta(x,x')), \tag{2.66}$$

where all lengths are scaled by the tip radius R. Here 'closed' means that this equation combines the information of the diffusion equation, the conservation of heat, and the local equilibrium, thus containing all information necessary to solve the problem. Equation (2.66) has to be solved to determine the steady-state solution of the problem. One fixes the control parameter Δ and thus the peclet number p, and finds the value of d/pR which corresponds to a shape with smooth tip and parabolic asymptotics.

However, solving this equation is a very challenging task, in spite of the mentioned assumptions and simplifications we made. The introduction of this problem will serve as a good basis for the discussion of the solid-solid transition influenced by the elastic properties of the transition, as given in section 3.2.

2.4.2 What does Selection mean

Within this thesis, we will often discuss the presence of a so-called selection in the problems we consider. Hereby, we mean selection in terms of dendritic growth. Among the different approaches to selection in dendritic growth, there are no examples of analytically simple calculations showing selection mechanisms. However, in the following paragraphs, we briefly describe three examples of selection mechanisms.

Classical Dendritic Growth: Selection by Anisotropy of Surface Tension

As we already mentioned in subsection 2.3.3 about the development of the theory of dendritic growth, the solution of classical dendritic growth requires an anisotropic surface tension. For a digest about this problem in two dimensions, see e.g. [18, 55, 52]. As the analytic efforts to understand the solution are tremendous, we consider the proceeding in detail up to the point where the nature of the derived problem is clear - clear enough to roughly understand the formal mechanism of selection [18]. Within this thesis, we will consider transitions which can be considered to take place in 2D effectively, thus the 3D selection is only shortly mentioned.

2D Selection First we need to define how the anisotropy of the surface tension enters the model. For the closed representation of the solidification process, as we stated it here by Eq. (2.66), the inclusion of anisotropy modifies the capillarity length d which now is orientation dependent as

$$d(\Theta) = d_0(1 - \alpha_d \cos 4(\Theta - \Theta_d)) = d_0 A_d(\Theta). \tag{2.67}$$

Here we introduced the parameter of surface tension anisotropy $\alpha_d \ll 1$, the anisotropy is of fourfold symmetry. The angle Θ is between the normal to the front and the y-axis, which is the direction of growth. Θ_d is the angle between the direction of growth and the direction along which $d(\Theta)$ is minimal. Now, we can describe the approach to find how anisotropic surface tension determines whether a selection is present or not.

From the closed representation of the anisotropic problem, the combination of Eqs. (2.66) and (2.67), a linearization and then neglecting all terms which contain derivatives lead to

$$\frac{(1+x)^{3/2}}{2\pi}\int_{-\infty}^{\infty} dx'\,\frac{(x+x')[\xi(x')-\xi(x)]}{(x-x')[1+\frac{1}{4}(x+x')]} = \sigma_d \tag{2.68}$$

where $\xi(x)$ is the deviation from the Ivantsov solution,

$$y = t - \frac{x^2}{2} + \xi(x), \tag{2.69}$$

and $\sigma_d = d_0/pR$. The integration in Eq. (2.68) with contributing poles at $x' = \pm 2i - x$ leads to a functional equation

$$(x+i)\xi_+(x) + (x-i)\xi_-(-2-2i) - (x+i)\xi_+(-x+2i) + (x-i)\xi_-(x) = i\frac{\sigma_d}{(1+x^2)^{1/2}}, \tag{2.70}$$

where ξ is represented as sum of ξ_+ and ξ_-, which are analytical in the upper and lower half-plane, respectively. When we consider the regions around $x = \pm i$ for Eq. (2.70), we obtain for the limit $x \to i$

$$\xi_-(-x-2i) - \xi_-(x) = i\sigma_d\frac{1}{(1+x^2)^{1/2}(x-i)} \quad | \; x \to i, \tag{2.71}$$

thus $\xi_-(x) \sim (x-i)^{-3/2}$ for $\|x-i\| \ll 1$. Correspondingly, one must not neglect the derivatives in the regime $\|x-i\| \ll 1$, as done in the linearization of the closed representation to derive Eq. (2.68).

Here, we finally obtained the analytic results which are necessary to understand the idea of the method which was successfully applied to the problem. The regime $\|x-i\| \ll 1$ defines an interior layer, and here it is required to take into account the derivative terms in the linearized closed representation. By appropriate rescaling, see [8], one derives a nonlinear differential equation of second order then. The solution of this interior equation than has to be matched to the (exterior) solution obtained by the solution of the Wiener-Hopf equation one obtains from the functional equation (2.70). In the matching of interior and exterior solution, it is revealed how the presence of anisotropy makes the difference between selection and no selection. Often this method of matched complex asymptotics is referred to as KS or PKKS method, named by Kruskal and Segur or also named by Pokrovskii and Khalatnikov, see also [12] or [67].

In the case of isotropic surface tension, the nonlinear differential equation lacks a parameter to be matched with the exterior solution. In the case of anisotropic surface tension, the anisotropy parameter sets an additional parameter which allows this matching, the ratio $\lambda = \alpha^{7/4}/\sigma_d$. The values of λ which allow the matching fix the possible growth velocities.

3D Selection In three dimensions, the anisotropy of the surface tension turns out to complicate the problem even further, so we only sketch the idea which leads to the selection mechansim. As the anisotropy of the surface tension will lead to a nonaxisymmetric crystal, it not sufficient to consider the axisymmetric case as extension of the 2D - problem.

Instead, for the nonaxisymmetric case, a solvability condition needs to be satisfied for each azimuthal harmonic. Kessler and Levine [43] showed numerically that this is possible in principle. The analytic approach by Brener and Ben-Amar [7, 13] yields the correction to the Ivantsov shape close to the tip as

$$z(r,\phi) = -\frac{r^2}{2} + \sum A_m r^m \cos(m\phi). \tag{2.72}$$

Here, lengths are rescaled by the tip radius of curvature R, the crystal grows into z-direction and r, ϕ are the polar coordinates of a crystal surface element. Obviously, the terms which correct the underlying Ivantsov solution will grow faster than the Ivantsov solution itself when one leaves the region close to the tip. The question rises how a solution which takes this form close to the tip can be matched with the asymptotic behaviour one expects from the Ivantsov paraboloid of revolution.

The key idea to solve this problem [13] is the interpretation of the 3D problem as initial value 2D problem for the cross section of the crystal in the tail region. The nonaxisymmetric corrections at the tip serve as initial conditions, and the corrections to the Ivantsov shape remain small only close to the tip. Sufficiently far behind the tip, four arms develop in the assumed case of a fourfold symmetry of the surface tension, which states a strong deviation ot the Ivantsov paraboloid of revolution. The length of the arms scales as $||z||^{3/5}$, the width like $||z||^{2/5}$, before the length of these arms finally grows as $||z||$ in the asymptotic regime.

Selection by Triple Junction

The presence of a triple junction changes the selection problem entirely. We recall that the necessity of an anisotropic capillarity length was indicated when all approaches with isotropic surface tension failed to produce an interface with smooth tip, see e.g. the numerical results in [57]. A physical solution requires vanishing slope at the tip in classical dendritic growth, so the interesting question arises - how will the presence of a physically motivated cuspid tip, due to a triple junction, change the selection problem?

We find the answer in [16], where melting along a grain boundary is considered, see Fig. 2.15.

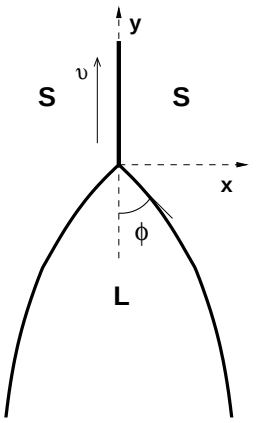

Figure 2.15: The melt zone propagates along the grain boundary at constant velocity υ. The solid phases are marked by S, the melt phase by L. The triple junction is in the origin of the coordinate system, by ϕ we label the opening angle at the tip.

In contrast to the dendritic solvability condition that $\phi = \pi/2$, here we must find a solution with $\phi < \pi/2$, obviously. The anisotropy of the surface tension as we just defined it in Eq. (2.67) is neglected here, since it has only little influence compared to the triple junction.

The closed representation of the system then reads as Eq. (2.66) when we redefine the temperature as $w = c_p(T_\infty - T)/L$ and the overheating as $\Delta = c_p(T_\infty - T_M)/L$. Here the temperature in the solid far away from the interface is denoted by $T_\infty > T_M$. In the limit of small opening angles $\phi \ll 1$ and ratios $p/\phi^2 \gg 1$, one obtains that the interface is governed by a linear integro-differential equation,

$$1 + \mu_d \frac{d^2x}{dy^2} = \frac{\sqrt{2}}{\pi} \int_0^y dy' \frac{dx(y')}{dy'} \frac{1}{\sqrt{||y - y'||}}. \tag{2.73}$$

Eq. (2.73) is solved by means of a Laplace transformation, which selects the eigenvalue $\mu_d = d_0\phi^3/R\Delta$ - the transformation from the image space back to the real space will only give a physical solution if $\mu_d = \pi/2$.

The selection theory in presence of a triple junction is much more transparent than the selection by anisotropy of the surface tension. The triple junction leads to a velocity selection with isotropic surface tension, and we will consider the influence of a triple junction in other selection problems within the next chapters.

3 Phase Transitions Limited by Thermal Diffusion in Presence of Lattice Strains

Pattern formation in diffusion-limited phase transitions is of utmost significance in metallurgical fabrication. Nearly every house we enter, any car we use, contains elements which passed through such phase transitions during their production process.

Whilst for the solidification of a pure substance, elastic effects typically are not in the focus of investigation, the question arises which role elastic tensions in solid-solid transitions play. It is evident that lattice changes in solid-solid systems especially will affect the interface. Massive displacements can occur to relax the system with respect to the onsetting tensions, constituting singular interface deformations. Consequently, the inclusion of lattice strains is an obvious idea. However, within the method we use, it is a not less challenging idea. The importance of predictions for this combined elastic-diffusional transitions by means of the Green's function method have to be significantly revalued. There are increasingly many simulations for these systems, but by principle they cannot rigorously resolve the asymptotically dominating behaviour. In the light of this strong demand for rigorous steady-state results, the value of the results we will present in this chapter on the most basic geometries and elastic configurations can be valued better.

This chapter is roughly separated into considerations for single crystal and bicrystal growth. The presence of a triple junction in bicrystal growth suggests this discrimination. Since selection can occur due to a triple junction [16], we need to distinguish systems with and systems without triple junction.

Section 3.1 serves as rough introduction for the common physical aspects of single and bicrystal growth. It mentions the basic assumptions which we make for the system. Thus it lays the foundations for the calculations in the following sections, in conjunction with section 2.4, where the Green's function method we apply is introduced.

Section 3.2 contains the model development, code testing and analytical and numerical results for single crystal growth.

Section 3.3 focuses on the extension of the single-crystal model to the bicrystal model and the analytical and numerical results for bicrystal growth.

3.1 Basic Physical Model

In this section, we want to give a brief description of the basic physical aspects of the transitions which we investigate. Only effects which are common in single and bicrystal growth are discussed, the model is developed in detail in the sections corresponding to each growth geometry.

The first system of interest exhibits a solid-solid transition. Releasing latent heat at the moving interface, the onsetting phase (β) grows at expense of reference phase (α), see Fig. 3.1. We assume that the reference phase (α) is only slightly undercooled, such that the limiting factor of the transition velocity is the transport of the latent heat away from the interface. The transport

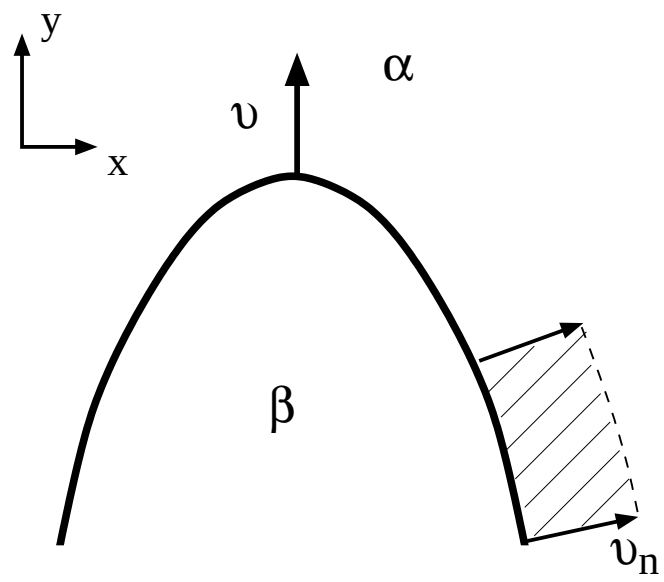

Figure 3.1: Sketch of the steady-state transition. Solid phase (β) grows at expense of solid reference phase (α) at constant velocity υ. Heat conservation fixes the normal velocity υ_n: The shaded area grows $\sim \upsilon_n$ and thus the release of latent heat L that fixes the difference of the fluxes $\upsilon_n L = -c_p D\vec{n}\left(\nabla T_\alpha - \nabla T_\beta\right)$ is also proportional to υ_n.

takes place by diffusion, rendering the problem a diffusional phase transition.

The structural difference between both phases leads to lattice strains, which affect the transition. Especially at the interface, where we assume coherency of the phases, it is apparent that the different lattices lead to elastic stresses. Due to the coherency of the interfaces, where the elastic stresses do not relax by means of singular distortions, an elastic hysteresis occurs. This elastic hysteresis shifts the transition temperature so that the temperature at the interface differs from the equilibrium transition temperature. Another shift in the interface temperature stems from the Gibbs-Thomson effect, it stabilizes the interface by a reduction of the interface temperature. The conjunction of the corrections to the interface temperature due to the elastic hysteresis and the Gibbs-Thomson effect is the basis of the local equilibrium which we assume on the interface. Altogether, this describes the basic physical processes which we consider.

Our specific interest focuses on the transition velocity which appears when transients have grown out, i.e. a steady-state solution, and the characteristic length scale of the onsetting interface. From experiments in various alloys, e.g. steel types, it is known that dendrites are found on many occasions. Our belief that the dominating steady-state solution also dominates the essential structural aspects of real materials is supported by such findings. The characteristic length scale in such dendritic patterns is the tip radius of curvature of an Ivantsov parabola which asymptotically matches the interfaces which we find.

3.1.1 Basic Approximative Assumptions

As the problem is an elastic-diffusional determined transition, one has to make a point about the nature of the elastic-diffusional coupling. We will assume the elastodynamics to relax sufficiently

faster than the diffusion. This means that the governing equations, originally coupled for diffusion and elastic fields, decouple except for a boundary condition, namely local equilibrium, and we obtain elastostatic behaviour. In addition to the simplification of the coupling of the diffusional and elastic problem, the consideration of both aspects is subject to further symmetry assumptions - the thermal diffusion is simplified in the spirit of the 'symmetric model' [53, 51, 57], see also subsection 2.4, i.e. we assume identical thermal diffusion properties in all phases. The elastic problem is also symmetrized, and this ansatz yields the closed representation of the entire problem, as we show in detail in sections dedicated to the single and bicrystal growth geometries.

3.1.2 Diffusional Aspect

The material which undergoes the transition is assumed to be pure and to exhibit identical heat diffusion properties in the solid phases. Instead of solving two different diffusion equations in two physically distinct domains, we thus consider one diffusion equation for the temperature field T in the entire system. We are specifically interested in the asymptotically dominating behaviour of the system, thus we focus on steady state solutions and consider the problem in a co-moving frame of reference located at the tip of the interface.

$$D\nabla^2 T + \upsilon \frac{\partial T}{\partial y} = 0, \tag{3.1}$$

where by υ we denote the constant growth velocity of the interface, and D is the thermal diffusion constant. The heat sources on the unknown interface are defined by

$$\upsilon_n L = -c_p D \vec{n} \left(\nabla T_\alpha - \nabla T_\beta \right), \tag{3.2}$$

where the heat capacity is denoted by c_P, and the latent heat per unit volume by L. The normal velocity υ_n of the interface is fixed by heat conservation, see Fig. 3.1. Here $\upsilon_n L$ is the heat per unit area and unit time which is set free by the phase transition at the interface, thus stating the jump of the heat flux across the interface. In phase (α), which is stable above the equilibrium transition temperature, the temperature T far away from the interface is set to $T = T_\infty$.

The local equilibrium on the interface reads as

$$T_{|int} = T_{eq} \left(1 - \frac{\gamma \kappa}{L} + \frac{\delta \tilde{F}^{el}}{L} \right), \tag{3.3}$$

where $T_{|int}$ denotes the temperature on the interface and T_{eq} is the equilibrium transition temperature of a flat interface. By γ we label the isotropic surface tension, by κ the curvature and by L the latent heat per unit volume. Eq. (3.3) defines the shift of the interface temperature due to the Gibbs-Thomson effect and the elastic effects. We neglect kinetic corrections as we are mainly interested in the regime of small undercoolings, which is also most important for experimantal setups. The Gibbs-Thomson effect is explained in section 2.3.1, and $\delta \tilde{F}^{el}$ represents the elastic effects, which are introduced in the following subsection.

3.1.3 Elastic Aspect

We assume an elastically isotropic system which effectively is two-dimensional in terms of the spatial dependencies of the elastic quantities. An example of such systems is provided in [31], where ferroelastic transitions were investigated. A convenient implication of this assumption is the reduction of the number of elastic coefficients to two. A sketch of the underlying transformation is given in Fig. 3.2.

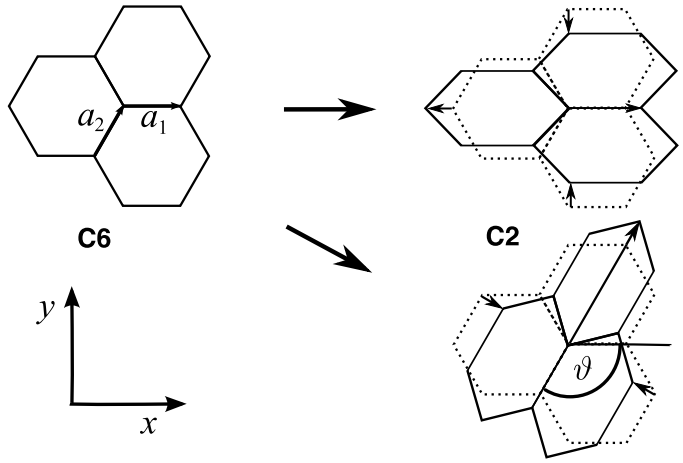

Figure 3.2: Schematic picture of the structure transition. The hexagonal lattice transforms to a hexagonal-orthorhombic lattice, which lowers the symmetry as $C_6 \mapsto C_2$. This fixes the possible angles as $\vartheta = 0, \pm 2\pi/3$. The resulting nonvanishing eigenstrains are given as $\epsilon^s_{xx} = -\epsilon \cos 2\vartheta$, $\epsilon^s_{yy} = \epsilon \cos 2\vartheta$, $\epsilon^s_{xy} = -\epsilon \sin 2\vartheta$, where ϵ is the common magnitude of the lattice strains.

This transformation will serve as an example for the lattice strains we use for shear. The other type of lattice strain we consider is a dilatational lattice strain, $\epsilon^d_{ik} = \delta_{ik}\epsilon$, and finally we will cover the regime of superpositions of these basic modes. To be more precise, we will introduce the lattice strain tensors $\epsilon^{\pm}_{ik} = \eta\epsilon^d_{ik} \pm (1-\eta)\epsilon^s_{ik}$. We refer to the case ϵ^+_{ik} as positive mixing, and to ϵ^-_{ik} as negative mixing. The mixing parameter η is defined such that the limit $\eta = 0$ yields pure shear, while $\eta = 1$ corresponds to pure dilatation. For the thermodynamic viewpoint, we introduce the free energydensities $F_{\alpha,\beta}$ of the system. The assumption of equal elastic constants E, ν in both phases allows us to write

$$F_\alpha = F^0_\alpha(T) + \frac{E}{2(1+\nu)}\left(\frac{\nu}{1-2\nu}\left(u^{(\alpha)}_{ii}\right)^2 + \left(u^{(\alpha)}_{ik}\right)^2\right), \tag{3.4}$$

in the initial phase, and for the new phase

$$F_\beta = F^0_\beta(T) + \frac{E}{2(1+\nu)}\left(\frac{\nu}{1-2\nu}\left(u^{(\beta)}_{ii} - \epsilon_{ii}\right)^2 + \left(u^{(\beta)}_{ik} - \epsilon_{ik}\right)^2\right). \tag{3.5}$$

We denote the strain tensor in the i-th phase by

$$u_{ik}^{(\alpha,\beta)} = \frac{1}{2}\left(\frac{\partial u_i^{(\alpha,\beta)}}{\partial x_k} + \frac{\partial u_k^{(\alpha,\beta)}}{\partial x_i}\right), \tag{3.6}$$

by ϵ_{ik} the eigenstrain in the onsetting phase. The elastic coefficients are E, the elastic modulus, and ν, the Poisson ratio. We denote the free energydensity without elastic effects by $F_i^0(T), i = \alpha,\beta$. As Eqs. (3.4) and (3.5) indicate, we assume symmetric elastic phases, i.e. identical elastic constants E, ν.

We restrict our considerations to the cases of small distortions, which suggests that we assume coherency of the interfaces, $u_i^{(\alpha)} = u_i^{(\beta)}$. Consequently, our model includes elastic hysteresis, which cannot occur in absence of coherency [20]. The appropriate modified Free energy, obtained by a Legendre transformation from the free energy[70], reads as

$$\tilde{F}_i = F_i^0 - \sigma_{nn}^{(i)} u_{nn}^{(i)} - 2\sigma_{n\tau}^{(i)} u_{n\tau}^{(i)}, \tag{3.7}$$

where n,τ are the normal and tangential coordinates in the local coordinate system, and $i = \alpha,\beta$ are the phases. This potential is also discussed in [75], and an illustrative example for a planar interface is given in [76].

The shift of the interface temperature $T_{eq}\delta\tilde{F}^{el}/L$ in Eq. (3.3) is due to the elastic hysteresis, which we define in terms of the modified free energies $\tilde{F}_i$ in a very convenient way as

$$\delta\tilde{F}^{el} = \tilde{F}_\alpha^{el} - \tilde{F}_\beta^{el}, \tag{3.8}$$

where the superscript *el* indicates that only the elastic contribution to the modified free energy is taken into account.

3.2 Single Crystal Diffusional Solid-Solid Transition in Presence of Lattice Strains

The field of diffusional phase transitions offers various challenging systems to consider. We explained the successful so-called symmetric model in section 2.4 to illustrate the fundamental issues concerning steady-state growth in dendritic solidification. Now we will model a solid-solid transition which involves heat diffusion and take lattice strains into account.

The considered lattice strains also represent fundamental modes of strain as they occur for example in a ferroelastic system described in [31] - they will provide us both the necessary variety of lattice transitions to study the elastic-diffusional interaction and an example of a real system.

We will establish a model which applies the Green's function technique to derive a closed representation of the governing equations. While this approach is well-known to obtain an evolution equation for the interface for diffusional phase transitions, see [53, 51, 66, 77, 78] and subsection 2.4, the inclusion of elastic effects in a closed representation which states then the coupled elastic-diffusional problem is new.

For the interpretation of the results we obtain, we shall remember some basic outcome of solvability theory in classical dendritic growth, see [18]. For the isotropic surface tension we assume here, the occurence of a selection for a smooth tip means that elastic effects lead to a new selection mechanism. This is the focus here, furthermore we discuss the influence of the relative orientation of the growth direction to the lattice strain on the transition.

Subsections 3.2.1 to 3.2.3 discuss the thermal and elastic aspects of the system and how they are linked to obtain the closed representation of the coupled thermo-elastic problem.

Subsections 3.2.4 to 3.2.6 treat the fundamental lattice strains separately, namely pure dilatation, pure shear and superpositions of both.

Subsection 3.2.7 introduces a lattice strain configuration with vanishing elastic hysteresis - it is theoretically possible, and would be energetically preferred.

3.2.1 Diffusional Aspect

We consider a transformation between two solid phases, using (α) to denote the high temperature (reference) and (β) to denote the low temperature (onsetting) phase. Here high and low temperature refer to the thermodynamic stability of the phases above (high) or below (low) the equilibrium transition temperature. The transformation is assumed to be limited by heat conduction of the latent heat set free at the moving interface, see Fig. 3.1. By Eqs. (3.1) to (3.3) we define the governing equations of the diffusional problem. Now we derive the closed representation in accordance to the symmetric model we discussed in section 2.4. First, to simplify the representation of the problem, we introduce dimensionless variables,

$$w = c_p \frac{T - T_\infty}{L}, \tag{3.9}$$

which is the temperature field,

$$\Delta = c_p \frac{T_{eq} - T_\infty}{L}, \tag{3.10}$$

the control temperature of the process, and

$$d = c_p \frac{T_{eq}\gamma}{L^2}, \tag{3.11}$$

the capillarity length. The resulting representation of the diffusion equation (3.1) reads as

$$\nabla^2 w + \frac{2}{l_D}\frac{\partial w}{\partial y} = 0, \tag{3.12}$$

where we also divided by D and define the diffusion length $l_D = 2D/\upsilon$. Heat conservation, Eq. (3.2), is given by

$$\upsilon_n = -D\vec{n}\left(\nabla w^{(\alpha)} - \nabla w^{(\beta)}\right). \tag{3.13}$$

The dimensionless notation of local equilibrium, Eq. (3.3), reads as

$$w_{|int} = \Delta - d\kappa + \frac{T_{eq}c_p}{L^2}\delta\tilde{F}^{el}, \tag{3.14}$$

where the subscript $|int$ indicates that w is considered at the interface. Briefly spoken, the Green's function method lets us eliminate the field w in Eq. (3.14) by means of its formal integral solution. Like in the example discussed in section 2.4, the phases α and β are considered as one domain of definition for the temperature w. Consequently, the index α or β now indicates only which phase is observed, but does not label two separate fields. In Eq. (3.14), the elimination of the thermal field by its integral representation reads as

$$w(\vec{x}) = \int_{-\infty}^{\infty} dx'\, g\frac{\upsilon}{D}, \tag{3.15}$$

where the free space Green's function for (3.12) is given by

$$g = \frac{1}{2\pi}\exp\left(-\frac{1}{l_D}(y-y')\right)K_0\left(\frac{\eta(x,x')}{l_D}\right). \tag{3.16}$$

The next step contains the scaling of the coordinates by R. Here R is the radius of an Ivantsov parabola which we match to our solutions asymptotically. The reason for this asymptotic matching is discussed in section 3.2.3. Due to the scaling by R, the Peclet number p appears,

$$p = \frac{\upsilon R}{2D}, \tag{3.17}$$

it contains both determining quantities of the transition, besides the steady-state velocity υ also the tip radius of curvature R of the asymptotically matching Ivantsov parabola which is defined by $y_{Iv} = -x^2/2R$. The Peclet number is implicitly determined by the dimensionless control temperature $\tilde{\Delta}$ as

$$\tilde{\Delta} = (p\pi)^{1/2}\exp(p)erfc(p^{1/2}). \tag{3.18}$$

Here *erfc* is the inverse error function, defined as in [1]. We denote the driving force by $\tilde{\Delta}$

instead of the usual Δ to emphasize the shift of the equlibrium transition temperature by the elastic hysteresis. The precise definition of $\tilde{\Delta}$ will be given in the subsequent section. For the closed dimensionless representation of the problem we thus obtain

$$\Delta - \frac{d\kappa}{R} + \frac{T_{eq} c_p \delta\tilde{F}^{el}}{L^2} = \frac{p}{\pi} \int_{-\infty}^{\infty} dx' \exp[-p(y(x) - y(x'))] K_0(p\eta(x, x')). \tag{3.19}$$

The detailed derivation of the elastic influence in the next section explains not only the yet undefined term $\delta\tilde{F}^{el}$, but also the relation of Δ and $\tilde{\Delta}$ in Eq. (3.19).

3.2.2 Elastic Part

In this section, we discuss the derivation of the integral representation of the elastic fields. For Eq. (3.19), this provides us the necessary expressions for $\delta\tilde{F}$ in terms of the interface $y(x)$. The explicit definition of $\delta\tilde{F}^{el}$ comprises Eqs. (3.4) to (3.8), we only give a compact version here for a better overview.

$$\delta\tilde{F}^{el} = \frac{E}{2(1+\nu)} \left[\left(\frac{\nu}{1-2\nu} \left(u_{ii}^{(\alpha)} \right)^2 + \left(u_{ik}^{(\alpha)} \right)^2 \right) - \left(\frac{\nu}{1-2\nu} \left(u_{ii}^{(\beta)} - \epsilon_{ii} \right)^2 + \left(u_{ik}^{(\beta)} - \epsilon_{ik} \right)^2 \right) \right]. \tag{3.20}$$

We discriminate nonlocal and local contributions to $\delta\tilde{F}$, the next paragraph describes the nonlocal part of $\delta\tilde{F}$, then we turn to the local part.

Nonlocal Contributions of $\delta\tilde{F}^{el}$ at the Interface

In this paragraph, we achieve a representation of $\delta\tilde{F}^{el}$ which no longer depends on $\sigma_{ik}^{(\beta)}$ and $u_{ik}^{(\beta)}$. This lets us eliminate the remaining strain $u_{ik}^{(\alpha)}$ by means of the formal solution in terms of the Green's tensor. In conjunction, this provides us the representation of $\delta\tilde{F}^{el}$ in terms of the interface $(x, y(x))$. To eliminate the strains and stresses of phase β from the problem, we consider the mechanical equilibrium on the interface,

$$\sigma_{ni}^{(\alpha)} = \sigma_{ni}^{(\beta)}. \tag{3.21}$$

Here $i = n, \tau$ denotes the components in local coordinates, and we determine the discontinuities of strain and stress tensor across the interface as

$$u_{nn}^{(\beta)} - u_{nn}^{(\alpha)} = \epsilon_{nn} + \frac{\nu}{1-\nu}(\epsilon_{\tau\tau} + \epsilon_{zz}), \tag{3.22}$$

$$u_{n\tau}^{(\beta)} - u_{n\tau}^{(\alpha)} = \epsilon_{n\tau}, \tag{3.23}$$

$$\sigma_{\tau\tau}^{(\beta)} = \sigma_{\tau\tau}^{(\alpha)} - \frac{E}{1-\nu^2}(\epsilon_{\tau\tau} + \nu\epsilon_{zz}). \tag{3.24}$$

Eqs. (3.22) to (3.24) allow to express $\delta\tilde{F}^{el} = \tilde{F}_{\alpha}^{el} - \tilde{F}_{\beta}^{el}$ in terms of strains in the α-phase, $u_{ik}^{(\alpha)}$, and the lattice strains ϵ_{ik}. In addition, due to the linearity of the problem, one can redefine the problem here by separation of the lattice strain-dependant contribution to the stresses. The new stresses are

defined as

$$\frac{\partial \tilde{\sigma}_{ik}^{(\alpha,\beta)}}{\partial x_k} = \frac{\partial \sigma_{ik}^{(\alpha,\beta)}}{\partial x_k} + \frac{\partial \sigma_{ik}^{(\alpha,\beta)\epsilon}}{\partial x_k}, \tag{3.25}$$

thus we obtain for the elastostatic equations, which we originally denote by

$$\frac{\partial \sigma_{ik}^{(\alpha,\beta)}}{\partial x_k} = 0, \tag{3.26}$$

now, in terms of the new stresses,

$$\frac{\partial \tilde{\sigma}_{ik}^{(\alpha,\beta)}}{\partial x_k} = 0. \tag{3.27}$$

Obviously, Eq. (3.27) corresponds to vanishing discontuities at the interface instead of Eqs. (3.22) to (3.24). The mechanical equilibrium thus must be satisfied in a different way. We discuss exemplarily the y-component of the force density at the interface. It holds

$$\int dA[F_y^{(\alpha)} + F_y^{(\beta)}] = 0, \tag{3.28}$$

where $\int dA F_y^{(i)} = \int dA(\partial \sigma_{yk}^{(i)}/\partial x_k)$, and dA is the differential of the area of integration enclosed by Δs and Δl, as shown in Fig. 3.3.

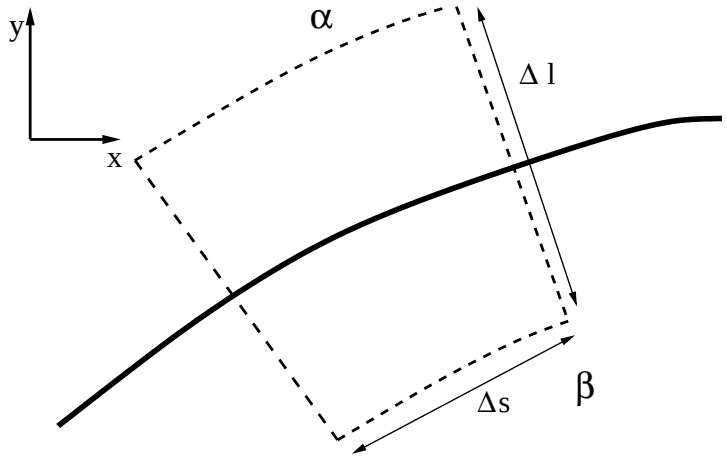

Figure 3.3: Schematic picture of the integration area to yield the artificial forces.

We introduce the artificial stresses σ_{yk}^{ϵ}, which are defined according to Eq. (3.28) as

$$\int dA \left(\frac{\partial \tilde{\sigma}_{yk}^{(\beta)}}{\partial x_k} - \frac{\partial \sigma_{yk}^{(\alpha)}}{\partial x_k} \right) = \int ds \sigma_{yk}^{\epsilon} n_k. \tag{3.29}$$

The artificial stresses σ_{ik}^{ϵ} formally substitute the jump conditions of the strains and stresses at the

interface, and we yield their representations in terms of the elastic strains later. If we let the area of integration shrink to a interface-parallel strip of infinitesimal width and length Δs, we obtain

$$\Delta s \left[(\tilde{\sigma}^{(\beta)}_{yk} - \sigma^{(\alpha)}_{yk}) n_k \right] = \Delta s \, \sigma^{\epsilon}_{yk} n_k. \tag{3.30}$$

In general, for component i we obtain

$$(\tilde{\sigma}^{(\beta)}_{ik} - \sigma^{(\alpha)}_{ik}) n_k = \sigma^{\epsilon}_{ik} n_k. \tag{3.31}$$

By Eq. (3.31), we obtained the definition of the artificial force density, $F^{\epsilon}_i = \sigma^{\epsilon}_{ik} n_k$. We could also have obtained F^{ϵ}_i since the stresses σ^{ϵ}_{ik} are determined by $\sigma^{\epsilon}_{ij} = c_{ijkl} \epsilon_{kl}$, thus

$$\sigma^{\epsilon}_{ik} = \frac{E}{1+\nu} \left(\epsilon_{ik} + \frac{\nu}{1-2\nu} \delta_{ik} \epsilon_{ik} \right). \tag{3.32}$$

Here the tensor c_{ijkl} is the elasticity tensor.

The expressions for the artificial forces complete the reformulation of the problem, which is now independent of $\sigma^{(\beta)_{ik}}$ and $u^{(\beta)_{ik}}$. Now, we can calculate the representation for $\delta\tilde{F}^{el} = \tilde{F}^{el}_{\alpha} - \tilde{F}^{el}_{\beta}$ as

$$\delta\tilde{F} = \sigma^{\epsilon}_{nn} u^{(\alpha)}_{nn} + \sigma^{\epsilon}_{\tau\tau} u_{\tau\tau} + 2\sigma^{\epsilon}_{n\tau} u^{(\alpha)}_{n\tau} - 0.5 \frac{E}{1-\nu^2} (\epsilon^2_{\tau\tau} + \epsilon^2_{zz} + 2\nu\epsilon_{zz}\epsilon_{\tau\tau}). \tag{3.33}$$

Since the calculation for equation (3.33) is lengthy, it is given in detail in the appendix A.3. As we need to express $\delta\tilde{F}^{el}$ on the interface in Eq. (3.19), the index (α) for the strain $u^{(\alpha)}_{ik}$ means here that we take the strain in phase (α), at $\delta\vec{n}$ from the interface and let $\delta\vec{n} \to 0$. Token altogether, reformulating the problem for σ^{ϵ}_{ik} and $u^{(\alpha)}_{ik}$ effectively reduces the elastic problem to the solution of the elastic equations in one phase, and the displacement $u^{(\alpha)}_{ik}$ can be represented by the standard Green's tensor [74] as

$$u^{(\alpha)}_i = \int ds' g_{ik}(r - r') F^{\epsilon}_k(r'), \tag{3.34}$$

where the Green's tensor for the elastic isotropic medium in plane strain is [49]

$$g_{ik}(r, r') = \frac{1+\nu}{4\pi(1-\nu)E} (n_i n_k - (3-4\nu)\delta_{ik} ln(\|\vec{r} - \vec{r}'\|)). \tag{3.35}$$

By $n_i n_k$, we denote $(x_i - x'_i)(x_k - x'_k)/\|\vec{r} - \vec{r}'\|^2$, and $F^{\epsilon}_k(r)$ is the force surface density, defined as $F^{\epsilon}_k(r) = \sigma^{\epsilon}_{ik} n_k$. The contraction of the strain tensor and the stress tensor in Eq. (3.33) is invariant under coordinate transformations, and we denote the contraction in cartesian coordinates to obtain

$$\delta\tilde{F}^{el} = \sigma^{\epsilon}_{ik} u^{(\alpha)}_{ik} - 0.5 \frac{E}{1-\nu^2} (\epsilon^2_{\tau\tau} + \epsilon^2_{zz} + 2\nu\epsilon_{zz}\epsilon_{\tau\tau}), \tag{3.36}$$

where $i, k = x, y$. Here, the strains $u^{(\alpha)}_{ik}$ in Eq. (3.33) are eliminated by

$$u^{(\alpha)}_{im} = \frac{1}{2} \int ds' \left(\frac{\partial g_{mk}}{\partial x_i} + \frac{\partial g_{ik}}{\partial x_m} \right) F^{\epsilon}_k, \tag{3.37}$$

which in a less compact formulation reads as

$$u_{im} = \frac{1+\nu}{4\pi(1-\nu)E}\int ds' \frac{F_k}{r^4}(x_k(r^2\delta_{mi} - x_i x_m) - x_i x_k x_m - r^2(1-2\nu)(\delta_{ik}x_m + \delta_{mk}x_i)).$$

The integral $\int ds'$ is prescribed along the moving interface. It is $x_i = (x-x'),(y-y')$, $r = ((x-x') + (y-y'))^{1/2}$ is the distance between point of observation and point of integration. We reached a good point for a brief summary of our proceeding up to here.

Summary: Elimination of the Nonlocal Elastic Fields In the beginning of this subsection we stressed that we need to express $\delta\tilde{F}$ in terms of the interface $y(x)$ which we will find. We introduced the modified free energies $\tilde{F}_{\alpha,\beta}$, which depend on the canonical variables that appear due to the mechanical equilibrium.

The jump conditions Eqs. (3.22) to (3.24) which result from the mechanical equilibrium let us eliminate the β-phase strains and stresses, and we can define artificial stresses which effectively substitute the lattice strains. These artificial stresses are defined in Eq. (3.32), and the resulting expression for $\delta\tilde{F}^{el}$ only contains the artificial stresses σ^{ϵ}_{ik} and the strains $u^{(\alpha)}$ - which we eliminate by the elastic Green's tensor, Eq. (3.38). Concluding, this part yields the central part of the expression of $\delta\tilde{F}^{el}$ in terms of $(x, y(x))$, which is required for the closed representation of the entire problem.

Local Contributions for $\delta\tilde{F}^{el}$

The remaining contribution to $\delta\tilde{F}^{el}$ can be separated into a constant and a remaining local depending part as

$$\delta\tilde{F}^{el}_{local} = -\frac{1}{2}\frac{E\epsilon^2}{(1-\nu^2)}(\bar{\epsilon}^2_{yy} + \bar{\epsilon}^2_{zz} + 2\nu\bar{\epsilon}_{yy}\bar{\epsilon}_{zz}) - \frac{1}{2}\frac{E\epsilon^2}{(1-\nu^2)}B(\vec{x}). \tag{3.38}$$

Here we define auxiliary functions

$$B = A^2 + 2A\bar{\epsilon}_{yy} + 2\nu A\bar{\epsilon}_{zz} \tag{3.39}$$

$$A = n_y^2(\bar{\epsilon}_{xx} - \bar{\epsilon}_{yy}) - 2n_x n_y\bar{\epsilon}_{xy}, \tag{3.40}$$

where by n_x, n_y we denote the components of the surface normal at the point of observation. In Eq. (3.38) we introduced $\bar{\epsilon}_{ik} = \epsilon_{ik}/\epsilon$, where $\epsilon \ll 1$ is the order of magnitude of the lattice strains. The definition of function $B(\vec{x})$ shows that $B \to 0$ when $y \to -\infty$, and since the nonlocal contribution $\sim \sigma^{\epsilon}_{ik}u^{(\alpha)}_{ik}$ also vanishes in that limit, $\delta\tilde{F}^{el}$ asymptotically yields

$$\delta\tilde{F}^{el}_{local} = -\frac{1}{2}\frac{E}{(1-\nu^2)}(\epsilon^2_{\tau\tau} + \epsilon^2_{zz} + 2\nu\epsilon_{zz}\epsilon_{\tau\tau}) \to -\frac{1}{2}\frac{E}{(1-\nu^2)}(\epsilon^2_{yy} + \epsilon^2_{zz} + 2\nu\epsilon_{yy}\epsilon_{zz}) \tag{3.41}$$

when $y \to -\infty$. This provides the appropriate measure for the strength of the elastic effects, in a dimensionless notation

$$\Delta_{el} = \frac{1}{2}\frac{T_{eq}c_p\epsilon^2 E}{(1-\nu^2)L^2}(\bar{\epsilon}^2_{yy} + \bar{\epsilon}^2_{zz} + 2\nu\bar{\epsilon}_{yy}\bar{\epsilon}_{zz}). \tag{3.42}$$

Eq. (3.42) thus completes the definition of the shifted undercooling $\tilde{\Delta} = \Delta - \Delta_{el}$. By Δ_{el} we denote the asymptotic shift of the transition temperature due to the lattice strains, the elastic hysteresis.

$$\frac{T_{eq}c_p\delta\tilde{F}^{el}}{L^2} = \frac{T_{eq}c_p}{L^2}\sigma^{\epsilon}_{ik}u^{(\alpha)}_{ik} - \frac{1}{2}\frac{T_{eq}c_pE\epsilon^2}{L^2(1-\nu^2)}B(\vec{x}) - \Delta_{el}. \tag{3.43}$$

Now we can subsume the results from this and the previous section to obtain the complete formulation in all necessary detail, which leads to the next section.

3.2.3 Solution of the Coupled Elasto-Diffusional Problem

In the previous subsections, we have derived the necessary representations of the distinct contributions to consider the problem in its entire complexity, namely Eqs. (3.19) and (3.43). Temperature field and strain fields have been eliminated by application of Green's function technique. The obtained equation,

$$\begin{aligned}\tilde{\Delta} &- \frac{d\kappa}{R} + \frac{T_{eq}c_p}{L^2}\left[\sigma^{\epsilon}_{ik}u^{(\alpha)}_{ik} - \frac{E\epsilon^2B(\vec{x})}{2(1-\nu^2)}\right] \\ &= \frac{p}{\pi}\int_{-\infty}^{\infty}dx'\,\exp[-p(y(x)-y(x'))]K_0(p\eta(x,x')).\end{aligned} \tag{3.44}$$

can be further simplified, as we discuss now. In many real situations, the Peclet number takes values in the range of 0.01 to 0.1, thus it is appropriate to consider the limiting case $p \ll 1$. Then, the Peclet number behaves approximately as

$$p = \frac{\tilde{\Delta}^2}{\pi}, \tag{3.45}$$

and we can approximate the kernel on the r.h.s. of Eq. (3.44) as [1]

$$\frac{1}{2\pi}\exp[-p(y(x)-y(x'))]K_0(p\eta(x,x')) \longrightarrow -\frac{1}{2\pi}\log\left\|\frac{p\eta(x,x')}{2}\right\|, \tag{3.46}$$

where $\eta(x,x')$ is the distance between point of observation and point of integration. Furthermore, we substitute $\tilde{\Delta}$ by its integral representation,

$$\tilde{\Delta} = \frac{p}{\pi}\int_{-\infty}^{\infty}dx'\left[-\log\left\|\frac{p\eta_{Iv}(x,x')}{2}\right\|\right], \tag{3.47}$$

where the Ivantsov solution sets $\eta_{Iv}(x,x')$ as

$$\eta_{Iv}(x,x') = \left((x-x')^2 + \left(-\frac{x^2}{2} + \frac{x'^2}{2}\right)^2\right)^{1/2}. \tag{3.48}$$

The aforementioned approximations let us represent Eq. (3.44) depending only on Δ_{el}/p. This dependence is plain to see when we divide by p and define $\Phi = 2(1-\nu^2)/(E\epsilon^2(\bar{\epsilon}^2_{yy} + \bar{\epsilon}^2_{zz} + 2\nu\bar{\epsilon}_{yy}\bar{\epsilon}_{zz}))$.

We then obtain

$$\begin{aligned} - \quad & \sigma\kappa + \frac{\Delta_{el}}{p}\Phi\left[\sigma^{\epsilon}_{ik}u^{(\alpha)}_{ik} - \frac{E\epsilon^2 B(\vec{x})}{2(1-\nu^2)}\right] \\ = \quad & -\frac{1}{\pi}\int_{-\infty}^{\infty} dx' \log\left[\frac{(x-x')^2 + (y(x)-y(x'))^2}{(x-x')^2 + \left(-\frac{x^2}{2} + \frac{x'^2}{2}\right)^2}\right]^{1/2} . \end{aligned} \tag{3.49}$$

We have introduced the solvability parameter $\sigma = d/pR$ here. Knowing the applied undercooling Δ and the elastic hysteresis Δ_{el}, it is the missing information to determine the desired quantities of the interface. Specifically, the velocity is determined as

$$\frac{\upsilon d}{D} = \frac{2}{\pi^2}\sigma\tilde{\Delta}^4 \tag{3.50}$$

and the radius of the asymptotically matching Ivantsov parabola R as

$$\frac{R}{d} = \frac{\pi}{\sigma\tilde{\Delta}^2}. \tag{3.51}$$

We now formulate our expectations concerning the solvability of the problem. Without the elastic contribution, we would deal with dendritic growth with isotropic surface tension. In the considered geometry, a smooth tip is prescribed. Consequently, the elastic effects lead to a new solvability mechanism if we observe a solvability parameter σ which does not vanish as the opening angle $\phi \to 0$. Here we define the angle ϕ as shown in Fig. 3.4.

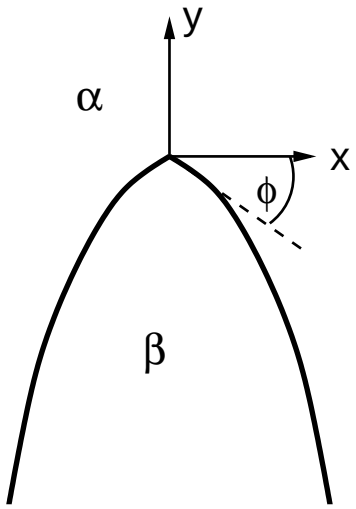

Figure 3.4: The opening angle ϕ is defined such that a smooth tip corresponds to $\phi = 0$, for the shown shape $\phi < 0$.

We will see that in the case of pure shear or dilatational eigenstrain, the single crystal growth will not exhibit a new selection mechanism due to the elastic effects. Solutions exist only for finite

slopes at the tip, and for $\phi \to 0$, we observe $\sigma(\Delta_{el}/p) \to 0$. The combination of dilatational and shear strain, however, shows a new selection mechanism. Here, the solvability parameter also exhibits a strongly combination-dependent behaviour. Specifically, the results indicate that the relative orientation of the lattice strains to the growth direction determines if there is a selection or not. The detailed description of the distinct configurations begins with the dilatational eigenstrain.

3.2.4 Dilatational Eigenstrain

Dilatational eigenstrain is the simplest elastic configuration to consider. We define the pure dilatation lattice strain in the onsetting phase (β) as

$$\epsilon_{ik}^{d} = \epsilon\delta_{ik}. \tag{3.52}$$

This lattice strain provides the possibility for comprehensive comparison of analytic and numerical results. Specifically, we show the absence of a selection by analytic considerations which we also support numerically. These analytic predictions base on an analogy of dilatational lattice strains and the inhomogeneous heating of a body.

Analytic Prediction: Absence of Solutions for Pure Dilatational Lattice Strain

We start from the equilibrium condition for a inhomogeneously heated body, given as [49]

$$0 = \frac{\partial\sigma_{ik}}{\partial x_k} = \left(-\frac{E\alpha}{3(1-2\nu)}\frac{\partial T}{\partial x_i} + \frac{E\nu}{(1+\nu)(1-2\nu)}\frac{\partial u_{ll}}{\partial x_i}\frac{E}{(1+\nu)}\frac{\partial u_{ik}}{\partial x_k}\right), \tag{3.53}$$

which is equal to

$$\frac{3(1-\nu)}{(1+\nu)}\nabla(\nabla\vec{u}) - \frac{3(1-2\nu)}{2(1+\nu)}\nabla\times\nabla\times\vec{u} = \alpha\nabla T. \tag{3.54}$$

Since the strain tensor is symmetric, it holds $\nabla\times\vec{u} = 0$. The coefficient of thermal expansion $\alpha = u_{ll}/(T-T_0)$ is defined as the ratio of volume change (Einstein sum convention) and difference between T, the applied temperature, and T_0, the temperature where no expansion due to heating occurs. The remaining representation of Eq. (3.54) reads as

$$\nabla(\nabla\vec{u}) = \frac{\alpha}{3}\frac{1+\nu}{1-\nu}\nabla T, \tag{3.55}$$

The analogy between the expansion due to heating and the constant dilatational eigenstrain means that we substitute $\alpha = \epsilon_{ll}/(T-T_0)$ for phase (β) and consider this ratio a constant for the subsequent integration of

$$\nabla(\nabla\vec{u}) = \frac{\epsilon_{ll}}{3}\frac{(1+\nu)}{(1-\nu)}\frac{1}{T-T_0}\nabla T. \tag{3.56}$$

This ratio $\epsilon_{ll}/(T-T_0)$ is constant in each phase, but more specifically it is the same in both phases. In the image of the heated body, we have just two areas which are heated to different temperatures, such that we can better understand that α is really the same in both phases. This sounds trivial, but

this point is crucial for the analogy.

To avoid a division by zero, one has to define a finite heating also in phase (α), corresponding to a lattice strain in (α). This is no problem as only the difference of the eigenstrains in (α) and (β) sets the effective lattice strain of the transition. Consequently, we may conduct the calculation we do for (β) also for (α). Now, we integrate the equation in x-direction from infinity to a point lying in the onsetting phase at $X(\beta)$ and assume the considered part of the interface to be parallel to the y-axis, see Fig. 3.5.

$$\int_{\infty}^{x(\beta)} dx \partial_x(\nabla \vec{u}) = \frac{\epsilon_{ll}}{3} \frac{(1+\nu)}{(1-\nu)} \frac{1}{T - T_0} \int_{\infty}^{x(\beta)} dx \partial_x T. \tag{3.57}$$

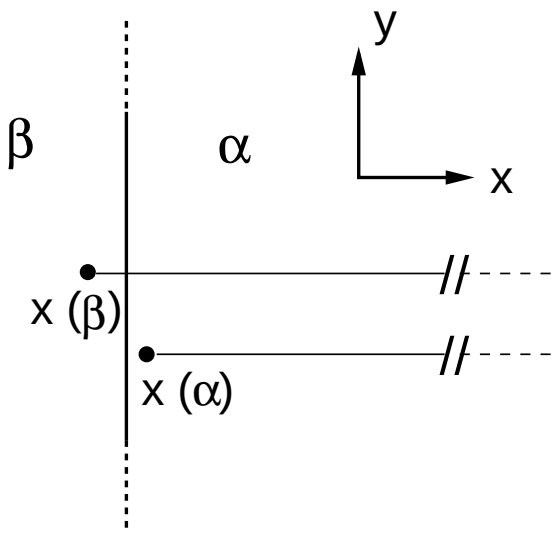

Figure 3.5: The integration paths for $\nabla \vec{u}$ in phases α, β. We integrate from $x \to \infty$ to $X(\alpha)$ and $X(\beta)$, respectively.

We set the constant offset temperature $T_0 = 0$ and take the analogue integration for the α-phase to a point $X(\alpha)$, see also Fig. 3.5, we obtain

$$\begin{aligned} \nabla \vec{u}^{(\beta)} &= \epsilon \frac{(1+\nu)}{(1-\nu)}, \\ \nabla \vec{u}^{(\alpha)} &= 0. \end{aligned} \tag{3.58}$$

The analogy between heating expansion and dilatational lattice strain thus yields the divergence of the displacement field in both phases. We can simplify the representation of $\delta \tilde{F}^{el}$ now, from Eq. (3.36),

$$\delta \tilde{F}^{el} = \sigma^{\epsilon}_{ik} u^{(\alpha)}_{ik} - 0.5 \frac{E}{1-\nu^2} (\epsilon^2_{\tau\tau} + \epsilon^2_{zz} + 2\nu \epsilon_{zz} \epsilon_{\tau\tau}), \tag{3.59}$$

we obtain, with $\epsilon_{ik} = \delta_{ik}\epsilon$,

$$\delta\tilde{F}^{el} = \frac{E}{(1-2\nu)}(u_{xx}^{(\alpha)} + u_{yy}^{(\alpha)}) - 0.5\frac{E}{1-\nu^2}(\epsilon_{\tau\tau}^2 + \epsilon_{zz}^2 + 2\nu\epsilon_{zz}\epsilon_{\tau\tau}). \tag{3.60}$$

We recall that we assume a plain strain situation, thus $u_{zz} = 0$, so the left part on the r.h.s. of Eq. (3.60) equals zero. The remaining difference of the elastic contributions of the modified free energyreads as

$$\delta\tilde{F}^{el} = -0.5\frac{E}{1-\nu^2}(\epsilon_{\tau\tau}^2 + \epsilon_{zz}^2 + 2\nu\epsilon_{zz}\epsilon_{\tau\tau}) = -\frac{E\epsilon^2}{1-\nu}. \tag{3.61}$$

Here, we applied the transformation of Eq. (3.60) to cartesian coordinates, see Eq. (3.39).

Finally, we yield the dimensionless notation of $\delta\tilde{F}^{el}$ as

$$\delta\tilde{F}_{el} = -\frac{T_{eq}c_p\epsilon^2 E}{(1-\nu)L^2}. \tag{3.62}$$

Eq. (3.62) shows the constant value of $\delta\tilde{F}^{el}$, due to which we can map the problem to classical dendritic growth with isotropic surface tension. The entire effect of $\delta\tilde{F}^{el}$ is a constant shift of the applied undercooling Δ. This consideration solves the complete elasto-diffusional problem, as it is known from classical dendritic growth [18] that isotropic surface tension prevents any physical solutions, i.e. those which exhibit smooth tips. Concluding, we can state that we obtain the absence of physical solutions, i.e. solutions with $\phi = 0$, by means of analytic considerations.

Numerical Results

The question arises in which sense we can obtain reasonable numerical results to support the predicted absence of solutions with $\phi = 0$. The appropriate method is the calculation of the solvability parameter $\sigma(\Delta_{el}/p, \phi)$ depending on the opening angle ϕ. We mention that here and also for all numerical simulations in other lattice configurations, the modulus of elasticity is $E = 1$ and the Poisson ratio $\nu = 1/3$.

With Eq. (3.62) in mind, we know that the term in Eq. (3.49), which enters with prefactor Δ_{el}/p, vanishes. The required coincidence of the taken values of σ for arbitrary Δ_{el}/p is obtained numerically. In Fig. 3.6, this is shown exemplarily for $\Delta_{el}/p = 0$ and $\Delta_{el}/p = 1$. Obviously, we obtain the expected absence of physical solutions, as for arbitrary Δ_{el}/p, the solvability parameter σ vanishes as $\phi \to 0$.

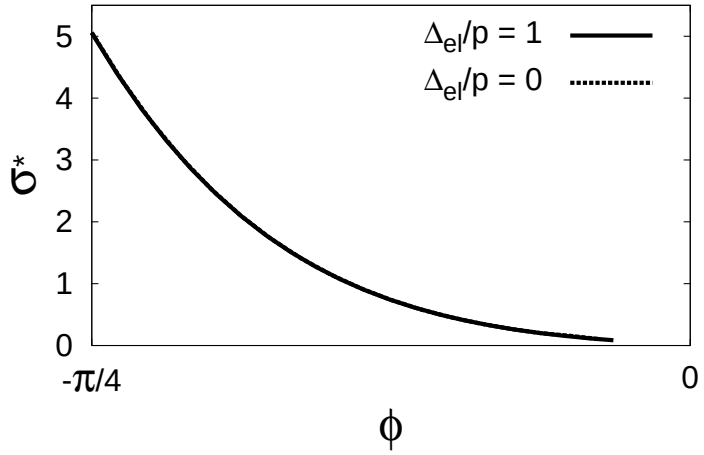

Figure 3.6: The solvability parameter σ vanishes as ϕ approaches 0. Here $\Delta_{el}/p = 1$ and $\Delta_{el}/p = 0$ show the same result, as required - since $\delta\tilde{F}^{el} \sim \Delta_{el}$, Eq. 3.49 is independent of Δ_{el}/p.

3.2.5 Pure Shear Eigenstrain

We return to Fig. 3.2, where the symmetry change due to the transition is illustrated. The angle which defines the orientation between old and new symmetry axis, ϑ, takes the values $\vartheta = 0, \pm 2\pi/3$. For $\vartheta = 0$, we consider the development of a single crystal with shear strain. Consequently, the concerning strain can be represented by the eigenstrain tensor

$$\epsilon^s_{ik} = \begin{pmatrix} -\epsilon & 0 & 0 \\ 0 & \epsilon & 0 \\ 0 & 0 & 0 \end{pmatrix}. \tag{3.63}$$

In contrast to the aforementioned dilatational eigenstrain, $\delta\tilde{F}^{el}$ does not approach Δ_{el} on the entire boundary. A comprising analytic prediction of the solution is thus not at hand. As for dilatation, we perform numerical calculations to consider the dependence of σ on the opening angle. We find absence of selection for shear lattice strain, i.e. the solvability parameter σ approaches 0 as $\phi \to 0$, see Fig. 3.7.

Besides the absence of selection for dilatation, we also see that shear lattice strains do not operate as selection mechanism. Although both fundamental modes of deformation do not lead to selection, we shall see in the next section that their superposition exhibits a new selection mechanism.

The reliability of our results is strongly supported by the various checks we conducted. The discontinuities of the elastic fields given in Eqs. (3.22) to (3.24) could be obtained as well as $T_{eq}c_P\delta\tilde{F}^{el}/L^2 \to \Delta_{el}$ for $x \to \infty$. The latter also allows to evaluate the length cutoff as reasonable, which is as well indicated by the parabolic approximation of our solutions we obtain. As $T_{eq}c_P\delta\tilde{F}^{el}/L^2 \to \Delta_{el}$ and $\kappa \to 0$ asymptotically, the solution in that region must be close to the Ivantsov solution, $y_{Iv} = -x^2/2$. The parabolas by which we match the tail region of the interface exhibit a coefficient of the quadratic term close to $-1/2$, as required. The numerical stability of the

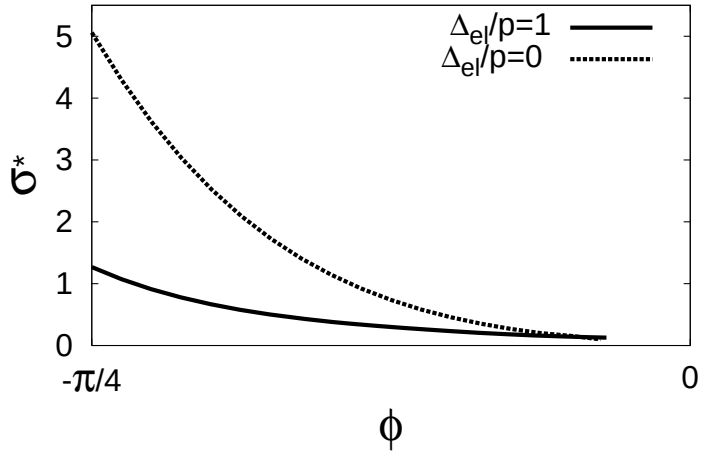

Figure 3.7: The solvability parameter σ vanishes as the opening angle ϕ approaches 0. Here $\Delta_{el}/p = 1$ and $\Delta_{el}/p = 0$ are compared. Obviously, the non-constant part of $\delta\tilde{F}^{el}$ in this case also suppresses selection.

results versus reasonable modifications of the numerical parameters can be stated for grid resolutions which can vary up to an order of magnitude, and approximatly the same holds for the system length.

3.2.6 Superposition of Pure Shear and Dilatational Eigenstrain

We discuss the occurence of a solvability mechanism due to a superposition eigenstrain. Here superposition eigenstrain means an eigenstrain $\epsilon^{\pm}_{ik}$ which is expressed as combination of pure shear and pure dilatational eigenstrain such that

$$\epsilon^{\pm}_{ik} = \eta\epsilon^{d}_{ik} \pm (1-\eta)\epsilon^{s}_{ik}. \tag{3.64}$$

The mixing parameter η yields a continuous mixing from pure shear eigenstrain, $\eta = 0$ to pure dilatation eigenstrain, $\eta = 1$, at $\eta = 1/2$ yielding the same weight of both eigenstrain types. The change of sign in Eq. (3.64) corresponds to a rotation of the growth direction relative to the lattice strain by $\pi/2$. It turns out that this relative orientation (ϵ^{+}_{ik} or ϵ^{-}_{ik}) determines whether there is selection or not. The occurence of selection is already surprising, as the separate modes of shear and dilatational strain could not exhibit new selection mechanisms. The case drawing our attention corresponds to ϵ^{-}_{ik}, which reads as

$$\begin{pmatrix} \epsilon & 0 & 0 \\ 0 & \epsilon(2\eta-1) & 0 \\ 0 & 0 & \eta\epsilon \end{pmatrix}. \tag{3.65}$$

We will first consider the behaviour of $\sigma(\Delta_{el}/p)$ for different fixed η before we turn to fixed Δ_{el}/p and vary η. The latter yields which lattice deformations lead to the fastest transitions, as σ is a

dimensionless velocity, $\upsilon \sim \sigma p^2$.

When we have a look at Fig. 3.8, we recognize the magnitude of the solvability parameter we calculated. At least for $\eta = 0.3$ and $\eta = 0.5$, we obtain values which are much larger than the values which occur in classical dendritic growth. The resulting velocities scale proportional to σ, (3.50) thus the transformations proceed much faster.

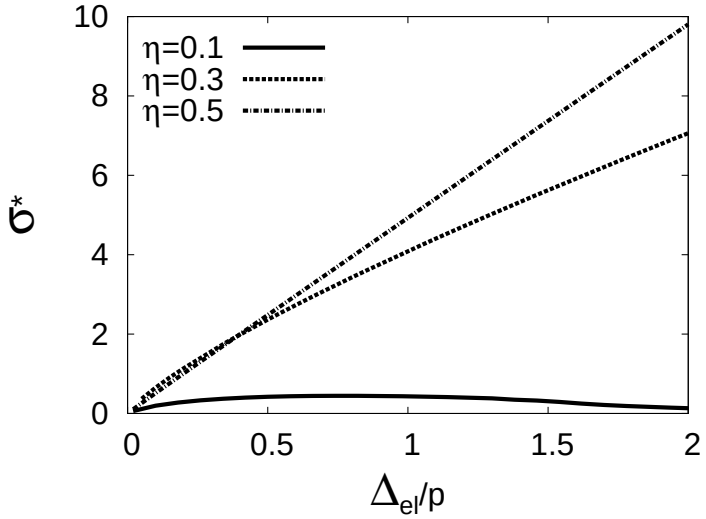

Figure 3.8: The solvability parameter $\sigma(\Delta_{el}/p)$ for varying mixing of dilatational and pure shear eigenstrain. Increasing of the mixing parameter up to roughly symmetric mixing leads to increasing growth velocities, as σ can be interpreted as dimensionless growth velocity.

The dependence of the selection on the mixing parameter is investigated for $\Delta_{el}/p = 1$. The results in Fig. 3.9 show a maximum at $\eta \approx 0.4$. When we obtain Δ_{el} for this configuration,

$$\Delta_{el} = \frac{T_{eq} c_p \epsilon^2 E \left((2\eta - 1)^2 + \eta^2 + 2\nu\eta(2\eta - 1)\right)}{2(1 - \nu^2)L^2}, \tag{3.66}$$

we see it is minimal at $\eta^* = 7/19 \approx 0.37$, for the Poisson ratio we choose $\nu = 1/3$. Asymptotically, the elastic hysteris thus leads to the smallest shift of the applied undercooling for $\eta = \eta^*$. Though the position of the maximum in Fig. 3.9 and the minimal asymptotic hysteresis are close, it is unclear if it is this effect which dominates the position of the maximum. The next question which comes up concerns the stability of the found solutions - as the method we apply cannot yield the dynamics of the system, we refer to calculations performed with phase field code by Michael Fleck in our group.

Comparison of Green's Function Method and Phase Field Method The comparison requires some introductory words. Subject of investigation of the phase field approach was the growth of a finger in a channel. It is well-known that this geometry in solidification exhibits selection different to that in free growth [45], but the comparison can be reasonable under certain restrictions. The geometry of the channel is shown in Fig. 3.10, and we shall briefly define the

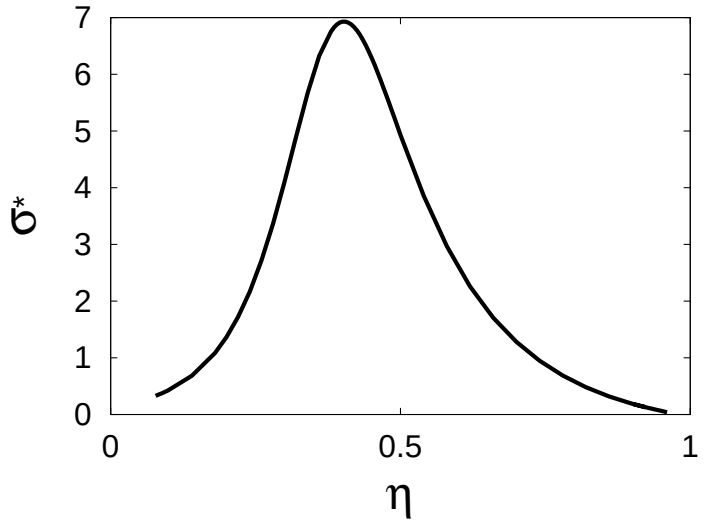

Figure 3.9: The solvability parameter σ depending on the mixing parameter η for $\Delta_{el}/p = 1$. Roughly at symmetric mixing, the maximum of the solvability parameter is found.

necessary quantities here. The presence of walls in the system introduces a new length scale, the system width W, and the relative width of the finger in its tail region is labelled λ.

The boundary conditions on the walls include thermal insulation, $\partial_x w = 0$, and constant displacements $u_x = 0,\ u_y = 0$. The latter means that far ahead of the tip in phase α, the system is elastically relaxed. In that region, the temperature is the applied undercooling Δ, which we defined for the free geometry. We skip a more detailed description of this system, as the differences to the free geometry explained up to here suffice to understand the assumed simplifications for the channel geometry we discuss in the following. These simplifications are required to allow the comparison of both geometries. Basically, the phase field simulations here restrict to symmetrized systems as we do, meaning equal thermal and elastic properties in both phases. Furthermore, the ratio of finger width to channel width, λ, must be sufficiently small, as the propagating finger exhibits a less strong 'recognition' of the walls when they are appreciably distant. With this restrictions in mind, we consider the outcome of both methods in Fig. 3.11. Obviously, we find good agreement when we focus on the regime of small λ. Since the phase field method showed stable behaviour in that regime, we can assume that the solutions we found also are stable.

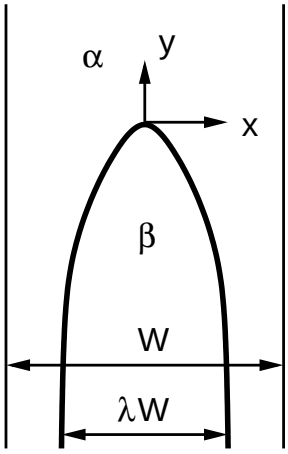

Figure 3.10: Sketch of the channel system geometry. The system has width W and is infinitely long. The finger is wide as λW in its tail region, thus the ratio of finger width to channel width is simply λ. The β phase grows at expense of phase α in y-direction.

3.2.7 Special Case of Eigenstrains with Vanishing Elastic Hysteresis

Among all eigenstrain configurations which we discussed before, the presence of the elastic hysteresis, represented by Δ_{el}, reduced the applied driving force Δ to the effective driving force $\tilde{\Delta} = \Delta - \Delta_{el}$. If we allow the possibility of a free orientation of the growing shape, we see that for a rotation of $\vartheta = 45°$, see Fig. 3.2 for the definition of ϑ, we can consider a single crystal with a corresponding eigenstrain tensor

$$\epsilon_{\mathbf{ik}} = \epsilon \begin{pmatrix} 0 & 1 & 0 \\ 1 & 0 & 0 \\ 0 & 0 & 0 \end{pmatrix},$$

which gives $\Delta_{el} = 0$. Obviously, if it existed, this configuration would be energetically preferential. Results of phase-field simulations [83, 85, 86, 84] also suggest to search for steady-state solutions in the case of $\vartheta = 45°$. The observed growing phases within these simulations seem to show qualitative agreement with our predicted steady-state solutions. However, these results emanate from simulations pertaining to models which include different features of elastic interactions. For instance, the simulated system contains several growing new phases, and incorporates elastic interaction between those. Also, we cannot judge whether and how the shown phase field results are relaxed up to the decay of oscillations, i.e. if steady-state is really reached. Apart from this question of comparability to other results, the question arises if we can consider this system without dropping our assumptions concerning the symmetry of the shape.

Dropping Symmetry at Vanishing Elastic Hysteresis At first glance, the symmetry assumption concerning the interface shape appears to be dropped for finding this solution. When we consider the elastic forces due to the eigenstrains,

$$\int_V F_i^{\epsilon} dV \quad = \quad \oint_{\partial V} \sigma_{ik}^{\epsilon} n_k ds, \tag{3.67}$$

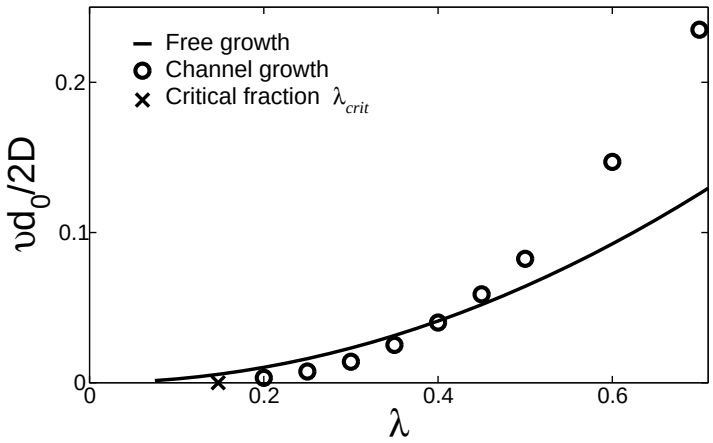

Figure 3.11: Comparison of free growth and channel growth. The dimensionless growth velocity is plotted versus λ, the superposition of dilatation and shear is symmetric, $\eta = 0.5$. The elastic hysteresis is set to $\Delta_{el} = 0.05$. By critical fraction λ_{crit} the minimum value of λ for positive velocities is labelled.

their y-component switches sign when we switch the point of observation from one side along the growth direction onto the other side:

$$\int_V F_y^\epsilon dV = \oint_{\partial V} \frac{E}{1+\nu}\epsilon_{yx} n_x ds, \tag{3.68}$$

here n_x changes sign from one side to the other. However, the closed representation which defines the solution of the problem reads as

$$\begin{aligned} \Delta - & \frac{d\kappa}{R} + \frac{T_{eq}c_p}{L^2}\left[\sigma_{ik}^\epsilon u_{ik}^{(\alpha)} - \frac{E\epsilon^2 B(\vec{x})}{2(1-\nu^2)}\right] \\ = & \frac{p}{\pi}\int_{-\infty}^{\infty} dx' \exp[-p(y(x)-y(x'))]K_0(p\eta(x,x')), \end{aligned} \tag{3.69}$$

thus we have to consider the term $\left[\sigma_{ik}^\epsilon u_{ik}^{(\alpha)} - (E\epsilon^2 B(\vec{x}))/2(1-\nu^2)\right]$. For the local part, the definition of $B(\vec{x})$ in Eq. (3.39) show that $B \sim n_x^2 n_y^2$, which is symmetric, and for the nonlocal part $\sim \sigma_{ik}^\epsilon u_{ik}^{(\alpha)}$ we perform an asymptotic estimation. The only nonvanishing term for the discussed case is $\sim \sigma_{xy} u_{xy}^{(\alpha)}$, so we calculate the strain $u_{xy}^{(\alpha)}$ for two lines parallel to the y-axis from 0 to $-\infty$, which represent the asymptotic interface. The lines are $(-1, y)$ and $(1, y)$, the point of observation is $(x, 0)$. The resulting formal solution of the strains $u_{ik}^{(\alpha)}$ reads as

$$\begin{aligned} u_{xy}^{(\alpha)} &= -\frac{\epsilon}{4\pi(1-\nu)}\int ds' \frac{1}{|\vec{r}-\vec{r}'|^4} \times \\ &\quad \Big(2(x-x')(y-y')(f_x(x-x') + f_y(y-y')) + (1-2\nu)|\vec{r}-\vec{r}'|^2(f_x(y-y') + f_y(x-x'))\Big), \\ f_i &= \frac{1+\nu}{E\epsilon}\sigma_{ik}^\epsilon n_k. \end{aligned} \tag{3.70}$$

We substitute the expressions for the normals, $n_x = -y'(x)/\sqrt{(1+(y'(x))^2)}$, $n_y = 1/\sqrt{(1+(y'(x))^2)}$, yielding

$$\begin{aligned} u_{xy}^{(\alpha)} &= -\frac{\epsilon}{4\pi(1-\nu)}\left[\int_{-\infty}^{\infty} dy' \frac{1}{|\vec{r}-\vec{r}'|^4}\left(2(x-1)(-y')^2 + (1-2\nu)|\vec{r}-\vec{r}'|^2(x-1)\right)\right] \qquad (3.71)\\ &+ -\frac{\epsilon}{4\pi(1-\nu)}\left[\int_{\infty}^{-\infty} d(-y') \frac{1}{|\vec{r}-\vec{r}'|^4}\left(2(x+1)(-y')y' + (1-2\nu)|\vec{r}-\vec{r}'|^2(-(x+1))\right)\right]. \end{aligned}$$

The obtained integrals belong to the standard cases

$$\int dx \frac{1}{p^2+x^2} = \frac{1}{p}\arctan\frac{x}{p} \qquad (3.72)$$

$$\int dx \frac{x^2}{(p^2+x^2)^2} = \frac{-x}{2(x^2+p^2)} + \frac{1}{2p}\arctan\frac{x}{p}, \qquad (3.73)$$

where on the left boundary, represented by the line $(-1, y)$, it is $p = x - 1$, and the right boundary $(1, y)$ corresponds to $p = x + 1$. With $\arctan(x) \to \pm\pi/2 \quad$ when $\quad x \to \pm\infty$, we arrive at

$$\begin{aligned} u_{xy}^{(\alpha)} &= -\frac{\epsilon}{4\pi(1-\nu)}\left[-(x-1)\left(\frac{b}{b^2+(x-1)^2} - \frac{a}{a^2+(x-1)^2}\right)\right] \qquad (3.74)\\ &+ -\frac{2(1-\nu)\epsilon}{4\pi(1-\nu)}\left[\arctan\left(\frac{b}{x-1}\right) - \arctan\left(\frac{a}{x-1}\right)\right] \qquad (3.75)\\ &+ \frac{\epsilon}{4\pi(1-\nu)}\left[(x+1)\left(\frac{a}{a^2+(x+1)^2} - \frac{b}{b^2+(x+1)^2}\right)\right] \qquad (3.76)\\ &+ -\frac{2(1-\nu)\epsilon}{4\pi(1-\nu)}\left[\arctan\left(\frac{a}{x+1}\right) - \arctan\left(\frac{b}{x+1}\right)\right], \qquad (3.77) \end{aligned}$$

here $a \to -\infty$ and $b \to \infty$ are the ranges of integration. The resulting behaviour for $u_{xy}^{(\alpha)}$, depending on whether the point of observation is in the new phase, $-1 < x < 1$, or not, is given by

$$\begin{aligned} u_{xy}^{(\alpha)} &\to -\frac{1}{2\pi}(-\pi - \pi) = \epsilon \quad | \quad |x| < 1 \qquad (3.78)\\ u_{xy}^{(\alpha)} &\to -\frac{1}{2\pi}(\pi - \pi) = 0 \quad | \quad |x| > 1. \end{aligned}$$

Concluding, Eqs. (3.78) show that the relevant strain field $u_{ik}^{(\alpha)}$ is symmetric - in conjunction with the symmetry of the local contributions to $\delta\tilde{F}^{el}$, we do not drop the assumption of a shape symmetric along the growth direction. We may apply the implementation of the system which we used up to here - and that effectively only requires the computation of the right half of the shape.

Numerical Solution and Discussion Again, we focus on the most relevant regime of $p \ll 1$, and the most convenient notation of the problem reads as

$$-\sigma\kappa + \alpha\left(\bar{u}_{xy}^{(\alpha)} - \frac{1}{2}\frac{B(\vec{x})}{1-\nu}\right) = -\frac{1}{\pi}\int_{-\infty}^{\infty} dx' \log\left[\frac{(x-x')^2 + (y(x)-y(x'))^2}{(x-x')^2 + (\frac{x^2}{2}+\frac{x'^2}{2})^2}\right]^{1/2},$$

where $\bar{u}_{xy}^{(\alpha)} = u_{xy}^{(\alpha)}/\epsilon$, the quantity $\alpha = (T_{eq}c_pE\epsilon^2)/(pL^2(1+\nu))$ is the measure for the ratio of the strength of the elastic effects and the driving force. As before, $\sigma = d/pR$ is the solvability parameter. The numerical results for the integro-differential equation in the introduced case of $\vartheta = \pi/4$ suggest the absence of steady-state solutions, as one can take from Fig. 3.12.

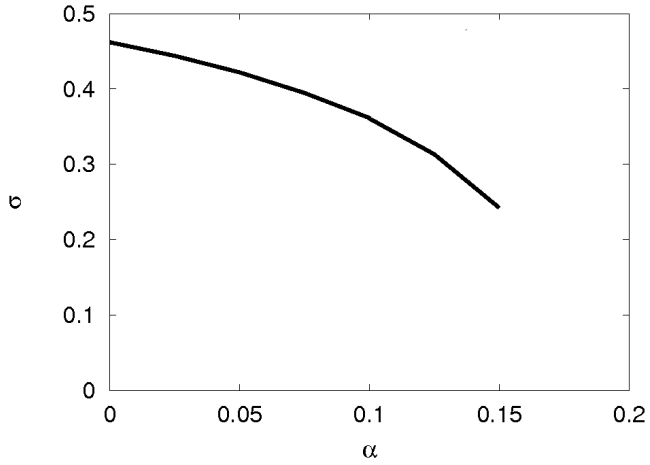

Figure 3.12: The solvability parameter $\sigma(\alpha)$ for $\vartheta = \pi/4$ and $\phi = 22°$. The elastic effects reduce the solvability parameter, indicating absence of a physical solution for a smooth tip.

Though a continuation of the decreasing behaviour of $\sigma(\alpha)$ to $\sigma \to 0$ could not be resolved numerically, the occurence of accretive elastic effects seems to inhibit solvability here. The shown plot, for an opening angle of $\phi = 22°$, is part of an appropriate procedure for the determination of the sovability; The boundary condition of vanishing slope at the tip is relaxed to see whether one finds the necessary - meaning that $\partial\sigma/\partial\alpha > 0$ - behaviour of the system concerning the presence of a selection mechanism. In such case, one would increase α to a certain level and then see if σ remains finite as $\phi \to 0$. However, as here both $\sigma(\phi)_{|\,\alpha}$ and $\sigma(\alpha)_{|\,\phi}$ are decreasing functions, absence of a selection mechanism is likely.

3.2.8 Conclusion

We introduced a model for solid-solid transitions limited by diffusion of the latent heat set free at the moving interface and influenced by the lattice strains in the onsetting phase. The occurence of the elastic aspect of the transition appears to massively complicate the problem. However, we introduce simplifying assumptions which allow to set up a closed representation of the moving boundary problem. Specifically, the elastic problem is assumed to be static on the timescale of the thermal problem. Consequently, the elastic-diffusional problem decouples up to the local equilibrium, where the interface temperature is shifted due to the lattice strains and the Gibbs-Thomson effect. Furthermore, the elastic aspect is simplified as we assume isotropic plain strain. In addition, both phases shall exhibit the same elastic constants and diffusion constants. In conjunction, this novel ansatz yields a closed formulation of the elastic-diffusional free boundary problem, which states an integro-differential equation. The variety of lattice strains we discuss here corresponds to an onsetting single crystal structure, which has the advantage to exclude the selection due to a triple junction. For the solution of this nontrivial equation, we distinguish three cases, corresponding to the lattice strains configurations in the creating phase.

In the case of dilatational lattice strain, we could solve the problem analytically - we found an analogy to the expansion of an inhomogeneously heated body and thus could map the problem to classical dendritic growth, where it is known that isotropic surface tension does not yield physical solutions. This prediction is supported by the outcome of the numerical investigations we performed. Dilatational lattice strain does not operate as selection mechanism in free elastic-diffusional growth with isotropic surface tension. The numerical investigations about shear lattice strain also exhibited the absence of selection. There is no mapping at hand to classical dendritic growth yet, but the successful tests we conducted for the numerical code suggest the correctness of our results.

The most interesting mode of lattice deformation is the superposition of dilatational and shear eigenstrain. Here we found that the elastic effects due to the lattice strain can induce a selection mechanism - provided there is a certain orientation of the growth direction relative to the lattice strains. The magnitude of the solvability parameter indicates that the transition velocity of the corresponding transformations are much higher than in classical dendritic growth. The comparison with phase field simulations showed that the found solutions are dynamically stable.

Apart from this discrimination by fundamental types of lattice strain, we also numerically investigated the specific case of vanishing elastic hysteresis. Obviously, being an energetically preferential mode of transition, it deserves specific consideration. We find that the necessary rotation does not break our symmetry assumptions, but the conducted calculations indicate that there is no corresponding steady-state solution.

3.3 Bicrystal Diffusional Solid-Solid Transition in Presence of Lattice Strains

The model we stated in the previous section concerned single crystal growth. In this section, we explain an extension to transitions which develop into a bicrystal geometry. As shown in [17], the bicrystal is more likely to be observed than the single crystal since the gain of free energydue to the transition is larger. This renders the bicrystal geometry a very promising subject to consider.

We assume that the various symmetry assumptions we imposed in the single crystal geometry are also satisfied here. The choice of the lattice strains again corresponds to [31] as well. In the bicrystal geometry, the presence of the triple junction leads to a perturbation which already leads to a selection with isotropic surface tension, as was shown in [16] and briefly discussed in subsection 2.4.2. The influence of the elastic effects on a present selection is an interesting subject, but first we want to investigate if elastic effects lead to a selection without the effect of the triple junction. Both regimes will be covered in the subsequent part of this section.

For that purpose, we distinguish between nearly equal interface energies $\gamma_b \sim \gamma$, and the case $\gamma_b \ll \gamma$. Here we denote the twin boundary surface energy by γ_b and the interface surface energy by γ. We consider a smooth tip for $\gamma_b \ll \gamma$ and a finite slope for $\gamma_b \sim \gamma$. The smooth tip will reveal the selection due to elastic effects in case of vanishing influence of the triple junction, the configuration with finite slope will show the interaction of selection by the triple junction and the elastic effects.

We express our expectations concerning the occurence of selection for the bicrystal geometry. A new selection mechanism in the bicrystal geometry due to the elastic effects implies that we find solvability, i.e. $\sigma \neq 0$, when we consider a 'weak' triple junction, $\gamma_b \ll \gamma$, meaning a smooth tip. Here the solvability parameter σ is defined the same way as in the single crystal geometry. Briefly said, the shear eigenstrain will exhibit a new selection mechanism, as well as the mixed eigenstrain configuration which combines dilatational and shear eigenstrain. Additionaly, the influence of the triple junction will exhibit probably unstable solution branches of the solvability parameter.

Subsection 3.3.1 starts with a short description of the system, where we concentrate on the changes in the model due to the bicrystal growth mode. This provides the necessary representations to state the closed formulation of the problem. For the specific lattice configurations, **subsection** 3.3.2 contains the investigations on the shear lattice strain, and **subsection** 3.3.3 the superposition of shear and dilatation. Furthermore, **subsection** 3.3.4 will describe the model and results we obtained for the limit of zero velocity of the transition.

3.3.1 Brief Derivation of the Problem

We give a compact derivation of the considered equation, with focus on the aspects which are new compared to the formulation of the problem in a single crystal geometry, as it was described in the previous section. We apply the Green's function method to obtain an evolution equation for the interface. For this purpose, we find the integral representations of the thermal field w and the difference of the elastic contributions of the free energydensities, $\delta\tilde{F}^{el}$. The derivation of the integral representation of the thermal field is described in the previous section, see subsection 3.2.1, and only a brief review is given here. But we discuss in detail the changes in the derivation of $\delta\tilde{F}^{el}$, the elastic part of the difference of the modified free energies in both phases. Like in the previous section, we start with the diffusional aspect of the problem. The diffusion equation in a

co-moving frame of reference located at the tip of the transition interface reads in dimensionless notation as

$$\nabla^2 w + \frac{2}{l_D}\frac{\partial w}{\partial y} = 0, \tag{3.79}$$

where $l_D = 2D/\upsilon$ defines the diffusion length with thermal diffusion constant D and υ the constant growth velocity. We define the temperature field

$$w = c_P \frac{T - T_\infty}{L}$$

where T_∞ is the applied temperature far away from the interface in the reference phase. By Δ we label the undercooling,

$$\Delta = c_P \frac{T_{eq} - T_\infty}{L},$$

it denotes the control temperature of the process, where T_{eq} is the equilibrium transition temperature without elastic hysteresis and Gibbs-Thomson effect. The latent heat per unit volume is L and the heat capacity is c_P. The Stefan condition of the moving boundary problem is given by the conservation of heat,

$$\upsilon_n = -D\vec{n}\left(\nabla w_\alpha - \nabla w_\beta\right)_{|int}. \tag{3.80}$$

Here υ_n is the normal component of the interface velocity, and the normal vector $\vec{n}$ points into the reference phase (α). By the index $|int$ we indicate that the difference of the gradients has to be taken at the interface. Local equilibrium includes the Gibbs-Thomson condition and the elastic contribution to the difference of the modified free energy densities $\delta\tilde{F}^{el}$, such that

$$w_{|int} = \Delta - d\kappa + \frac{T_{eq}c_p}{L^2}\delta\tilde{F}^{el}. \tag{3.81}$$

Here, we rescaled all lengths by the tip radius of curvature R, and by

$$d = c_P \frac{T_{eq}\gamma}{L^2},$$

we introduce the capillarity length, where γ is the surface tension and κ the curvature. The effect of the bicrystal geometry, apart from the presence of the triple junction, appears in the explicit representation of $\delta\tilde{F}^{el}$, and like in section 3.2.2, we assume a symmetric elastic model. This means that the elastic constants E, ν are identical in both phases. Furthermore, we separate the eigenstrain in both phases as

$$\tilde{\sigma}_{ik}^{(i)} = \sigma_{ik}^{(i)} + \sigma_{ik}^{\epsilon(i)}, \tag{3.82}$$

where

$$\sigma_{ik}^{\epsilon(i)} = \frac{E}{1+\nu}\left(\epsilon_{ik}^{(i)} + \frac{\nu}{1-2\nu}\delta_{ik}\epsilon_{ll}^{(i)}\right) \tag{3.83}$$

is the stress related to the eigenstrains, and $\tilde{\sigma}_{ik}^{(i)}$ is the eigenstrain-independent stress. By E and ν we denote the elastic modulus and the Poisson ratio, by $i = \alpha, \beta$ we indicate the phase. Now, in terms of $\tilde{\sigma}_{ik}^{(i)}$, satisfying the mechanical equilibrium requires the definition of artificial force densities F_k on the interface. This ansatz was introduced in detail in section 3.2.2 for the $\alpha - \beta$ interface. Here we explain the outcome of this ansatz for the bicrystal geometry, specifically for the twin boundary.

Elastic Effects of the Twin Boundary

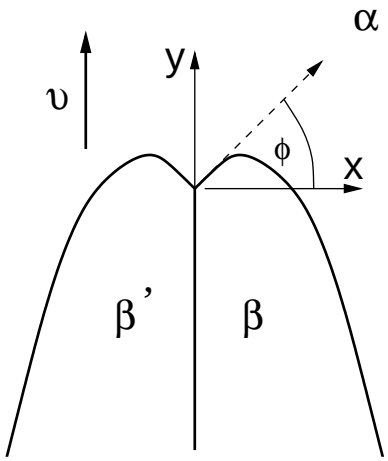

Figure 3.13: The bicyrstal grows on expense of phase (α) with constant velocity υ parallel to the y-axis. The Twin phases (β) and (β') differ by the orientation of the eigenstrains, where $\vartheta = 2\pi/3$ in phase β and $\vartheta = -2\pi/3$ in phase β'. The angle ϑ is illustrated in Fig. 3.2. The twin boundary Γ_{twin} is placed on the negative part of the y-axis, by ϕ we denote the opening angle, here $\phi = 0$ defines a smooth tip. Young's law fixes the opening angle as $\sin\phi = \gamma_b/2\gamma$.

The growth of a bicrystal extends the integral representation of the strains by terms from the twin boundary. These artificial stresses come from the different orientation of the eigenstrains in the twin phases, as it is shown in the following calculation. Additional to Eq. (3.82), we obtain

$$\frac{\partial \tilde{\sigma}_{ik}^{(\beta')}}{\partial x_k} = 0 \tag{3.84}$$

for bicrystal growth. Thus, from the condition of mechanical equilibrium on the twin interface, we obtain artificial forces as we did for the ($\alpha - \beta$) boundary in the single crystal geometry. Considering the y-component exemplarily, the mechanical equlibrium yields for the y-component

$$\int dy \left[\sigma_{yx}^{(\beta)} - \sigma_{yx}^{(\beta')}\right] n_x = 0, \tag{3.85}$$

since $n_y = 0$ along the twin boundary. The representation of the elastostatic Eqs. (3.82) thus takes

the form

$$\left(\tilde{\sigma}_{yx}^{(\beta)} - \tilde{\sigma}_{yx}^{(\beta')}\right) n_x = F_y. \tag{3.86}$$

Explicitly, we obtain

$$F_y = \frac{E}{1+\nu} 2\epsilon_{xy}, \tag{3.87}$$

the analogue consideration for F_x gives $F_x = 0$. As the coordinate system is chosen such that the twin boundary is located on the negative part of the y-axis, the expressions for the additional contributions to the strains simplify and can be calculated by hand. The additional integrand for the strain u_{xx} along the twin boundary Γ_{twin} reads as

$$u_{xx}^{\Gamma_{twin}} = \frac{1+\nu}{4\pi(1-\nu)E} \int_0^{y_{Max}} \frac{1}{r^4} F_y Y (Y^2 - X^2) dy'. \tag{3.88}$$

Here, analytically $y_{Max} \to -\infty$ and we denote by $X = x - x'$, by $Y = y - y'$. We obtain

$$u_{xx}^{\Gamma_{twin}} = -\frac{1}{2} F_y \frac{1+\nu}{4\pi(1-\nu)E} \left[\frac{2x^2}{x^2+Y^2} + \ln \|Y^2 + x^2\| \right]_y^{y-y_{Max}}. \tag{3.89}$$

We see that the effect of the twin boundary can be treatet comfortably with some simple integrals. Like for $u_{xx}^{\Gamma_{twin}}$, we also obtain the additional term in the integral representation of u_{yy}. We write:

$$u_{yy}^{\Gamma_{twin}} = \frac{1+\nu}{4\pi(1-\nu)E} \int_0^{y_{Max}} \frac{1}{r^4} F_y Y [(X^2 - Y^2) - 2(1-2\nu) r^2] dy', \tag{3.90}$$

and by the same procedure as for u_{xx}, we obtain that

$$u_{yy}^{\Gamma_{twin}} = \frac{1}{2} F_y \frac{1+\nu}{4\pi(1-\nu)E} \left[(1 + 2(1-2\nu)) \ln(Y^2 + x^2) + 2x^2 \left(\frac{1}{Y^2 + x^2} \right) \right]_y^{y-y_{Max}}. \tag{3.91}$$

For the twin boundary contribution to u_{xy}, we see that

$$u_{xy}^{\Gamma_{twin}} = \frac{1+\nu}{4\pi(1-\nu)E} \int_0^{y_{Max}} \frac{1}{r^4} F_y X [2Y^2 + (1-2\nu) r^2] dy' \tag{3.92}$$

gives

$$u_{xy}^{\Gamma_{twin}} = F_y \frac{1+\nu}{4\pi(1-\nu)E} \left[(2-2\nu) A_1(x,y,y') - A_2(x,y,y') \right]_0^{y_{Max}}, \tag{3.93}$$

where the functions $A_1(x,y,y')$ and $A_2(x,y,y')$ are defined as

$$A_1(x,y,y') = \arctan\left(\frac{y-y'}{x} \right) \tag{3.94}$$

and

$$A_2(x,y,y') = x\left(\frac{y-y'}{(y-y')^2+x^2}\right). \tag{3.95}$$

Eqs. (3.89) to (3.95) state the additional contributions in the integral representations of the strains, which we recall to be

$$u_{im} = \frac{1}{2}\int ds'\left(\frac{\partial g_{mk}}{\partial x_i} + \frac{\partial g_{ik}}{\partial x_m}\right)F_k. \tag{3.96}$$

Consequently, the representation of $\delta\tilde{F}^{el}$ as functional of the interface,

$$\delta\tilde{F}^{el} = \left[\sigma^{\epsilon}_{ik}\epsilon^{(\alpha)}_{ik} - \frac{E}{2(1-\nu^2)}(\epsilon^2_{\tau\tau} + \epsilon^2_{zz} + 2\nu\epsilon_{\tau\tau}\epsilon_{zz})\right](x, y(x)), \tag{3.97}$$

is now completely defined for the bicrystal geometry in the desired way.

Closed Formulation

Supported with the definition of the difference of the chemical potential $\delta\tilde{F}^{el}$, we obtain the closed formulation in this part. In Eq. (3.81), the thermal field is substituted by its Green's function integral representation, see section 2.4.1 for a detailed discussion, as

$$w(\vec{x}) = \frac{\upsilon}{D}\int_{-\infty}^{\infty} dx' g(\vec{r}, \vec{r}'),$$

where

$$g(\vec{r}, \vec{r}') = \frac{1}{2\pi}\exp\left(-\frac{1}{l_D}(y-y')\right)K_0\left(\frac{1}{l_D}\eta(x,x')\right),$$

is the free space Green's function for (3.79), and K_0 is a modified Bessel function. By η we label the distance of the points $\vec{x} - \vec{x}'$, $\eta = \|\vec{x} - \vec{x}'\|$. Here the diffusion length l_D relates to the Peclet number p and the Radius R as

$$p = \frac{R}{l_D}. \tag{3.98}$$

We remember that R is the tip radius of curvature of the Ivantsov parabola which is asymptotically matched by the solutions which we obtain. The Peclet number itself is implicitly determined by the dimensionless shifted undercooling $\tilde{\Delta}$ as

$$\tilde{\Delta} = (p\pi)^{1/2}\exp(p)erfc(p^{1/2}), \tag{3.99}$$

where the shifted undercooling is defined as $\tilde{\Delta} = \Delta - \Delta_{el}$. Here, by Δ we denote the dimensionless undercooling as it is known from free dendritic growth without elastic effects, defined by Eq. (3.80). By Δ_{el} we denote the dimensionless asymptotic shift of the equilibrium temperature due to

the elastic effects, defined as

$$\Delta_{el} = \frac{1}{2}\frac{T_{eq}c_p E}{(1-\nu^2)L^2}(\epsilon_{yy}^2 + \epsilon_{zz}^2 + 2\nu\epsilon_{yy}\epsilon_{zz}). \tag{3.100}$$

In an experimental setup, one would set T_∞, which fixes the undercooling Δ. Then, the elastic effects lead to a shifted Δ, which is $\tilde{\Delta}$, and which we could measure on the interface in the asymptotic region $|x| \to \infty$, where the curvature $\kappa \to 0$, and $\delta\tilde{F}^{el} \to \Delta_{el}L^2/T_{eq}c_p$. For the closed dimensionless representation of equations (3.81) and (3.97) we obtain

$$\Delta - \frac{d\kappa}{R} + \frac{T_{eq}c_p\delta\tilde{F}^{el}}{L^2} = \frac{p}{\pi}\int_{-\infty}^{\infty} dx' \exp[-p(y(x)-y(x'))]K_0(p\eta(x,x')), \tag{3.101}$$

where we rescaled all lengths by the tip radius of curvature R. In the relevant regime of small undercoolings, when the approximation for the Peclet relation and the Bessel function, see Eqs. (3.45) and (3.46), are legitimate, we obtain

$$\begin{aligned} &- \sigma\kappa + \frac{\Delta_{el}}{p}\Phi\left[\sigma_{ik}^{\epsilon}u_{ik}^{(\alpha)} - \frac{E\epsilon^2 B(\vec{x})}{2(1-\nu^2)}\right] \\ &= -\frac{1}{\pi}\int_{-\infty}^{\infty} dx' \log\left[\frac{(x-x')^2 + (y(x)-y(x'))^2}{(x-x')^2 + \left(-\frac{x^2}{2} + \frac{x'^2}{2}\right)^2}\right]^{1/2}. \end{aligned} \tag{3.102}$$

The function $B(\vec{x}) = B(n_x, n_y)$ is defined in Eq. (3.39). By $\epsilon = \epsilon_{ik}/\bar{\epsilon}_{ik}$ we set the magnitude of the eigenstrains. We have introduced $\Phi = 2(1-\nu^2)/(E\epsilon^2(\bar{\epsilon}_{yy}^2 + \bar{\epsilon}_{zz}^2 + 2\nu\bar{\epsilon}_{yy}\bar{\epsilon}_{zz}))$ and the solvability parameter $\sigma = d/pR$ here. Together with the Peclet number p and the material properties, σ is the missing information to determine the desired quantities of the interface. As the normalization by p already indicates, the solvability parameter depends on the ratio of the elastic hysteresis and the Peclet number in the regime of small p.

In the following subsections, we only discuss shear and superpositions of shear and dilatational lattice strains. The dilatational lattice strains can be mapped to other problems - we recall that in section 3.2.4, the contribution of the elastic effects reduced to a constant shift of the undercooling. In the corresponding calculation, the consideration of the bicrystal geometry does not change this aspect of the dilatational strain. For the case of a 'weak' triple junction, we thus again obtain the absence of selection. In the case of a triple junction with finite slope at the tip, the problem can be mapped to melting along a grain boundary, a system we considered in [16] and also briefly discussed in subsection 2.4.2.

3.3.2 Shear Eigenstrain

Purport of this section is the definition and numerical solution for the shear lattice strain configuration. We recall that in the previous chapter, we defined the shear lattice strain configurations as $\epsilon_{yy}^s = \epsilon\cos 2\vartheta$, $\epsilon_{xx}^s = -\epsilon_{yy}^s$ and $\epsilon_{xy}^s = -\epsilon\sin 2\vartheta$. Here ϑ is the orientation angle between the old and the new symmetry axis, thus it takes the values $\vartheta = +2\pi/3$ in phase β and $\vartheta = -2\pi/3$ in phase β', see Fig. 3.2.

We obtain by solution of Eq. (3.102) for $\tan\phi = 0$ and $\tan\phi = 0.577$ the solvability plot shown in Fig. 3.14. The introduction of the 'weak' triple junction, $\tan\phi = 0$, obviously allows

us to resolve the shear lattice strain operating as selection mechanism here, in contrast to the single crystal geometry. The present selection also exhibits much larger values of the solvability parameter than the values known for selection by anisotropy of the surface tension. Since the velocity is determined by the effective driving force $\tilde{\Delta}$ and the solvability parameter σ as

$$\frac{vd}{D} = \frac{2}{\pi^2}\sigma\tilde{\Delta}^4, \tag{3.103}$$

the transitition velocities that could theoretically be observed in appropriate experiments are also much higher than in classical dendritic growth. It should be mentioned here that we assumed lattice strains of small magnitude, i.e. $\epsilon \ll 1$, such that the shift of the applied driving force Δ to the effective driving force $\tilde{\Delta}$ is not dominating the velocity.

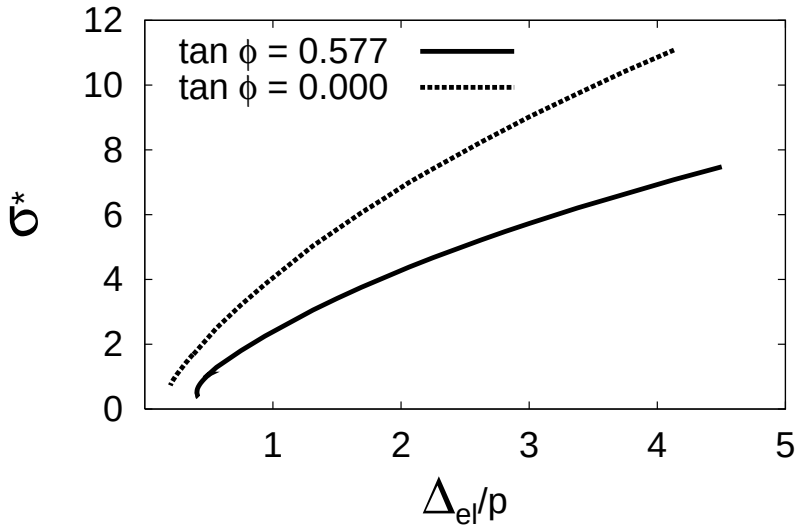

Figure 3.14: The solvability parameter $\sigma(\Delta_{el}/p)$ for a cuspid tip, $\tan\phi = 0.577$, and a smooth tip, $\tan\phi = 0$. The presence of the triple junction, which is of appreciable influence for $\tan\phi = 0.577$, leads to a second solution branch at the threshold value of $\Delta_{el/p} \approx 0.4$.

The second curve in Fig. 3.14, for $\tan\phi = 0.577$, shows the selection which occurs in a combination of two effects which already lead to a selection separately, as we know now. There, in the regime of small Δ_{el}/p at $\Delta_{el}/p \approx 0.4$, a second solution branch appears. Even if that branch corresponded to stable solutions, they would hardly be observed as they would be outgrown by the other branch with larger σ.

Comparison to Phase Field Simulations The Green's function method we apply cannot predict the dynamic stability of the found solutions, we refer to the results obtained by Michael Fleck in our group by means of phase-field calculations. As the concept of this method complicates the solution of the system with fixed opening angles, we restrict to a comparison with the solvability plot for a 'weak' triple junction. The resulting plot is shown in Fig. 3.16.

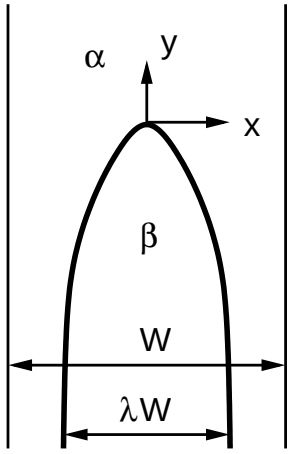

Figure 3.15: Sketch of the channel system geometry. The system with width W is infinitely long. The finger is wide as λW in its tail region, thus the ratio of finger width to channel width is given by λ. The (β) phase grows at expense of phase (α) in y-direction.

To assess the content of Fig. 3.16, one should take into account that the two solutions which are compared here are a free geometry calculation with the Green's function method and a channel geometry with the phase-field method. The agreement between channel and free growth was found for a small ratio of finger width to channel width λ, see fig 3.15. Then the geometrical confinement only has a weak influence on the system. Here the fraction λ is proportional to the driving force for the channel growth.

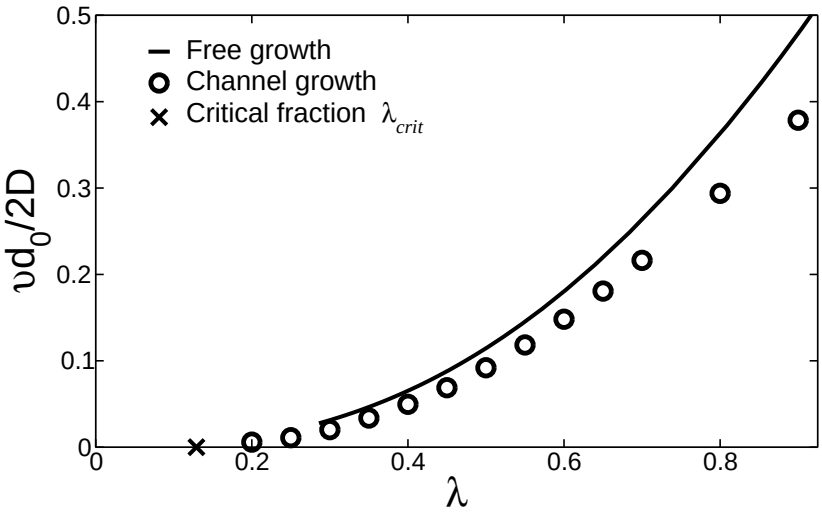

Figure 3.16: The dimensionless growth velocity versus relative finger width λ for free growth and channel growth. The elastic hysteresis is $\Delta_{el} = 0.3$

Consequently, when λ increases, the geometrical confinement of the channel becomes less negligible and the agreement is reduced - as we see in Fig. 3.16. However, the agreement we found

shows that the solutions found by means of the Green's function technique calculations correspond to dynamically stable patterns, as these are tracked by the phase-field method. For this section, we state that we revealed that a simple shear lattice strain can operate as selection mechanism - and analoguous to the previous section, we continue with lattice strains that can be represented as combination of dilatation and shear strains.

3.3.3 Mixing of Shear and Dilatational Eigenstrain

When we incorporate lattice strains which are represented as a superposition of shear and dilatation, this obviously extends the validity of the model massively. When we performed this extension for the single crystal geometry, this led to the observation of selection, where no selection appears for pure shear in the single crystal geometry.

We already found selection for pure shear in the bicrystal geometry and also considered how the selection changes when we introduce a triple junction. To focus on the effect on the superposition of the fundamental deformation modes, we restrict to 'weak' triple junctions. The influence of the triple junction would possibly impede the interpretation of the influence of dilatation on the present selection due to shear lattice strain. The mixed eigenstrain configurations we consider here are defined by $\epsilon^{\pm}_{ik} = (1-\eta)\epsilon^{s}_{ik} \pm \eta\epsilon^{d}_{ik}$. For ϵ^{+}_{ik}, we can write

$$\begin{pmatrix} \frac{\epsilon}{2}(1+\eta) & -\frac{\sqrt{3}\epsilon}{2}(1-\eta) & 0 \\ -\frac{\sqrt{3}\epsilon}{2}(1-\eta) & \frac{\epsilon}{2}(3\eta-1) & 0 \\ 0 & 0 & \eta \end{pmatrix} \tag{3.104}$$

and for ϵ^{-}_{ik} we get

$$\begin{pmatrix} \frac{\epsilon}{2}(1-3\eta) & -\frac{\sqrt{3}\epsilon}{2}(1-\eta) & 0 \\ -\frac{\sqrt{3}\epsilon}{2}(1-\eta) & -\frac{\epsilon}{2}(\eta+1) & 0 \\ 0 & 0 & -\eta \end{pmatrix}. \tag{3.105}$$

The mixing parameter η represents pure shear for $\eta = 0$. This definition of the lattice strains has an advantegeous property: we see that the two tensors in Eq. (3.104) and Eq. (3.105) can be obtained from each other by a rotation in the xy-plain about $\pi/2$, except for an absolute sign. When we compare the results for both configurations, we can thus conclude about the influence of the orientation between growth direction and lattice strains. We recall that it is this orientation which makes the difference between selection and no selection in the single crystal geometry, see section 3.2.6.

Results and Discussion We begin the discussion of our results with the type of superpositions represented by ϵ^+_{ik}. The plot σ vs Δ_{el}/p for two different η and the pure shear as reference mode is shown in Fig. 3.17. Here we see that an increasing fraction of dilatation raises the mag-

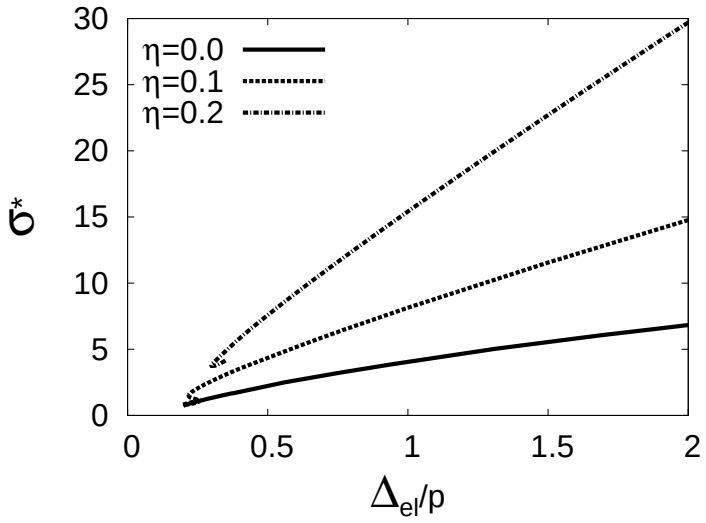

Figure 3.17: Stability parameter σ^* for two mixed configurations and the pure shear lattice strain. The influence of the triple junction was excluded, $\tan\phi = 0$. At the threshold around $\Delta_{el}/p \sim 0.4$, secondary branches appear.

nitude of the solvability parameters obtained at fixed Δ_{el}/p. Specifically, for $\eta = 0.2$ the values which σ takes are up to four times higher than for the reference pure shear. Also, both solvability-plots with finite η show a threshold behaviour between $\Delta_{el}/p = 0.2$ and $\Delta_{el}/p = 0.4$. Admittedly, the secondary branch is merely indicated by our calculations, but the corresponding parts of the plots have a high point density, and we extensively checked the regime of Δ_{el}/p smaller than the assumed threshold.

In comparison, for the solvability plot for the eigenstrain which we denote by ϵ^-_{ik}, we yield the opposite behaviour - while we also find a selection here. In Fig. 3.18, the reference shear curve shows the largest values of the solvability parameter. The Increase of the mixing parameter η here leads to a substantial decrease of σ, at $\eta = 0.5$ up to a prefactor of 10 compared to shear. We recall that the change from ϵ^+ to ϵ^- corresponds, up to a total sign, to a rotation of the strains relative to the growth direction by $\pi/2$. Obviously, the orientation between growth direction and lattice strains is crucial for the transition, as we already found for transitions which develop into single crystal geometries. For the representation of the plot σ vs η for both ϵ^+_{ik} and ϵ^-_{ik}, shown in Fig. 3.19, we choose $\Delta_{el}/p = 1$. The contrariness of the solutions for both types of superposition not only consists of the opposite direction of change from the reference shear solvability parameter. Obviously, also the regime of η where the selection occurs, is different. While the solutions for ϵ^-_{ik} can be obtained in the entire region, up to $\eta = 1$ nearly, the selection ceases to exist at $\eta \approx 0.25$ for ϵ^+_{ik}. The reason for this specific value is not clear, but with increasing η we find a rapidly growing bulge of the interface into the growth direction at the tip, see Fig. 3.20. The idea of a transition to a doublon growth mode is apparent, but the interface does not indicate the presence of the characteristic channel at the tip. Interpretation of the ending selection for ϵ^+_{ik} at $\eta \approx 0.25$

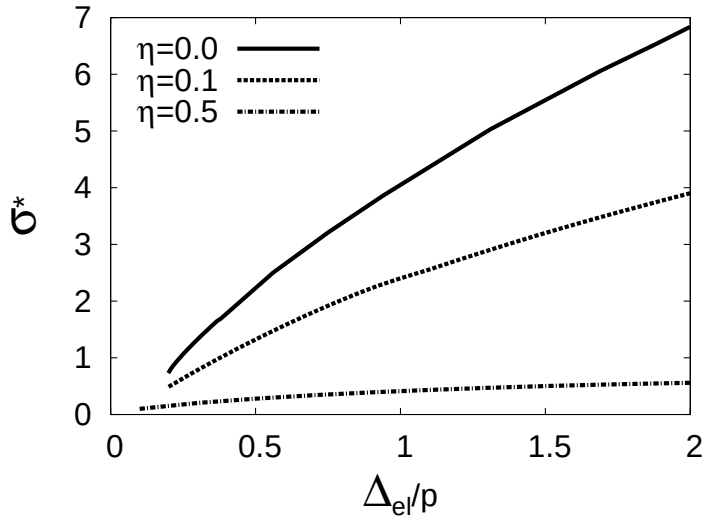

Figure 3.18: The solvability plot for the superposition of type ϵ_{ik}^{-}. We see that increased fractions of dilatation lead to lower solvability parameters σ. This type of superposition lacks the secondary solution branches which appear in Fig. 3.17.

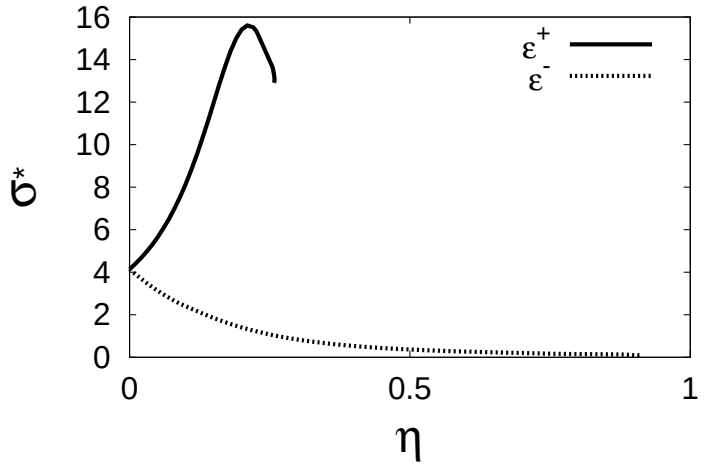

Figure 3.19: Dependence of the solvability parameter at fixed $\Delta_{el}/p = 1$ on the mixing parameter η. We see that the regime of solution for the superposition of type ϵ_{ik}^{+} is limited to $\eta \sim 0.25$, though there we obtain larger velocities.

thus remains unclear. For the location of the maximum σ for ϵ_{ik}^{+}, we find an analogue coincidence as for the single crystal. For ϵ_{ik}^{+} , Δ_{el} is explicitly defined as

$$\Delta_{el} = \frac{T_{eq} c_p \epsilon^2 E}{2(1-\nu^2)L^2}\left[\frac{1}{4}(3\eta-1)^2 + \eta^2 + \nu\eta(3\eta-1)\right]. \tag{3.106}$$

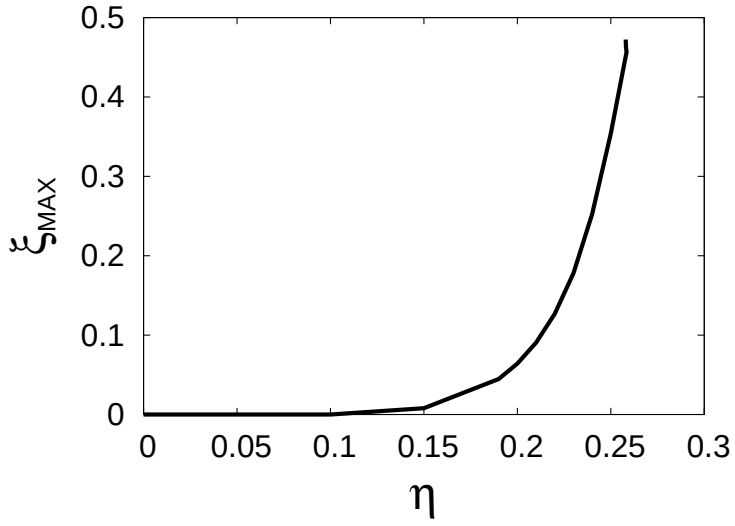

Figure 3.20: ξ_{MAX} denotes the y-coordinate of the tip of the bulge at the tip of the interface. This development of the interface corresponds to the plot for ϵ_{ik}^{+} at $\Delta_{el}/p = 1$ in Fig. 3.19.

Numerically, we find the maximum of σ for ϵ_{ik}^{+} at $\eta \approx 0.24$. When we estimate the point of least elastic hysteresis, we obtain as minimum for Δ_{el} the value $\eta^{*} = 11/51$, which is quite close to the maximum. However, as in the single crystal geometry, this is a striking coincidence, but independent of this intuitive argument, we cannot judge if this effect has dominant influence on the position of the maximum.

Comparison to Phase Field Results Apart from the nontrivial question of appropriate detailed interpretation of the found solvability plots, a point of fundamental importance is the dynamical stability of the solutions. We can compare to the results obtained by Michael Fleck in our group by means of phase-field simulations for channel growth. We compare the superposition of type ϵ_{ik}^{+} at $\eta = 0.1$ and type ϵ_{ik}^{-} at $\eta = 0.5$. As already mentioned in section 3.2.6, the comparison in these two geometries can be expected to show a decreasing agreement of the results for increasing relative finger width λ. The agreement for ϵ_{ik}^{+} which we show in Fig. 3.21 is excellent and covers a wide range of λ. The secondary branch, which we see in Fig. 3.21 in the regime $0.6 \leq \lambda \leq 0.8$, could not be resolved with the phase field method, but the primary branch is obviously dynamically stable. In the regime of the threshold, the phase-field simulations find a dynamically stable solution which bulges into the reference phase at the tip, named twinned phase here. This suggests dynamical instability of the secondary branch we found, which also exhibited the growth of a bulge into the reference phase, see Fig. 3.20. For the configurations ϵ_{ik}^{-}, where we choose $\eta = 0.5$, we also find a good agreement. Though restricted to a smaller range of driving forces λ, the matching of phase-field and Green's function method results means that for this configuration, the obtained solutions are dynamically stable.

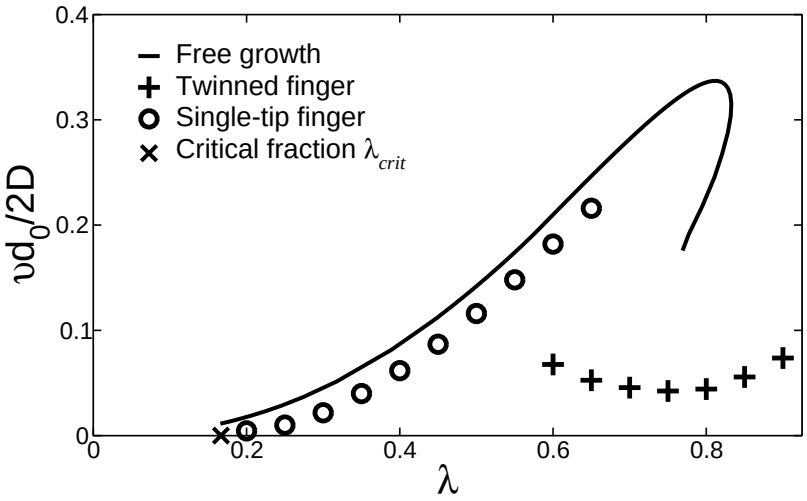

Figure 3.21: The growth velocity obtained by means of Green's function method in the free geometry and the phase-field method in the channel geometry. The elastic hysteresis is $\Delta_{el} = 0.1$, and the superposition ϵ^{+}_{ik} is set by $\eta = 0.1$. The regime which shows good agreement ranges from $\lambda = 0.2$ to $\lambda = 0.65$, for larger relative finger widths the phase field method tracks branches probably pertaining to dynamical solutions. The critical fraction λ_c corresponds to the minimal λ which leads to positive growth velocities in the phase field model.

3.3.4 Looking for Purely Elastic Selection in the Zero-Velocity Limit

The last case we consider within this section is the so-called zero-velocity limit. This limit labels the scenario of very slow diffusion, so that the interface propagates slowly. Then, the diffusion is sufficiently low to have the elastic effects dominate the transition. We consider the pure shear transition which we label ϵ^{s}_{ik}. It exhibits selection in the regime of small Peclet numbers $p \ll 1$, as we discussed in section 3.3.2. In the case of very small Δ_{el}/p, one shall exploit the possibilites of analytic methods, e.g. apply the complex matching method which yielded the solution of the classical dendritic problem, but for the limit of $p/\Delta_{el} \ll 1$, analytic approaches in the aforementioned spirit are not at hand, suggesting specific numerical consideration here.

This is an essential question of the elastic-diffusional problem we consider - how does the system behave in the limit of zero velocity. While one can easily understand that in the limit of zero lattice strains, the system would exhibit selection in case of a triple junction, $\tan\phi \neq 0$, it is unclear what happens at zero velocity. Formally, we can reach the regime of a possibly negligible release of latent heat at the interface when $\upsilon \to 0$. We introduce a representation of the problem which suits this approach, namely

$$
\begin{aligned}
- \quad & \frac{d}{\Delta_{el} R}\kappa + \Phi\left[\sigma^{\epsilon}_{ik} u^{(\alpha)}_{ik} - \frac{E\epsilon^2 B(x,x')}{2(1-\nu^2)}\right] \\
= \quad & -\frac{1}{\pi}\frac{p}{\Delta_{el}} \int_{-\infty}^{\infty} dx' \log\left[\frac{(x-x')^2 + (y(x)-y(x'))^2}{(x-x')^2 + \left(-\frac{x^2}{2} + \frac{x'^2}{2}\right)^2}\right]^{1/2},
\end{aligned}
\tag{3.107}
$$

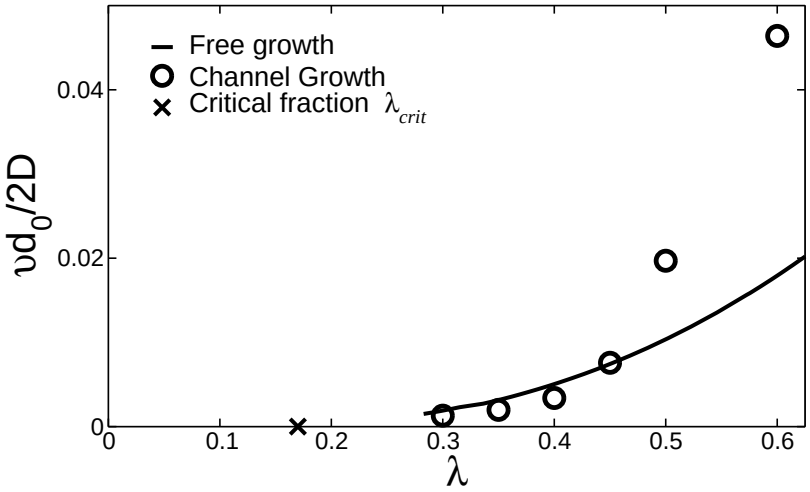

Figure 3.22: The growth velocity obtained by means of Green's function method in the free geometry and the phase-field method in the channel geometry. The elastic hysteresis is $\Delta_{el} = 0.2$, and the superposition ϵ^{-}_{ik} is set by $\eta = 0.5$.

where we define

$$\Phi = \frac{2(1-\nu^2)}{E\epsilon^2(\bar{\epsilon}^2_{yy} + \bar{\epsilon}^2_{zz} + 2\nu\bar{\epsilon}_{yy}\bar{\epsilon}_{zz})}$$

The corresponding elastic solvability parameter σ_{el} is defined as

$$\frac{d}{\Delta_{el}R} = \sigma_{el} = \frac{1}{R}\frac{2\gamma(1-\nu^2)}{E\epsilon^2(\bar{\epsilon}^2_{yy} + \bar{\epsilon}^2_{zz} + 2\nu\bar{\epsilon}_{yy}\bar{\epsilon}_{zz})}, \tag{3.108}$$

and we recognize that in fact σ_{el} is independent of any thermal quantities. Though this appears to be a purely formal aspect, this restatement of the entire problem as given in Eq. (3.107) clearly exhibits the possible elastic selection in a zero-velocity limit, when $p \to 0$ for finite radii R. Before we discuss the outcome of our calculations, we shall briefly discuss the outcome of the previous considerations about elastic selection in pattern formation.

Elasticity-Induced Selection in Growth of a Lenticular Melt Inclusion

This small paragraph is a brief excursion to elastic pattern selection as considered in [19]. Though the detailed understanding of the discussed growth behaviour is beyond the scope of this thesis, we roughly describe the problem and the outcome. The motivation for this small interruption is the dendritic growth behaviour derived in [19], found for elastic selection.

Referring to [19], we consider the growth of a melt inclusion, which has a very oblate lenticular shape, $h/R \ll 1$ where h is the height of the lentil, and R is the radius of the circle which is the cross section of the inclusion in the xy-plane. The governing equations of growth describe the consumption of the latent heat at the interface which has to be transported there by thermal

diffusion:

$$D\nabla^2 w = \frac{\partial w}{\partial t} \tag{3.109}$$

$$\upsilon_n = -D\vec{n}\nabla w|_{int} \tag{3.110}$$

$$w|_{int} = \Delta\left(1 - \frac{P}{P_c}\right). \tag{3.111}$$

The temperature is defined as $w = c_P(T_\infty - T)/L$, the overheating as $\Delta = c_P(T_\infty - T_M)/L$, with T_M the melting temperature and L the latent heat, c_P the specific heat, and D is the diffusion constant, υ_n the normal velocity of the interface. Eq. (3.109) is the diffusion equation which is supported by the equation for heat conservation, Eq. (3.110), and the equation of local equilibrium, Eq. (3.111) where elastic and capillarity corrections are excluded. The temperature inside the inclusion is assumed to be constant and equal to its interfacial value, (3.111), and the local equilibrium requires the pressure inside the nucleus to satisfy the Griffith formula,

$$P^2 = \frac{\pi E\alpha}{2(1-\nu^2)R}, \tag{3.112}$$

here α is the surface energy. Again, E, ν are the elastic modulus and the Poisson ratio. In the regime of radii smaller than the diffusion length, $R < (Dt)^{1/2}$, the system is approximated by solving the Laplace equation instead of the diffusion equation. Within this approach, the combination of the Griffith formula (3.112) and the mass conservation,

$$\left(\frac{\nu_l}{\nu_s} - 1\right)\frac{\pi R^2 h}{\nu_s} = \int u_n ds, \tag{3.113}$$

set the value of the characteristic length scale ρ,

$$\rho = \frac{128\alpha(1-\nu^2)v_s^2}{9\pi E(v_l - v_s)^2}. \tag{3.114}$$

Here, by $\nu_{l,s}$ we define the atomic volume of the liquid and the solid phase, by u_n the normal component of the displacement vector of the interface. By ρ, the lentil height h is selected,

$$h = \sqrt{\rho R}. \tag{3.115}$$

The crucial point is the absence of any thermal quantities in ρ. This is the first hint indicating that search for an elastic selection in our system is suggested. In addition, when one drops the restriction to $R < (Dt)^{1/2}$, the system exhibits a steady-state Ivantsov regime with a velocity scaling as

$$\upsilon \sim \frac{D}{\rho}\Delta^2, \tag{3.116}$$

which suggests the appellation as elastic dendrite. Summarizing, this short view on the growth of a lenticular melt inclusion shows that diffusion-limited growth can exhibit elastic selection in conjunction with parabolic asymptotics in the steady-state regime of the transition.

Results in the Zero Velocity Limit

We come back to the calculations we performed in the limit $p/\Delta_{el} \ll 1$, i.e. $\upsilon \to 0$. The resulting calculations for pure shear can cover the regime up to $p/\Delta_{el} = 0.05$, but even at this already small value, an extrapolation to $p/\Delta_{el} \to 0$ remains inconclusive. As the plot in Fig. 3.23 shows, we can at least assume that the hidden behaviour of the selection does not obey a linear law. Exemplarily, we discuss the result of a - potentially present - finite σ_{el} and the result for the case $\sigma_{el} \sim (p/\Delta_{el})^{1/2}$. A finite value of σ_{el} at zero p/Δ_{el} would lead to an elastic selection as

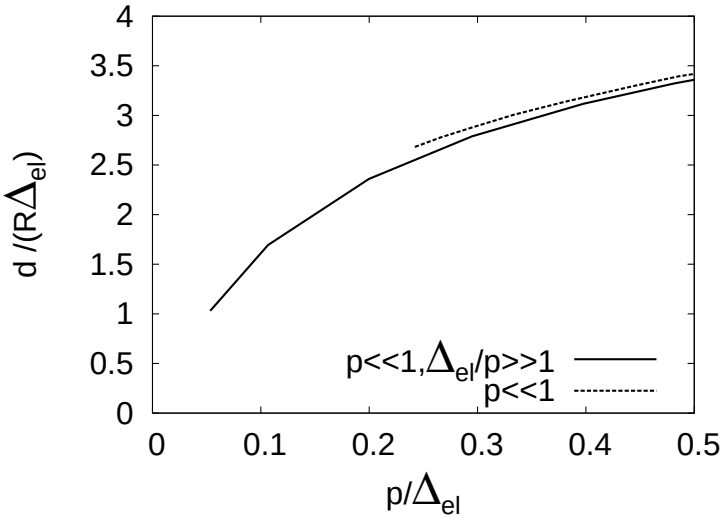

Figure 3.23: The close up of the regime up to $p/\Delta_{el} = 0.5$. The solid line was obtained in the asymptotic regime and matches the results obtained for Δ_{el}/p vs. σ before, represented by the dashed line. The results for the asymptotic regime $\Delta_{el}/p \to \infty$ remain inconclusive concerning the presence of a selection for zero velocity.

$$R = \frac{d}{\Delta_{el}\sigma_{el}} \sim const \tag{3.117}$$

$$\upsilon = \frac{2\Delta_{el}\sigma_{el}}{\pi}\frac{D}{d}\tilde{\Delta}^2 \sim \tilde{\Delta}^2. \tag{3.118}$$

Here, the growth in this regime close to zero velocity would occur faster than the growth in the regime of small p/Δ_{el}, where the velocity scales as $\upsilon \sim \sigma\tilde{\Delta}^4$, and the interface would exhibit a finite radius R. The case of $\sigma_{el} \sim (p/\Delta_{el})^{1/2}$ would also result in a faster growth mode,

$$R \sim \frac{1}{\tilde{\Delta}} \tag{3.119}$$

$$\upsilon \sim \tilde{\Delta}^3. \tag{3.120}$$

Inspite of the inconclusive numerical results for the zero velocity limit concerning a finite σ_{el}, the results show that the exhibited growth is faster than the classical dendritic growth.

3.3.5 Conclusion

This section is dedicated to the diffusion limited growth of a bicrystal in a solid, where we take lattice strains into account. The presence of a triple junction in the bicrystal geometry requires to distinguish between a 'weak' triple junction, i.e. a smooth tip, and a triple junction with finite slope at the tip. These two cases allow to consider if selection with isotropic surface tension exists due to elastic effects, and separately how elastic effects and selection due to the triple junction interact. The system can be mapped to classical dendritic growth with isotropic surface tension in case of pure dilatational lattice strains and 'weak' triple junction, analogue to our proceeding in section 3.2.4. The configuration with dilatational lattice strains and a triple junction can be mapped to the problem of selection due to a triple junction we considered in [16]. Both dilatational configurations thus can be solved by relating them to other systems.

In the case of shear lattice strains, we find a selection due to the elastic effects for a 'weak' triple junction. The found solutions exhibit to be dynamically stable, as comparison with phase-field simulations show. The magnitude of the solvability parameter obtained here is much higher than in classical dendritic growth, and thus also the transition velocities can reach higher values. When we consider shear lattice strains with a triple junction and finite slope, we find a threshold behaviour at small Δ_{el}/p. The secondary branch, which corresponds to lower values of the solvability parameter, is difficult to obtain numerically, but if it were a stable solution, it would be outgrown by the primary branch, which corresponds to faster growth velocites.

The superposition of shear and dilatation is discussed only for 'weak' triple junctions, since the pure shear already triggers a selection. We define two superposition types, ϵ^{+}_{ik} and ϵ^{-}_{ik}, which can be obtained from each other by a rotation of the strain orientation to the growth direction by $\pi/2$. In both cases, we find that selection occurs. The deviation to the selection that we know from shear is contrary for the configurations. The solutions for ϵ^{+}_{ik} exist only up to superpositions with a dilatational fraction of ca. 25%, and the solvability parameter reaches values which are larger up to a factor of 4 for fixed Δ_{el}/p. For ϵ^{-}_{ik}, we obtain solutions in the entire range from zero up close to one. The solvability parameter is shifted to smaller values - obviously, the orientation between growth direction and strain is crucial for the velocity selection.

Finally, we investigate the behaviour of the pure shear bicrystal in the limit of negligible release of latent heat, what we call zero-velocity limit. Our results for such a purely elasticity-induced selection remain inconclusive, though they qualitatively suggest that the range of possible growth behaviours correspond to higher transition velocities than classical dendritic growth exhibits.

4 Phase Transitions Limited by Chemical Diffusion

Pattern formation in metallurgical processing results from various transport processes. Though there exist systems where the investigation of chemical and thermal diffusion on the same timescale is required, the approximation of separate timescales for the two types of diffusion is in fact legitimate in many systems found in industrial application. Consequently, when we investigate the pattern formation associated with the diffusion of chemical components in such systems, our models will only take into account the limiting transport process - which is the chemical diffusion in many metallurgical problems.

This chapter comprises the investigation on two distinct and yet unresolved problems of pattern formation limited by chemical diffusion. We begin with a brief recapitulation of the eutectic-type transformation and basic results for this process of broad application, see **section** 4.1. We introduce the isolated eutectoid dendrite. This fascinating structure belongs to the solid-solid transformations of eutectic type.

The second system which we investigate in **section** 4.2 is the monotectic dendrite. The geometry which we introduce allows to study an asymmetric dendritic pattern growing along a liquid-liquid interface. This challenging case concerns the regime of the monotectic transitions where the liquid phase occurs decomposed.

4.1 Eutectic-Type Transitions

This section on chemical-diffusional phase transitions focuses on eutectic and eutectoid reactions. We introduce the eutectic transition in 4.1.1. The resemblance to the eutectoid transition will facilitate our understanding of eutectoid growth - the system we investigate in 4.1.2.

Both eutectic and eutectoid growth are transition modes for a binary mixture. They operate near the eutectic and eutectoid point in a phase diagram, where the cooled material splits into two different solid phases. These two phases exhibit opposite concentrations: one phase consists of a high concentration of α atoms, with a low concentration of β atoms, the other phase vice versa. Here the notation α, β is arbitrarily chosen. The occurence of such special points in the phase diagram is a material property. One of the most important materials which can undergo both types of transition is the iron-carbon mixture. Consequently, we choose to discuss this material exemplarily. The corresponding phase diagram in Fig. 4.1 is quite complex, and we will only briefly discuss the various transitions and products.

The presented $Fe - C$ phase diagram in Fig. 4.1 is cut off at a carbon concentration of $\approx 6.5\%$. This value has pragmatical reasons. In this iron-carbon system, the carbon can occur as graphite or as Fe_3C, cementite, and the reaction we are interested in involve cementite, not graphite. Due to the molecular masses and the atom ratio in Fe_3C of 3:1, 100% fraction of cementite correspond to $\approx 6.5\%$ of carbon. Consequently, we cover the regime of relevant concentrations.

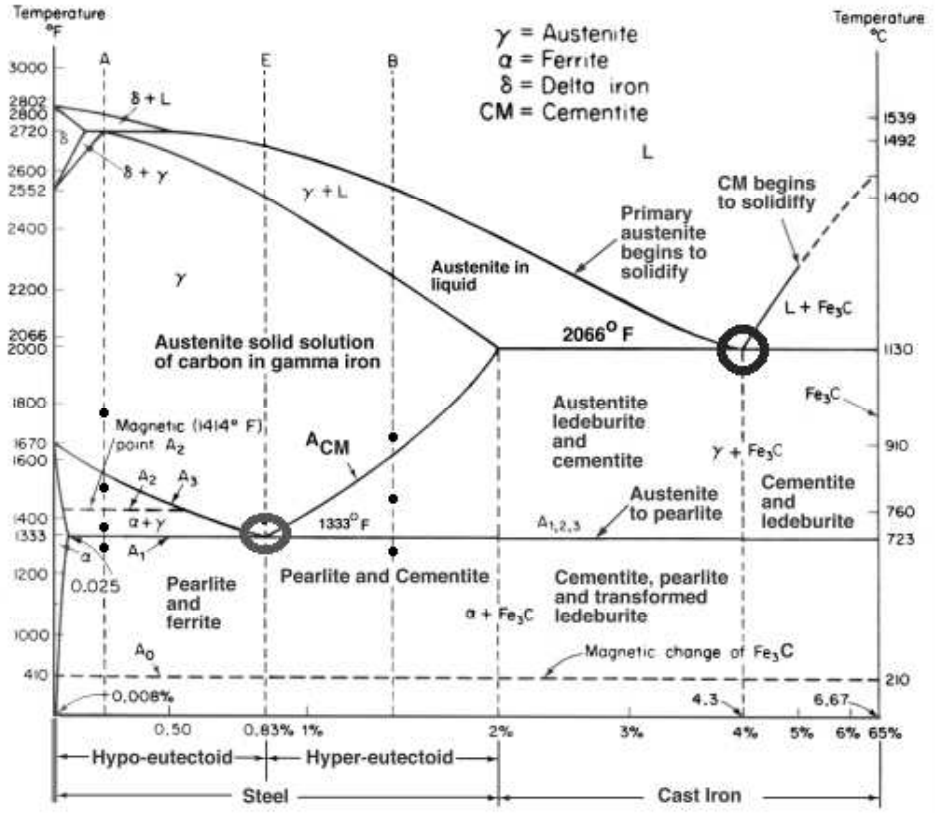

Figure 4.1: An excerpt of the Fe-C reaction phase diagram [68]. The right upper circle marks the eutectic point at 1147°C and concentration of $4,3\%$ carbon. Here the melt solidifies into γ-mixture crystals called austenite, and ledeburite. The lower left ellipse marks the eutectoid concentration E and temperature, $723°C$. Here the austenite decomposes into α-mixture crystals called ferrite and cementite.

Cementite has an orthorhombic crystal structure, it is hard and brittle. It either forms from austenite during cooling or from martensite during heating. Though only metastable, it withstands most of the heat treatments for steel and remains as distinct phase.

Ferrite is almost pure iron and shows a bcc-structure. It is the component of steel and cast iron which dominates its magnetic properties. In the range of up to $1184K$ it exists as α-iron, in the range of $1665K$ and $1809K$ it exists as δ-iron, they differ in the solulibility of carbon.

Austenite (γ-iron) is a metallic non-magnetic solid solution, with fcc crystal structure, it exists above the critical eutectoid temperature of $1000K$.

Martensite is formed by displacive transformation, by quenching of austenite which traps carbon atoms such that they cannot diffuse out of the crystal. Martensite has a body-centered-tetragonal structure.

Pearlite has a lamellar structure composed of alternating layers of α-ferrite ($88wt\%$) and cementite (12%), it forms by a eutectoid reaction as austenite is slowly cooled below $1000K$.

Ledeburite is the eutectic that results when the molten steel solidifies, a phase mixture of austenite and cementite which melts at $1420K$.

The aforementioned structures give a complete list of the phases we will encounter in the subsequent discussion, where we will occasionally refer to them though our considerations are not limited to the iron-carbon mixture. We start with the eutectic transition, which is located at the circle in the upper right in the $Fe - C$ phase diagram, Fig. 4.1.

4.1.1 Eutectic Phase Transition

Although we introduced the iron-carbon mixture as exemplarily for both eutectic and eutectoid growth, we need to define certain simplifying assumptions about the system. We commence the explication with the phase diagram in Fig. 4.2.

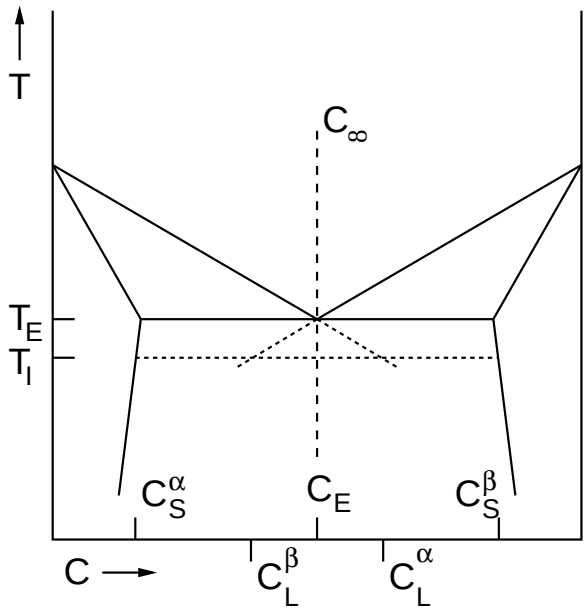

Figure 4.2: The schematic symmetrical eutectic phase diagram. The average temperature at the interface is T_I, thus the liquid has the metastable concentrations C_L^β and C_L^α. The creating solid phases α and β have the concentrations C_S^α and C_S^β. The concentration infinitely far away from the interface in the liquid is given as $C_\infty = C_E$, the eutectic concentration.

When we compare the region at the circle in the right top of Fig. 4.1 and the phase diagram in Fig. 4.2, we see the simplifications. Obviously, we linearized and symmetrized the phase diagram in the region around the eutectic point, where the $Fe - C$ melt solidifies to a mixture of austenite, cementite and ledeburite or cementite and ledeburite, respectively.

Among the different types of eutectic transitions, we will focus on one type of so-called normal eutectic solidification. Normal means here that the creating structure will be rod-like in a matrix, e.g. for Al_6Fe [69], or lamellar, as it occurs in the iron-carbon mixture,see a schematic illustration in Fig. 4.3. We consider the latter, and depict the basic features of lamellar eutectic growth.

The governing process of the transition which can be illustrated with Fig. 4.3 is the diffusion of each type of atom along the lamellar interface. We will denote the phase with a high concentration of α-atoms phase α, and the phase with a high concentration of β-atoms phase β. As phase α

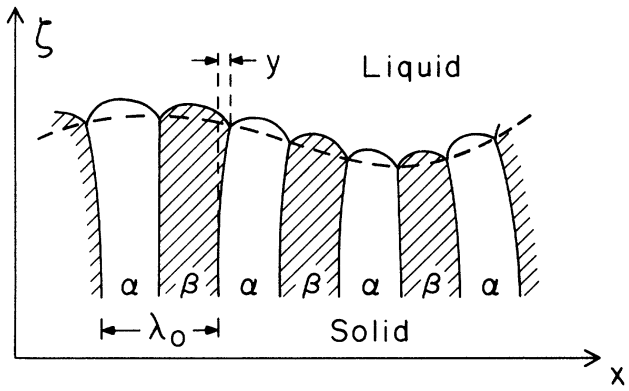

Figure 4.3: The lamellar eutectic front [58]. By λ_0 we denote the spatial periodicity of the lamellar structure in the asymptotic region. Here we also define the vertical deformation of the growth front by ξ and the lateral deformation y. As we will neglect the lateral deformation in our considerations, we denote λ instead of λ_0.

solidifies, it rejects β-atoms, and vice versa for phase β. The atoms only need to diffuse into the neighbouring lamella, which corresponds to the distance $\approx \lambda/2$. If we assume symmetry of the onsetting lamellae, $y = 0$ and $\xi = 0$, then the distance equals $\lambda/2$.

To find the crucial lengthscale of the system, the spatial periodicity λ, we give the argumentation presented originally by Jackson and Hunt [39]. One basic assumption is that the operating transition point of the system with a spacing λ will be fixed by the minimal undercooling. The undercooling $\Delta T_I = T_E - T_I$ can be expressed by the concentration difference $\Delta C = C_L^\alpha - C_L^\beta$, and the slopes of the liquidus lines, $\|dT/dC_L\|$:

$$\Delta T_I = \frac{\Delta C}{2} \left\| \frac{dT}{dC_L} \right\|. \tag{4.1}$$

The relation to the periodicty λ is given by the matter conservation at the interface,

$$\upsilon C_E (1 - k) = D \frac{\Delta C}{\lambda/2}. \tag{4.2}$$

Here we denote the eutectic concentration by C_E, the growth velocity by υ, D is the chemical diffusion constant and the segregation coefficient is $k = \|dT/dC_L\|/\|dT/dC_S\|$. Eq. (4.2) states that the diffusion flux over distance $\lambda/2$ to the next lamella through the liquid must equal the material flux which comes from the propagation of the interface with velocity υ. For undercooling

ΔT_I we thus write

$$\Delta T_I = \frac{1}{2}\left\|\frac{dT}{dC_L}\right\| C_E(1-k)\frac{\lambda}{l_D}, \tag{4.3}$$

where we introduced the diffusion length $l_D = 2D/\upsilon$. The second contribution to the undercooling comes from the Gibbs-Thomson relation, obviously the curvature behaves as $\kappa \sim \lambda^{-1}$. To be more precise, the additional undercooling ΔT_κ reads as $\Delta T_\kappa = T_E d\kappa$, where we introduced the capillarity length d which is proportional to the surface tension. The resulting undercooling $\Delta T = \Delta T_I + \Delta T_\kappa$ is obtained as

$$\Delta T = T_E\left(a_I\frac{\lambda}{l_D} + a_\kappa\frac{d}{\lambda}\right), \tag{4.4}$$

where the a_i are dimensionless coefficients, $a_I = 1/2(\|dT/dC_L\|)(T_E/C_E)(1-k))$ and $a_k = \kappa\lambda$. In principle, one has to take into account the kinetic undercooling, but usually this contribution can be neglected - in metal eutectics, the typical order of magnitude of the growth velocities is $\mu m\ s^{-1}$.

For the operation of the transition at minimal undercooling for a given λ, thus we yield:

$$\lambda = \sqrt{\frac{a_\kappa}{a_I}}\sqrt{l_D d}. \tag{4.5}$$

Real values for λ are typically in the order of μm, see Jackson and Hunt [39] for experimental comparisons.

The progress about lamellar eutectic growth has its origin as well in the aforementioned considerations as in the closed integral equation formulation of the problem, see [40]. Especially the most recent results were obtained by application of this technique, and we will apply it to the problem of eutectoid transformations in the next section.

4.1.2 Eutectoid Phase Transition

In this section about eutectoid transitions, we will explain the development from basic considerations to a closed formulation for the problem as boundary integral equation. As for eutectic growth, we locate the transition in the iron-carbon phase diagram. The regime in the grey rectangle in Fig. 4.4 contains the range of carbon concentrations which can lead to the eutectoid reaction.

The eutectoid transition is similar to the eutectic transition, instead of *melt* $\mapsto$ *solid* α + *solid* β, we observe the process *solid* $\gamma \mapsto$ *solid* α + *solid* β. As in eutectic growth, the onsetting phases in eutectoid growth exhibit opposite concentrations and can form a lamellar structure. The corresponding reaction in the iron-carbon phase diagram in Fig. 4.4 is *Austenite* $\mapsto$ *Pearlite* + *Cementite*/*Pearlite* + *Ferrite*. The name Pearlite reflects the fact that it shows the same optical effect as mother-of-pearl due to its lamellar structure.

However, we will not restrict our considerations to this specific type of $Fe - C$ reaction, but develop a model which enables us to investigate the most determining aspects of the eutectoid system, namely, the selection of the growth velocity of the appearing pattern in our model.

The nature of this kind of selection problems is known to be quite complex, we just recall of the

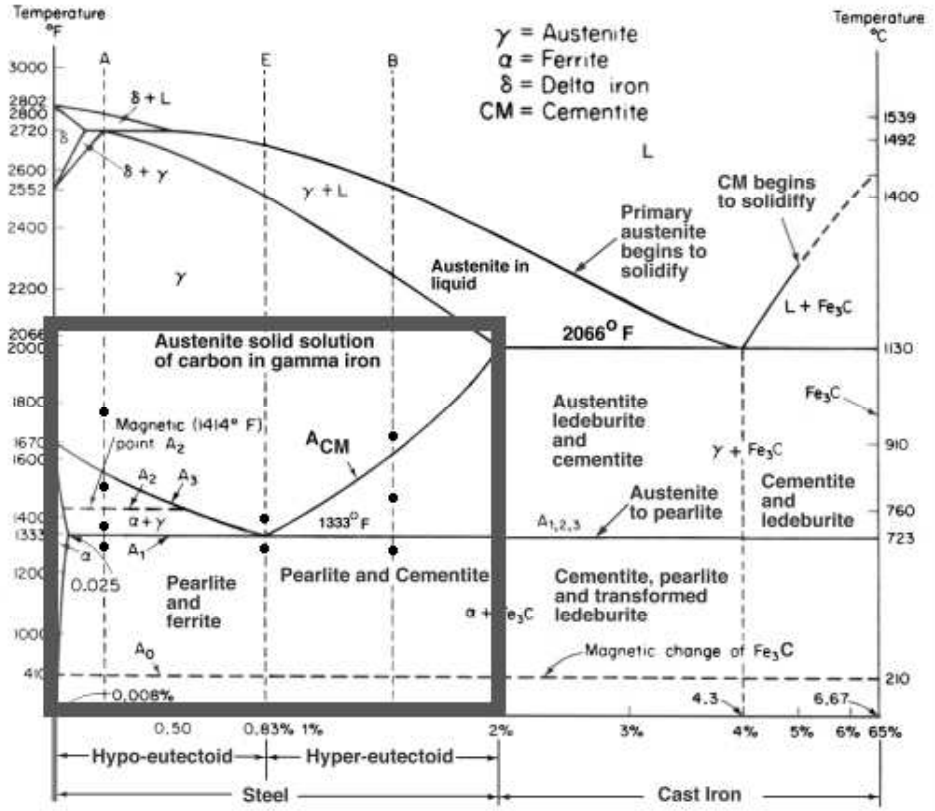

Figure 4.4: An excerpt of the Fe-C reaction phase diagram [68]. The regime of concentrations and temperatures which can lead to eutectoid transitions is located in the grey rectangle. The eutectoid concentration E and temperature, $723°C$, assign the point where the reaction pearlite+ferrite/pearlite+cementite $\mapsto$ austenite, or vice versa, occurs. The terminology of the different phases is explained in section 4.1.

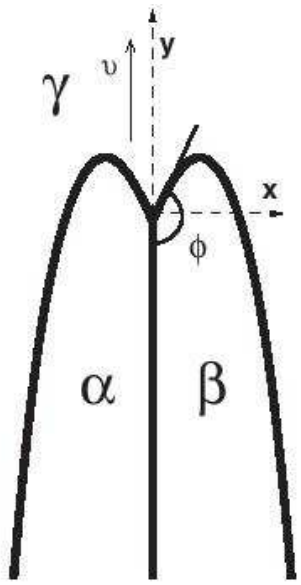

Figure 4.5: The assumed schematic interface in the eutectoid reaction. The isolated dendrite grows with constant velocity υ along the y-axis. The opening angle ϕ is fixed by Young's law; The assumption of identical surface tensions γ_α and γ_β on the interfaces yields $\sin(\phi - \pi/2) = \gamma_{\alpha\beta}/2\gamma_\alpha$, where $\gamma_{\alpha\beta}$ is the surface tension of the $\alpha - \beta$-interface.

difficulties which arose during the studies about dendritic crystal growth. It is now known that in classical dendritic growth [18, 13] the anisotropy of the surface tension is required for a selection. As the symmetry assumptions we will later introduce can provide dendritic asymptotics, it is promising to search for the connection to classical dendritic growth. We will see that the selection in the presence of a triple junction leads to a fundamentally different selection than in classical dendritic growth.

Model Development

The assumptions which underlie the successive considerations concern three basic aspects of the system. The geometry states the case of an 'isolated dendrite', i.e. the periodicity of the creating lamellar structure is much larger than the tip radius of curvature - the 'dendrite' is legitimate as we point out later when we consider the asymptotic behaviour of the chemical diffusion. The corresponding shape is given in Fig. 4.5.

Apart from that, we assume that in all three phases, the chemical diffusion constants D are the same. Additionally, the dependence of the free energy satisfies $(\partial^2 f/\partial c_i^2)_{eq} = (\partial^2 f/\partial c_j^2)_{eq}$, where *eq* indicates that $(\partial^2 f/\partial c_i^2)_{eq}$ is taken at the equilibrium concentrations of each phase. Consequently, one may consider all three phases as one area of definition where the interfaces remain as source and sink terms which we integrate to obtain a boundary integral formulation of the solution. This 'symmetric model' was originally proposed by to Langer and Turski, [53, 51], who intended to simplify the consideration of solid-solid diffusional transitions. Later it has been transferred to various other systems.

Finally, we introduce a simplified phase diagram which exhibits a symmetric structure, see Fig. 4.6.

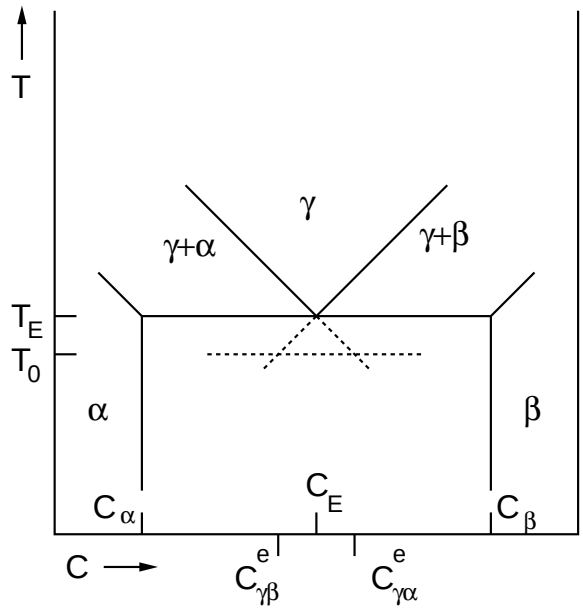

Figure 4.6: The schematic phase diagram of the eutectoid reaction. T_0 is the temperature of the system, T_E is the eutectoid temperature. C_α , C_β , and C_E are the equilibrium concentrations at the eutectoid temperature. For this diagram the eutectoid concentration $C_E = (C_\alpha + C_\beta)/2$ and the lines of the equilibrium of the γ and α phases are parallel, the same for the lines of the equilibrium of the γ and β phases. The equilibrium concentrations at the α/β interface, $C_{\alpha,\beta}$ do not depend on the temperature.

Obviously, this phase diagram and setting the initial concentration far away from the interface in the γ-phase as $c(\infty) = c_E$ lead to the symmetry of the eutectoid dendrite shown in Fig. 4.5. In the subsequent discussion of the system, we shall see that these symmetry assumptions drastically simplify the theoretical access to the problem.

The free boundary problem we consider is stated for the concentration c, which we define dimensionless as

$$u = (c_E - c)/(c_\beta - c_E). \tag{4.6}$$

Here c_E is the eutectoid concentration, c_β is the equilibrium concentration in the β-phase.
As illustrated in Fig. 4.5, the origin of the coordinate system is located at the tip of the interface which propagates at velocity υ. The diffusion equation thus can be written as

$$D\nabla^2 u + \upsilon \frac{\partial u}{\partial y} = 0, \tag{4.7}$$

here D is the chemical diffusion constant. The free boundary or Stefan condition of the diffusion

equation is the matter conservation on the moving interface:

$$-D\vec{n}(\vec{\nabla}c_\gamma - \vec{\nabla}c_\beta) = \upsilon_n \Delta c \tag{4.8}$$

reflects that the concentration jump $\Delta c = c_\beta - c_E$ which is is consumed on the $\gamma\beta$ - interface and set free on the $\gamma\alpha$ - interface with velocity υ_n, equals the difference of fluxes in both phases across the boundary.

On the interfaces, we assume local equilibria,

$$\begin{aligned} u &= \Delta^\alpha - d^\alpha \kappa, \\ u &= \Delta^\beta - d^\beta \kappa. \end{aligned} \tag{4.9}$$

At the $\gamma\alpha$-interface the mixture is undersaturated, $\Delta^\alpha = (c_E - c^e_{\gamma\alpha})/(c_\beta - c_E) < 0$. Due to the symmetry of the phase diagram and $c_\infty = c_E$, on the $\gamma\beta$ interface it holds $\Delta^\beta = (c_E - c^e_{\gamma\beta})/(c_\beta - c_E) = -\Delta^\alpha$ for the supersaturation. The curvature is positive when the α- or β-phase bulges into the γ-phase, where $\kappa = -y''(x)/(1 + y'(x)^2)^{3/2}$. We denote the capillarity lengths [41, 52] as

$$d_i = \frac{\gamma_i T_E}{L m_i \Delta c}. \tag{4.10}$$

Here m_i is the absolute value of the slope of the solvus lines, $\|dT/dc_{solvus}\|$, L is the effective latent heat[41] and $\Delta c = c_\beta - c_E$. The surface tension γ_i between phase i and phase γ sets the opening ϕ angle, we obtain $\sin(\phi - \pi/2) = \gamma_{\alpha\beta}/2\gamma_\alpha$, as shown in Fig. 4.5.

The symmetry of the phase diagram, namely $\|dT/dc_{\gamma-\gamma/\alpha}\| = \|dT/dc_{\gamma-\gamma/\beta}\|$ and thus $(c_E - c^e_{\gamma\beta}) = (c^e_{\gamma\alpha} - c_E)$ reduce the problem to the consideration of the $\gamma - \alpha$ or $\gamma - \beta$ - interface finally.

To conclude the development of the model, we cast the system of equations Eq. (4.7) to (4.9) into one integro-differential equation by means of the Green's function technique, see section 2.4. We consider the $\gamma - \beta$-interface to solve the entire problem, and we obtain:

$$\Delta - \frac{d}{R}\kappa = -\frac{p}{\pi}\int_{-\infty}^{0} dx' e^{-p(y-y')} K_0(p\eta(x,x')) + \frac{p}{\pi}\int_0^\infty dx' e^{-p(y-y')} K_0(p\eta(x,x')). \tag{4.11}$$

Here, $\eta = [(x-x')^2 + (y-y')^2]^{\frac{1}{2}}$ and K_0 is a modified Bessel function of zeroth order. The Peclet number p is defined as

$$p = \frac{\upsilon R}{2D},$$

R is the tip radius of the asymptotically fitted Ivantsov parabola. In Eq. (4.11), we see the similarity to classical dendritic growth. However, the occurence of sources and sinks on the boundary crucially changes the selection as we shall see when we present the numerical results. Before, we obtain the velocity scaling of the system.

Analytic Prediction of the Velocity Scaling

We consider the diffusion at the interface in the asymptotic region. Thereby, we are mainly interested in the regime of small supersaturations, where we assume the fluxes in the onsetting phases to be much larger than in the γ phase. In Eq. (4.8), we can thus substitute the gradient of the concentration in phase (β) by Δ/x in dimensionless notation and neglect the gradient in phase (γ). Then, matter conservation reads as

$$D\frac{\Delta}{x} = -\upsilon\frac{dx}{dy}. \tag{4.12}$$

Integration for $y(x)$ and comparing to the Ivantsov solution $y_{Iv} = -x^2/2R$ yields from

$$y(x) = -\frac{\upsilon}{D\Delta}\frac{x^2}{2} \equiv -\frac{x^2}{2R}$$

and $p = \upsilon R/2D$ that the Peclet relation holds here as

$$\Delta = 2p. \tag{4.13}$$

Apart from the modifed Peclet relation, it is suggested to approximate $K_0(x)$ in Eq. (4.11) for small arguments $x \ll 1$ as

$$K_0(x) \mapsto -\log\left(\frac{\|x\|}{2}\right).$$

Combined with Eq. (4.13), we derive a p-independent integro-differential equation,

$$2 - \sigma\kappa = \frac{1}{2\pi}\int_0^\infty dx' \log\left(\frac{(x+x')^2 + (y-y')^2}{(x-x')^2 + (y-y')^2}\right). \tag{4.14}$$

By $\sigma = d/Rp$ we denote the solvabilityparameter, which determines the velocity as

$$\frac{d\upsilon}{D} = 2\sigma p^2. \tag{4.15}$$

We can conclude that the velocity, which is determined by the solvability parameter and the Peclet number as given by Eq. (4.15), scales as $\upsilon \sim \Delta^2$, which is in contrast to the velocity scaling known from classical dendritic growth, where $\upsilon \sim \Delta^4$.

Numerical Results and Discussion

Apart from the obtained velocity scaling, we numerically solved Eq. (4.14). We calculate the depedence of the solvabilityparameter σ on the opening angle ϕ. Here, the difference to classical dendritic growth becomes apparent when one considers the case $\phi = \pi/2$ in Fig. 4.7, which is not a singular point here. The eigenvalue is continuous across $\phi = \pi/2$. Here the regime of $\phi < \pi/2$ corresponds to the growth of γ phase on expense of the α and β phase when $T_0 > T_E$, whereas for $\phi > \pi/2$, the α and β phase grow at $T_0 < T_E$ from the γ phase.

Though we found the described solutions to obey a potentially dominant velocity scaling, we should explain to what extent we may expect observation of these patterns. This mostly concerns two issues, specifically the symmetry assumptions and the structure of the initial seed. Recent

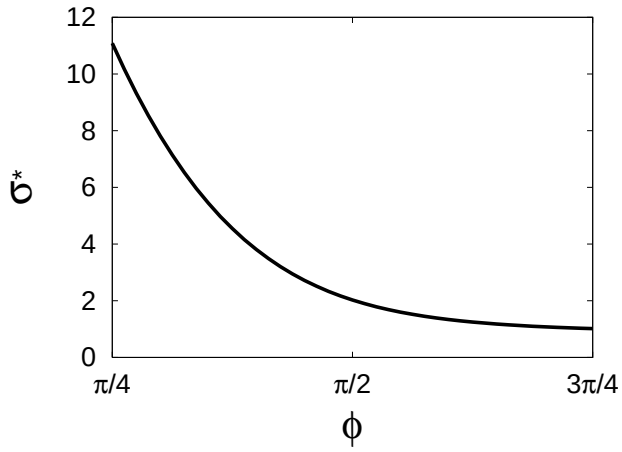

Figure 4.7: The solvabilityparameter σ for opening angles varying from $\pi/4$ to $3\pi/4$. Angles $\phi < \pi/2$ correspond to growth of the γ -phase from the α and β -phase, angles $\phi > \pi/2$ to growth of the α and β -phase from the γ -phase.

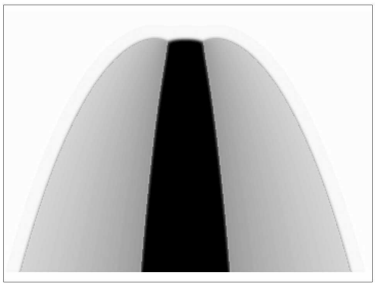

Figure 4.8: First phase-field results from [11]. The white phase is the mother γ phase, the grey and black being either α or β.

results in phase-field simulations [11] support the suspicion that the solution which we showed here exists only in the case of the introduced symmetry assumptions. If we introduce a slight asymmetry in the phase diagram, the eutectoid crystal we show in Fig. 4.5 is replaced by a generic solution, which we present in Fig. 4.8. In this sense, the solutions which we calculated should be understood as special case of a highly symmetrized system, whereas the generic structure of the onsetting eutectoid pattern is probably the one which we show in Fig. 4.8.

Concerning the structure of the initial seed, the observation of isolated eutectoid or eutectic dendrites requires seeds with both α and β phase contained. Seeds with only one of both phases would not exhibit the eutectoid structure we investigated here. Up to now, we have not found experimental results which could verify this prediction.

4.2 Transitions of Monotectic Type

Like the previously discussed eutectic and eutectoid transitions, the monotectic transition is a reaction of binary mixtures. Similar to the eutectic reaction, where a liquid solidifies into two solid phases, the monotectic point marks temperature and concentration where from a reference liquid phase a new liquid phase and a solid phase set on. To introduce the monotectic reaction, we first consider the phase diagram shown in Fig. 4.9.

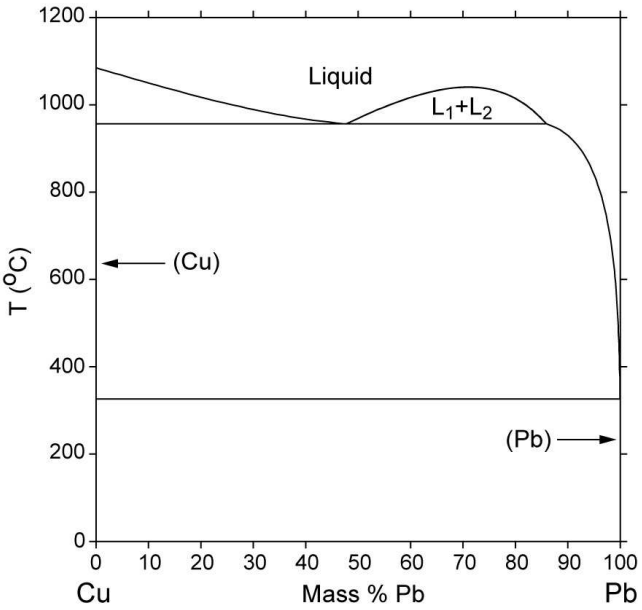

Figure 4.9: The phase diagram of the Cu-Pb system [64], exemplarily for the monotectic reaction.

Assuming we start at 70 percent of tin and 1100 °C, and cool the system down. Around 1020 °C, the critical temperature of the liquid miscibility gap is reached, and at approximatly 1000 °C, we find liquid 1 at $\approx$ 55%, liquid 2 at $\approx$ 82%. Further cooling down to the monotectic temperature T_m at $\approx$ 950 °C gives liquid 1 at $\approx$ 47% and liquid 2 at $\approx$ 87%. Further cooling at T_m leads to the monotectic reaction $L_1 \rightarrow L_2 + S$, until all liquid 1 is consumed. When the monotectic reaction finishes, the continuing cooling lets copper precipitate. Systems of importance for industrial applications which also exhibit a monotectic point are other copper mixtures [30], some iron mixtures [82] and also various aluminium mixtures [26]. Introduction to monotectic transitions with less focus on a specific material can be found e.g. in [72, 63, 79]

4.2.1 The Decomposed Monotectic Geometry

We introduce a new monotectic geometry - basically, it allows to discuss dendritic growth along a liquid-liquid boundary. We will address some initial assumptions about the system, and consequently present a first system of governing equations.

As the formal approach we undertake does not fold down to a comparably overviewable representation as in the case of eutectoid transitions, see section 4.1.2, we will discuss it in its very detail. This precise description of the proceeding is contained in section A.2 in the appendix. We

just state the final formulation here for the sake of readability.

The motivation for the considered geometry is apparent as it is of specific interest to study cases where the decomposition of the liquid phase has already taken place, being a state of the system which needs to be better understood in the field of monotectic transitions.

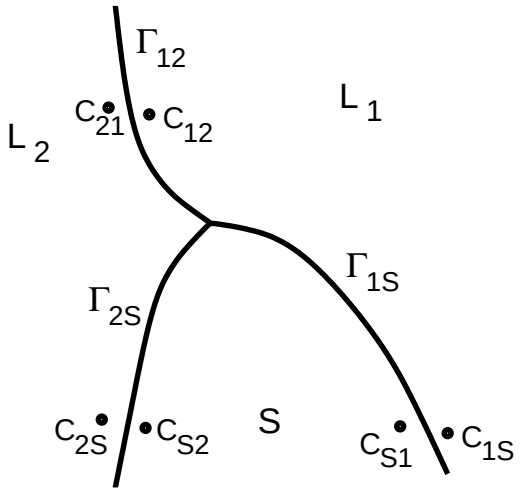

Figure 4.10: The geometry of the transition. We assume that the system initially consists of two liquid phases L_1, L_2. These two liquid phases are in metastable equilibrium at $y \to \infty$. The concentration c_{ij} is the concentration of phase i close to the i/j - interface.

The geometry of the system with the corresponding concentrations is sketched in Fig. 4.10. The phases L_1 and L_2 are the liquid phases which are at equilibrium at $y \to +\infty$, S is the solid phase. The indexed concentrations c_{ij} are the equilibrium concentrations as they are shown in Figs. 4.12 and 4.10.

We see in Fig. 4.10 that the solid phase grows along the liquid-liquid boundary into y-direction. However, in contrast to the symmetric geometries we are used to from dendritic growth, the dendritic shape of the solid phase here is deformed in conjunction with a finite rotation of the triple junction. Also, the asymptotic lateral position of the liquid-liquid interface as $y \to \infty$ is shifted from the tip. We shall find that, even though we consider a case of dendritic growth, these new asymmetric pattern characteristics render this system comprisingly different to other cases of dendritic growth we encountered before. For a proper defintion of these new quantites, see Fig. 4.11.

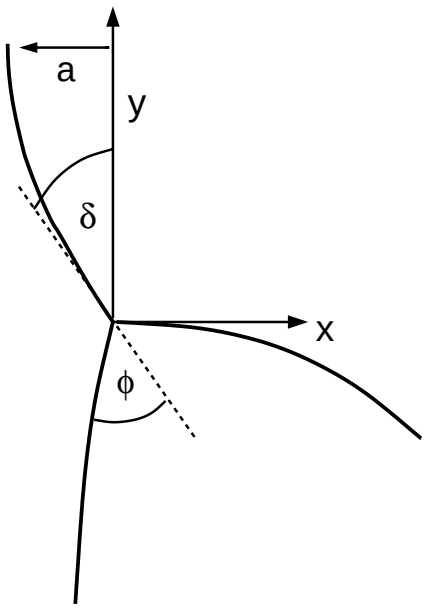

Figure 4.11: The rotational angle δ and the asymptotic lateral shift a are illustrated. The opening angle ϕ is defined by Young's law. The coordinate system is chosen such that the position of the triple junction is at $(0, 0)$.

Along the elementary assumptions for the system, we start with those concerning the diffusion processes. A first approximation we take here demands that the thermal diffusion in the system relaxes on appreciably smaller time scales compared to the chemical diffusion. Consequently, we assume an isothermal system at a temperature T, which is below the monotectic temperature T_m in all our cases. Next, we will assume that the chemical diffusion in the solid phase is much slower compared to that in the liquid phases. Thus, we neglect diffusion in the solid, leaving the liquid phases L_1, L_2 where the diffusion equation holds. The diffusion equation we consider here is the steady-state equation in a comoving frame of reference, denoted as

$$\nabla^2 c + \frac{2}{l_D}\partial_y c = 0, \tag{4.16}$$

where l_D is the chemical diffusion length and c the physical concentration. We assume identical diffusion lengths in both liquid phases, but the asymptotic concentrations at $y \to +\infty$ are different, see Fig. 4.10. In phase L_1, the equilibrium concentration at $y \to \infty$ is denoted by c_{12}, in phase L_2 by c_{21}. From the phase diagram in Fig. 4.12 we also see that we have a source at Γ_{1S}, where $c_{1S} \to c_{S1}$. As we assume no diffusion in the solid phase S, we obtain

$$v_n(c_{1S} - c_{S1}) = -D\vec{n}(\nabla c)_{|1}, \tag{4.17}$$

the flux in L_1 transports the material set free. Accordingly, at the interface Γ_{2S}, where we also have a source as $c_{2S} \to c_{S2}$,

$$v_n(c_{2S} - c_{S2}) = -D\vec{n}(\nabla c)_{|2}, \tag{4.18}$$

and at the interface Γ_{12}, a sink $\sim v_n(c_{12} - c_{21})$ is present. Diffusion in both phases means that we have here

$$v_n(c_{12} - c_{21}) = -D\vec{n}((\nabla c)_{|1} - (\nabla c)_{|2}). \tag{4.19}$$

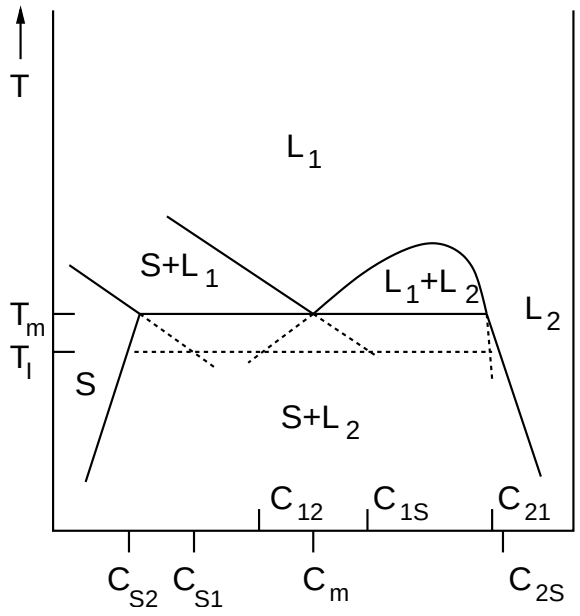

Figure 4.12: A schematic phase diagram of the system under consideration. Especially we assume linearized metastable prolongations of the equilibrium lines, $\|dT/dc_{ij}\| = const$ at $T \leq T_m$

The system of governing equations is completed by the local equilibria at the distinct interfaces, written as

$$\begin{aligned}
\Gamma_{21}: \; c &= c_{21} - \frac{\gamma_{12} T_m}{m_{21} L_{12}} \kappa \\
\Gamma_{2S}: \; c &= c_{2S} - \frac{\gamma_{2S} T_m}{m_{2S} L_{2S}} \kappa \\
\Gamma_{12}: \; c &= c_{12} - \frac{\gamma_{12} T_m}{m_{12} L_{12}} \kappa \\
\Gamma_{1S}: \; c &= c_{1S} - \frac{\gamma_{1S} T_m}{m_{1S} L_{1S}} \kappa
\end{aligned} \tag{4.20}$$

where the surface tensions are denoted by γ_{ij}, the slopes of the lines separating the phases in the phase diagram by $m_{ij} = \|dT/dc_{ij}\|$ and the effective latent heats, referring for their defintions to [40], by L_{ij}. Concerning the behaviour of the $m_{ij} = \|dT/dc_{ij}\|$, we will impose linearized behaviour below T_m, as sketched in Fig. 4.12. The opposition of the Mullins-Sekerka instability and the Gibbs-Thomson effect, which is included in Eqs. (4.20), is explained in detail in section 2.3.1. The following paragraph yields the desired representation of Eqs. (4.16) to (4.20), the detailed derivation is presented in section A.2 in the appendix.

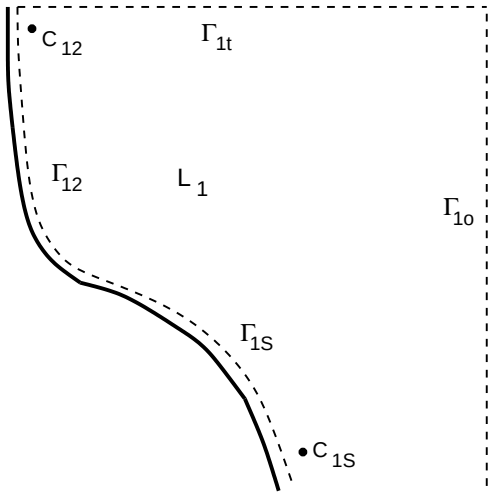

Figure 4.13: A sketch of the boundary of phase L_1. The triple junction is located at $(0, 0)$.

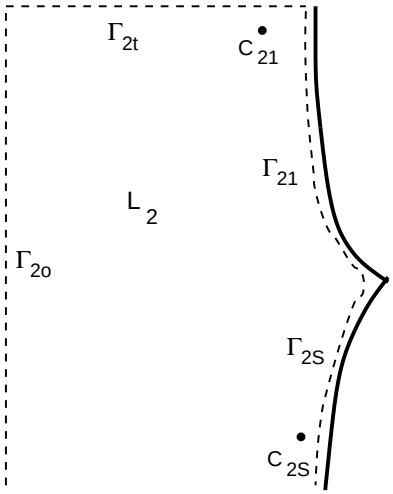

Figure 4.14: A sketch of the boundary of phase L_2.

Closed Representation of the One-Sided Model Here we summarize the representation of the problem we just described in the previous part of this section. We briefly state the closed representation of the governing equations we gave in Eqs. (4.16) to (4.20) and provide the definitions of the involved quantities. The four equations we state are the equations of local equilibrium

on the interfaces. For phase L_2, we obtained on interface Γ_{21}

$$
\begin{aligned}
- \quad & \frac{\Delta c_{21}}{\Delta c_{2S}} \frac{d_{21}}{2R_1} \kappa \\
= \quad & \frac{p_1}{2\pi} \int_{-\infty}^{0} dx' e^{-p_1(y-y')} \Bigg(2K_0(p_1\eta) \\
+ \quad & \left(\Delta_2 - \frac{d_{2S}}{R_1} \kappa' \right) \left[\frac{-\frac{dy}{dx'}(x-x') + (y-y')}{\eta} K_1(p_1\eta) - K_0(p_1\eta) \right] \Bigg) \\
- \quad & \frac{1}{2\pi} \int_{-a/R_1}^{0} dx' e^{-p_1(y-y')} \frac{ds}{dx'} \Bigg(K_0(p_1\eta) (\nabla' c)_{\Gamma(21)} \vec{n}' \\
- \quad & p_1 \frac{\Delta c_{21}}{\Delta c_{2S}} \left(-\frac{d_{21}}{R_1} \kappa' \right) \left[\frac{-\frac{dy}{dx'}(x-x') + (y-y')}{\eta} K_1(p_1\eta) - K_0(p_1\eta) \right] \Bigg).
\end{aligned}
\tag{4.21}
$$

Here, the miscibility gaps are denoted by $\Delta c_{21} = c_{21} - c_{12}$ and $\Delta c_{2S} = c_{2S} - c_{S2}$. The capillarity lengths are defined as $d_{2S} = \gamma_{2S} T_m / \Delta c_{2S} L_{2S} m_{2S}$, $d_{21} = \gamma_{12} T_m / \Delta c_{21} L_{21} m_{21}$, where γ_{ij} is the surface tension, L_{ij} the effective latent heat, and $m_{ij} = \|dT/dc_{ij}\|$. The Peclet number is defined according to the dendritic interface in contact with liquid phase L_1, $p_1 = \upsilon R_1 / 2D$ where R_1 is the tip radius of curvature of the asymptotically matching Ivantsov parabola. By D we denote the chemical diffusion constant, by a we denote the asymptotic lateral shift of the liquid-liquid interface relative to the triple junction, see Fig. 4.11. The modified Bessel function of zeroth and first order $K_{0,1}$ is of argument $p_1\eta$, where $\eta = \|\vec{r} - \vec{r}'\|$. The supersaturation Δ_2 is given as $\Delta_2 = (c_{2S} - c_{21})/\Delta c_{2S}$. After this comprising list of involved quantities, we come to the interface between solid and liquid phase L_2. On Γ_{2S} we have

$$
\begin{aligned}
\tfrac{1}{2} \quad & \left(\Delta_2 - \frac{d_{2S}}{R_1} \kappa \right) \\
= \quad & \frac{p_1}{2\pi} \int_{-\infty}^{0} dx' e^{-p_1(y-y')} \Bigg(2K_0(p_1\eta) \\
+ \quad & \left(\Delta_2 - \frac{d_{2S}}{R_1} \kappa' \right) \left[\frac{-\frac{dy}{dx'}(x-x') + (y-y')}{\eta} K_1(p_1\eta) - K_0(p_1\eta) \right] \Bigg) \\
- \quad & \frac{1}{2\pi} \int_{-a/R_1}^{0} dx' e^{-p_1(y-y')} \frac{ds}{dx'} \Bigg(K_0(p_1\eta) (\nabla' c)_{\Gamma(21)} \vec{n}' \\
- \quad & p_1 \frac{\Delta c_{21}}{\Delta c_{2S}} \left(-\frac{d_{21}}{R_1} \kappa' \right) \left[\frac{-\frac{dy}{dx'}(x-x') + (y-y')}{\eta} K_1(p_1\eta) - K_0(p_1\eta) \right] \Bigg).
\end{aligned}
\tag{4.22}
$$

The Eqs. (4.21) and (4.22) are the governing equations in liquid phase L_2, and they are coupled with those for liquid phase L_1. In the liquid phase L_1, the resulting representation of the local

equilibrium on the liquid-liquid interface Γ_{12} reads as

$$
\begin{aligned}
- \quad & \frac{\Delta c_{21}}{\Delta c_{1S}} \frac{d_{12}}{2R_1} \kappa \\
= \quad & \frac{p_1}{2\pi} \int_0^\infty dx' e^{-p_1(y-y')} \Bigg(2K_0(p_1\eta) \\
+ \quad & \left(\Delta_1 - \frac{d_{1S}}{R_1} \kappa' \right) \left[\frac{-\frac{dy}{dx'}(x-x') + (y-y')}{\eta} K_1(p_1\eta) - K_0(p_1\eta) \right] \Bigg) \\
+ \quad & \frac{p_1}{2\pi} \int_{-a/R_1}^0 dx' e^{-p_1(y-y')} \Bigg(\frac{ds}{dx'} K_0(p_1\eta) \left(2 \frac{(c_{21}-c_{12})}{\Delta c_{1S}} + \frac{\nabla c_{\Gamma(21)} \vec{n}'}{p_1} \right) \\
+ \quad & \frac{\Delta c_{21}}{\Delta c_{1S}} \left(-\frac{d_{12}}{R_1} \kappa' \right) \left[\frac{-\frac{dy}{dx'}(x-x') + (y-y')}{\eta} K_1(p_1\eta) - K_0(p_1\eta) \right] \Bigg).
\end{aligned}
\tag{4.23}
$$

The capillarity lengths are defined as $d_{1S} = \gamma_{1S} T_m / \Delta c_{1S} L_{1S} m_{1S}$, $d_{12} = \gamma_{12} T_m / \Delta c_{21} L_{21} m_{12}$, and the supersaturation Δ_1 is given as $\Delta_1 = (c_{1S} - c_{12})/\Delta c_{1S}$. Finally, the equation which completes the set of governing equations for the entire system describes the local equilibrium in liquid phase L_1 on the liquid-solid interface.

$$
\begin{aligned}
\tfrac{1}{2} \quad & \left(\Delta_1 - \frac{d_{1S}}{R_1} \kappa \right) \\
= \quad & \frac{p_1}{2\pi} \int_0^\infty dx' e^{-p_1(y-y')} \Bigg(2K_0(p_1\eta) \\
+ \quad & \left(\Delta_1 - \frac{d_{1S}}{R_1} \kappa' \right) \left[\frac{-\frac{dy}{dx'}(x-x') + (y-y')}{\eta} K_1(p_1\eta) - K_0(p_1\eta) \right] \Bigg) \\
+ \quad & \frac{p_1}{2\pi} \int_{-a/R_1}^0 dx' e^{-p_1(y-y')} \Bigg(\frac{ds}{dx'} K_0(p_1\eta) \left(2 \frac{(c_{21}-c_{12})}{\Delta c_{1S}} + \frac{\nabla c_{\Gamma(21)} \vec{n}'}{p_1} \right) \\
+ \quad & \frac{\Delta c_{21}}{\Delta c_{1S}} \left(-\frac{d_{12}}{R_1} \kappa' \right) \left[\frac{-\frac{dy}{dx'}(x-x') + (y-y')}{\eta} K_1(p_1\eta) - K_0(p_1\eta) \right] \Bigg)
\end{aligned}
\tag{4.24}
$$

Altogether, Eqs. (4.21) to (4.24) contain all necessary information to determine the physical behaviour of the system. Our main interest is on the velocity of the steady-state transformation, and we also have to consider the dependencency of the rotational angle δ and the asymptotic lateral shift a on the various parameters of the phase diagram, not only on the temperature which sets the supersaturations Δ_1 and Δ_2.

The representation of the system by Eqs. (4.21) to (4.24) is, though formally correct, full of implicit dependencies of the included parameters, which make it difficult to access the essential behaviour of the system.

Also, the numerical implementation exhibits some appreciable drawbacks. When we compare the equations we obtained here to those from the previous problems on dendritic growth, the asymmetry of the onsetting shape and the liquid-liquid interface already lead to a factor three of equations to solve, and the unknown normal projection of the concentration gradient on Γ_{21} makes a factor four of that. For the numerical solvers which are dedicated to such problems - multi-

dimensional nonlinear root-finding - the probability of success on such high-dimensional systems of highly complicated equations rapidly decreases with increasing dimensionality. On the other hand, reducing the spatial resolution of the system by a factor four to leads to nonsatisfactory testing behaviour. As experience tells, such rough resolutions destroy the mass conservation of the system, and the Ivantsov relation is not properly reproduced by the code.

Nevertheless, the calculations from Eq. (4.16) to (4.24) and the detailed description in the appendix, see A.2, are primarliy intended to give a detailed example for the application of the Green's function method when the approach discussed in section 2.4 is not feasible. The next paragraph describes the formal proceeding to get a 1-sided liquid-liquid symmetric model for the considered geometry, which solves some of the just mentioned problems.

The One-Sided Liquid-Liquid Symmetric Model We stress that the closed formulation for the monotectic geometry we consider demands the solution of four coupled massively nonlinear integro-differential equations. It is required to search for further simplifications we can introduce in the system without losing the essential physics.

This paragraph discusses what we call one-sided liquid-liquid symmetric model. We consider diffusion in the two liquid phases, rendering the problem 1-sided, but the new simplification comes from the formal symmetrization of the two liquid phases. When we assume identical diffusion constants D in both liquid phases as well as $(\partial\mu/\partial c)_{eq}$ - where eq indicates that the slope of the chemical potential is taken at each equilibrium concentration - we may add the representations of the fields in both domains of definition. Though this is the formally most straightforward approach, we shift the detailed description to the appendix, see A.2, and present here a rather elegant formulation for a better arrangement.

We treat the two liquid phases as one, and apply the well-known 1-sided model [24] for this liquid-solid system. Then the liquid-liquid interface can be introduced quite elegant when we consider the sources as inhomogeneity in Eq. (4.16) which is incorporated by means of a delta distribution δ_Γ like

$$\nabla^2 c + \frac{2}{l_D}\partial_y c = \frac{v}{D} n_y \delta_\Gamma. \tag{4.25}$$

Here the delta distribution δ_Γ is defined by

$$\int_V dv\ \delta_\Gamma = \int_\Gamma d\Gamma. \tag{4.26}$$

The obtained representation of the field thus provides us with one integral representation valid for all points of observation in both liquid phases, including the boundaries. We define it as $I_\sum \Delta c_{21}$ as it is the sum of the integrals along Γ_{1S}, Γ_{2S} and Γ_{12} and choose to have $I_\sum$ dimensionless, where the prefactor Δc_{21} indicates that we will normalize the concentrations by the liquid-liquid

miscibility gap. For $I_\sum$, we obtain:

$$\begin{aligned} I_\sum(\vec{x})\Delta c_{21} &= -\int_{\Gamma'(1S)} ds' \left(G\nabla'\bar{c}_1 - \bar{c}_{1S}\nabla' G + \frac{2}{l_D}\bar{c}_{1S} G\vec{e}_y \right)\vec{n}' \\ &- \int_{\Gamma'(2S)} ds' \left(G\nabla'\bar{c}_2 - \bar{c}_{2S}\nabla' G + \frac{2}{l_D}\bar{c}_{2S} G\vec{e}_y \right)\vec{n}' \\ &- \int_{\Gamma'(12)} ds' \left(G(\nabla'\bar{c}_1 - \nabla'\bar{c}_2) - (\bar{c}_{12} - \bar{c}_{21})\nabla' G + \frac{2}{l_D}(\bar{c}_{12} - \bar{c}_{21}) G\vec{e}_y \right)\vec{n}', \end{aligned} \tag{4.27}$$

where $\Delta c_{21} = c_{21} - c_{12}$, and the same assumptions concerning the contributions to the integrals by the interfaces $\Gamma_{1t,2t,1o,2o}$, see Figs. 4.13 and 4.14, hold here. Now we see that the remaining unknown normal projection of one gradient of the concentration field at the liquid-liquid boundary, $\nabla\bar{c}_{2|\Gamma(21)}$ and see Eqs. (4.21) to (4.24), is eliminated. Only the difference of the concentration gradients remains - which is given by mass conservation.

Also, due to our choice of a concentration field which is continuous across the Γ_{12} - interface, all terms in the integral along Γ_{12} which are proportional to $(\bar{c}_{12} - \bar{c}_{21})$ vanish. This is a simple calculation but important, so we briefly give it here. The local equilibria in real concentrations read as

$$\begin{aligned} c &= c_{21} - \Delta c_{21} d_{12}\kappa \quad | \quad L_2 \\ c &= c_{12} - \Delta c_{21} d_{12}\kappa \quad | \quad L_1, \end{aligned} \tag{4.28}$$

where we apply the same capillarity length d_{12}. Consequently, in terms of the concentrations $\bar{c}$ we introduced, the local equilibria render the concentration continuous across the interface:

$$\begin{aligned} \bar{c} &= -\Delta c_{21} d_{12}\kappa \quad | \quad L_2 \\ \bar{c} &= -\Delta c_{21} d_{12}\kappa \quad | \quad L_1, \end{aligned} \tag{4.29}$$

which is the required interface behaviour of the concentration. From Eq. (4.27) we thus achieve

$$\begin{aligned} I_\sum(\vec{x})\Delta c_{21} &= -\int_{\Gamma'(1S)} ds' \left(G\nabla'\bar{c}_1 - \bar{c}_{1S}\nabla' G + \frac{2}{l_D}\bar{c}_{1S} G\vec{e}_y \right)\vec{n}' \\ &- \int_{\Gamma'(2S)} ds' \left(G\nabla'\bar{c}_2 - \bar{c}_{2S}\nabla' G + \frac{2}{l_D}\bar{c}_{2S} G\vec{e}_y \right)\vec{n}' \\ &+ \int_0^\infty dy' \frac{dx}{dy'}\frac{\upsilon}{D}(c_{21} - c_{12})G \end{aligned} \tag{4.30}$$

The last line of Eq. (4.30) contains all remaining contributions from the Γ_{12} - interface, obviously far more convenient than the expressions we had before, confer e.g. with Eq. (4.24). We choose to rescale all lengths by the tip radius of curvature of the Ivantsov parabola that matches the interface Γ_{1S} asymptotically, R_1. The capillarity lengths are defined as $d_i = \gamma_i T_m / L_i m_i \Delta c_i$, $i = 12, 1S, 2S$, where we denote by γ_i the surface tension, by T_m the monotectic temperature, L_i is the effective latent heat, see [40]. We define m_i as the absolute slope of the line in the phase diagram describing the coexistence of the corresponding phases, and Δc_i are the miscibility gaps, $\Delta c_{1S} = c_{1S} - c_{S1}$, $\Delta c_{2S} = c_{2S} - c_{S2}$, $\Delta c_{21} = c_{21} - c_{12}$. For the integral representation of the concentration in both

liquid phases we consequently obtain

$$
\begin{aligned}
I_\Sigma \Delta c_{21} \;=\; & \qquad (4.31)\\
& + \frac{p_1}{2\pi}\int_0^\infty dx' e^{-p_1(y-y')}\Big[2\Delta c_{1S} K_0(p_1\eta)\\
& + \left((c_{1S}-c_{12}) - \Delta c_{1S}\frac{d_{1S}}{R_1}\kappa\right)\left[\frac{-\frac{dy}{dx'}(x-x')+(y-y')}{\eta}K_1(p_1\eta) - K_0(p_1\eta)\right]\Big]\\
& + \frac{p_1}{2\pi}\int_{-\infty}^0 dx' e^{-p_1(y-y')}\Big[2\Delta c_{2S} K_0(p_1\eta)\\
& + \left((c_{2S}-c_{21}) - \Delta c_{2S}\frac{d_{2S}}{R_1}\kappa\right)\left[\frac{-\frac{dy}{dx'}(x-x')+(y-y')}{\eta}K_1(p_1\eta) - K_0(p_1\eta)\right]\Big]\\
& + \frac{p_1}{\pi}\int_0^\infty dy' \frac{dx}{dy'}\Delta c_{21} e^{-p_1(y-y')}K_0(p_1\eta),
\end{aligned}
$$

where the argument of the modified Bessel function η is $\eta = \|\vec{r}-\vec{r}'\|$. We mention that we normalize the concentrations with respect to the miscibility gap between the two liquid phases, Δc_{21}. This leads to the occurence of ratios $\Delta c_{1S}/\Delta c_{21}$ and $\Delta c_{2S}/\Delta c_{21}$ in the representations and the equations of local equilibria which follow.

$$
\begin{aligned}
-\frac{d_{12}}{R_1}\kappa &= I_\Sigma \quad | \quad \vec{x}\in\Gamma_{12} \qquad (4.32)\\
\frac{1}{2}\frac{\Delta c_{1S}}{\Delta c_{21}}\left(\Delta_1 - \frac{d_{1S}}{R_1}\kappa\right) &= I_\Sigma \quad | \quad \vec{x}\in\Gamma_{1S}\\
\frac{1}{2}\frac{\Delta c_{2S}}{\Delta c_{21}}\left(\Delta_2 - \frac{d_{2S}}{R_1}\kappa\right) &= I_\Sigma \quad | \quad \vec{x}\in\Gamma_{2S}
\end{aligned}
$$

The system of coupled nonlinear integro-differential equations stated by Eq. (4.32) is the basis of our numerical approach to the system. Obviously, this representation of the system makes life easier, when we compare with Eqs. (4.21) to (4.24). Now, we solve for the three interfaces $\Gamma_{1S}, \Gamma_{2S}, \Gamma_{12}$, the ratio of the capillarity length d_{12} and radius R_1, the rotational angle δ and the asymptotic lateral shift relative to the tip, a.

For the numerical implementation, two features of Eq. (4.32) are most important. First, it reduced the dimension of the equation system stated by Eqs. (4.21) to (4.24) by 25 %. Second, the complexity of the integrals along the liquid-liquid interface is reduced. This leads to a good testing behaviour of the code for the one-sided symmetric code, and in the next subsection we discuss some tests in more detail.

Test Proceeding for the Code

In this short section we briefly mention the tests for the used code, which assure the physical and numerical consistence of the obtained results. Some exemplary test results are shown.

Tests for the Numerical Approach: 1-Sided Isotropic Classical Dendritic Growth

One suggested test for a certain part of the code is the solution of the isotropic classical dendritic

growth problem, in a one-sided model. Though we may not expect matching of the symmetric-model results known from [57], we require this one-sided model to reproduce the qualitative behaviour of the solvability parameter $\sigma = d/pR$ - i.e., that $\sigma \to 0$ for a smooth tip. Verification of this test already would imply a sufficient cut-off length of the system at $y \to -\infty$, proper evaluation of the now more complicated integral kernels, and a proper resolution in this part of the system. We directly present the equation for the 1-sided model,

$$\frac{1}{2}\left(\Delta - \frac{d}{R}\kappa\right) = \frac{p}{2\pi}\int dx' \exp^{-p(y-y')}\left(\left(\Delta - \frac{d}{R}\kappa\right)\left[\left(\frac{-\frac{dy}{dx}(x-x') + (y-y')}{\eta}\right)K_1(p\eta) - K_0(p\eta)\right] + 2K_0(p\eta)\right).$$

The test covers a large range of opening angles, and the expected qualitative behaviour is satisfied, as shown in Fig. 4.15.

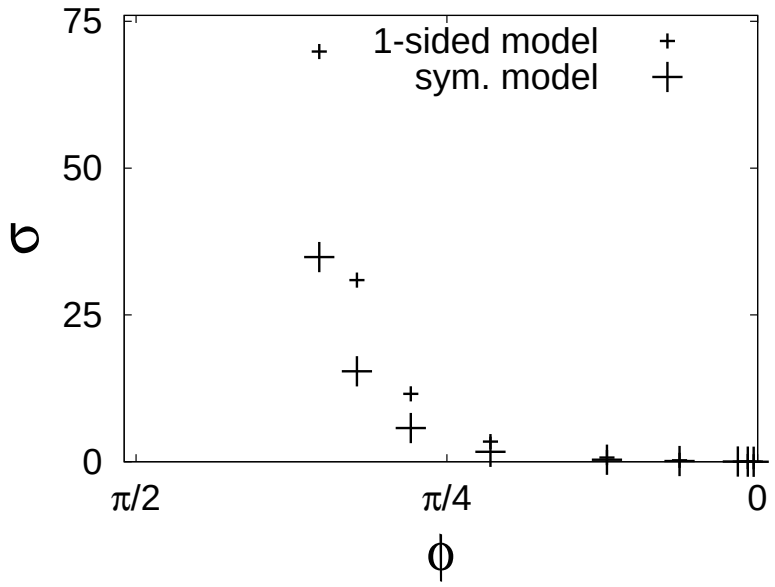

Figure 4.15: The solvabilityparameter behaves as expected, $\sigma \to 0$ as the slope tends to zero.

Apart from this test, we also can consider the behaviour of the 1-sided model when we introduce asymmetric Peclet numbers p_1, p_2. Then, we investigate the dependence of the rotational angle δ on the asymmetry of the Peclet numbers. We expect that δ tends to zero when the Peclet numbers take the same value. Also, we assume that δ satisfies $\delta \to -\delta$ when we invert the difference of the Peclet numbers, $(p_1 - p_2)/(p_1 + p_2) \to (p_2 - p_1)/(p_1 + p_2)$. The test result for a fixed opening angle and a fixed sum of the Peclet numbers $p_1 + p_2 = 0.2$ is shown in Fig. 4.16

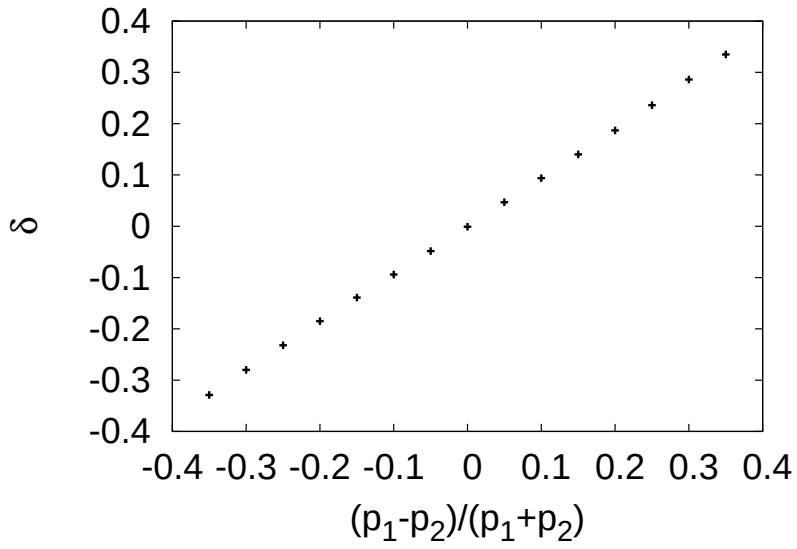

Figure 4.16: The rotational angle behaves as expected, $\delta \to 0$ as $p_1 \to p_2$.

The tests we performed in the 1-sided model of isotropic dendritic growth showed the expected results, meaning that we assume this kind of sub-problem of the entire monotectic system is solved properly.

Further Tests for the Numerical Approach After the just mentioned nontrivial test for the classical isotropic dendrite, we describe tests which lets us judge the functionality of the entire code. We introduce some basic tests to check if the system behaves as if it were extended infinitly in positive y-direction. The easiest test here is simply the asymptotic behaviour of the liquid-liquid interface. It needs to become a vertical line asymptotically, as we know that the deviation from the liquid-liquid equilibrium originates to the curvature of the liquid-liquid interface only.

The next test allows to check if the asymptotic lateral shift a is small relative to the length cut-off in positive y-direction. One can calculate an integral along the interface of one of the liquid phases at $y \to \infty$ to see if the numerical result coincides with the analytically predicted value. Though the calculation along this interface is not required in our model, it allows to verify that the cut-off at $y \to \infty$ is not problematic. When we consider the interface Γ_{1t}, see Fig. 4.13, at $y \to \infty$, it holds for a constant quantity q

$$\int d\Gamma'_{1t} \left[G\nabla' q - q\nabla' G + 2pq\, G\vec{e}_y \right] \vec{n} = \lim_{y\to\infty} \frac{p}{2\pi} \int_{\infty}^{a/R} -dx' \exp(-p(y-y')) \times \left(-q\left(K_0(p\eta) + \frac{(\vec{r}-\vec{r}')}{\|\vec{r}-\vec{r}'\|} \vec{e}_y K_1(p\eta) \right) + 2qK_0(p\eta) \right). \tag{4.33}$$

Since $K_0(p\eta)$ and $K_1(p\eta)$ decay exponentially for large arguments $p\eta \gg 1$, we can neglect all contributions to the integral beyond some finite value of x on Γ_{1t}. Consequently, for the limit

$y \to \infty$, it holds $(\vec{r} - \vec{r}') \parallel -\vec{e}_y$, and

$$\lim_{y\to\infty} \frac{p}{2\pi} \int_{\infty}^{a/R} -dx' \exp(-p(y-y'))q\left((K_0(p\eta) + K_1(p\eta))\right) \tag{4.34}$$

remains. We take the asymptotic expansion of the modified Bessel functions we consider here, [1]

$$K_\nu(z) \approx \sqrt{\frac{\pi}{2z}}\, e^{-z}\left(1 + \frac{\mu - 1}{8z} + \ldots\right) \mid \quad \mu = 4\nu^2, \tag{4.35}$$

to obtain

$$\lim_{y\to\infty} q\left(\frac{p}{2\pi}\right)^{1/2} \int_{a/R}^{\infty} dx' e^{-p(y-y')}\left(\frac{1}{\|\vec{r} - \vec{r}'\|}\right)^{1/2} e^{-p\sqrt{(x-x')^2+(y-y')^2}}. \tag{4.36}$$

We denote by $Y = y' - y, X = x' - x$ and use that [1]

$$(a+b)^k \approx a^k + ka^{k-1}b \quad \mid \quad b \ll a, \tag{4.37}$$

yielding

$$\lim_{y\to\infty} q\left(\frac{p}{2\pi}\right)^{1/2} \int_{a/R-x}^{\infty} dX e^{p\left[Y\left(1-\left(1+\frac{1}{2}X^2/Y^2\right)\right)\right]}\left(\frac{1}{Y\left(1+\frac{1}{2}\frac{X^2}{Y^2}\right)}\right)^{1/2}, \tag{4.38}$$

which is

$$\lim_{y\to\infty} q\left(\frac{p}{2\pi}\right)^{1/2} \int_{a/R-x}^{\infty} dX e^{-pX^2/2Y}\left(\frac{1}{\|Y\|}\right)^{1/2}. \tag{4.39}$$

From here, we get with $p = x\left(\sqrt{p/2\|Y\|}\right)$

$$\lim_{y\to\infty} q\left(\frac{p}{2\pi}\right)^{1/2} \int_{(p/2\|Y\|)(a/R-x)}^{\infty} dp\left(\frac{2\|Y\|}{p}\right)^{1/2} e^{-p^2}\left(\frac{1}{\|Y\|}\right)^{1/2}, \tag{4.40}$$

which is known [36] as

$$\frac{q}{\sqrt{\pi}} \int_0^{\infty} dp e^{-p^2} = \frac{q}{2}. \tag{4.41}$$

Summarizing, for this contribution $\sim q$ of the integral along Γ_{1t}, we obtain $q/2$. The relative error of $q/2$ enables the estimation of a proper cut-off at $y \to \infty$. For the asymptotic behaviour as $y \to -\infty$, we check if the calculated shape matches the Ivantsov solution at the numerical cut-off. Since we scaled all lengths by R_1, we need to find $y = -x^2/2$ on Γ_{1S} and $y = -x^2 p_1/2p_2$ on Γ_{2S}. Further tests which supplement the usual check for proper asymptotics and numerical consistence (meaning consistent results with respect to changes of the system length and discretization) include the continuity of the concentration field on the three interfaces close to the triple junction and a test for the phase geometry of the system. By the latter we mean that if we only exchange the liquid phases, we expect to find equal results when we take the rescaling by R_2 instead of R_1 into

account.

4.2.2 Numerical Solution of the One-Sided Liquid-Liquid Symmetric Model

In this section, we explain the choice of the proper control parameters, the investigated configurations, and we discuss the behaviour of the system. We assume we are close below the monotectic temperature T_m, and the physical control parameter be the temperature which we set to values below T_m. By the phase diagram, we thus fix the supersaturations, Δ_1, Δ_2 as well as the miscibility gaps $\Delta c_{1S}, \Delta c_{2S}, \Delta c_{21}$. We recall the equations to be solved on each interface,

$$\begin{aligned} -\frac{d_{12}}{R_1}\kappa &= I_\Sigma \quad | \quad \vec{x} \in \Gamma_{12} \\ \frac{1}{2}\frac{\Delta c_{1S}}{\Delta c_{21}}\left(\Delta_1 - \frac{d_{1S}}{R_1}\kappa\right) &= I_\Sigma \quad | \quad \vec{x} \in \Gamma_{1S} \\ \frac{1}{2}\frac{\Delta c_{2S}}{\Delta c_{21}}\left(\Delta_2 - \frac{d_{2S}}{R_1}\kappa\right) &= I_\Sigma \quad | \quad \vec{x} \in \Gamma_{2S} \end{aligned} \tag{4.42}$$

where

$$\begin{aligned} I_\Sigma \Delta c_{21} &= \\ &+ \frac{p_1}{2\pi}\int_0^\infty dx' e^{-p_1(y-y')}\Big[2\Delta c_{1S} K_0(p_1\eta) \\ &+ \left((c_{1S}-c_{12}) - \Delta c_{1S}\frac{d_{1S}}{R_1}\kappa\right)\left[\frac{-\frac{dy}{dx'}(x-x')+(y-y')}{\eta}K_1(p_1\eta) - K_0(p_1\eta)\right]\Big] \\ &+ \frac{p_1}{2\pi}\int_{-\infty}^0 dx' e^{-p_1(y-y')}\Big[2\Delta c_{2S} K_0(p_1\eta) \\ &+ \left((c_{2S}-c_{21}) - \Delta c_{2S}\frac{d_{2S}}{R_1}\kappa\right)\left[\frac{-\frac{dy}{dx'}(x-x')+(y-y')}{\eta}K_1(p_1\eta) - K_0(p_1\eta)\right]\Big] \\ &+ \frac{p_1}{2\pi}\int_0^\infty dy' \frac{dx}{dy'} e^{-p_1(y-y')} 2\Delta c_{21} K_0(p_1\eta). \end{aligned} \tag{4.43}$$

Fixing the temperature, we set all necessary parameters, except for the opening angle ϕ of the triple junction, see Fig. 4.11.

The ratio of capillarity length and radius, d_{12}/R_1, the rotation angle δ, see also Fig. 4.11, and the asymptotic lateral shift of the liquid-liquid interface to the y-axis as $y \to \infty$, a, are output of our code, in addition to the interface shape. Consequently, the steady-state velocity is obtained as

$$\frac{\upsilon d_{1S}}{D} = 2\frac{d_{1S}}{R_1}p_1, \tag{4.44}$$

being the information of main interest. We mention that the definition of a reduced representation of the equation system stated by 4.43 and the corresponding eigenvalues specific for this reduced representation requires further investigation. However, provided with this rough sketch of our approach, we turn to the results.

Results for Approximated Phase Diagrams and Discussion The results discussed in this short section stem from calculations which require further approximations. Though it is of interest to resolve all dependencies later on, we fix the miscibility gap while changing the supersaturations, to give an initial impression how the obtained results depend on separate parameters. We are interested in the dependence of the velocity, the rotational angle and the asymptotic lateral shift on the asymmetry of the supersaturations.

We choose the relative difference of the supersaturations $(\Delta_1 - \Delta_2)/(\Delta_1 + \Delta_2)$ to decrease with increasing Δ_t, where we define Δ_t as.

$$\Delta_t = \frac{T - T_m}{\left|\frac{dT}{dc_{1S}}\right| \Delta c_{21}(T = T_m)} \tag{4.45}$$

It turns out that in this case, the rotational angle decreases when the relative difference of Δ_1 and Δ_2 decreases, see Fig. 4.17. It is intuitive to find the rotational angle decreasing when the asymmetry of the supersaturations decreases while the miscibility gaps remain unchanged. To determine the rotational angle δ, keeping Δ_t fixed, but changing $\Delta_1 - \Delta_2/\Delta_1 + \Delta_2$, could show if the absolute value of Δ_t affects the rotational angle. Further investigation with changing ratios of the miscibility gaps $\Delta c_{iS}/\Delta c_{21}$, but - though quite artificial - fixing $\Delta_t, \Delta_1 - \Delta_2$ could also reveal the role of the $\Delta c_{iS}/\Delta c_{21}$. When we consider the asymptotic lateral shift a, we find that it also decreases when

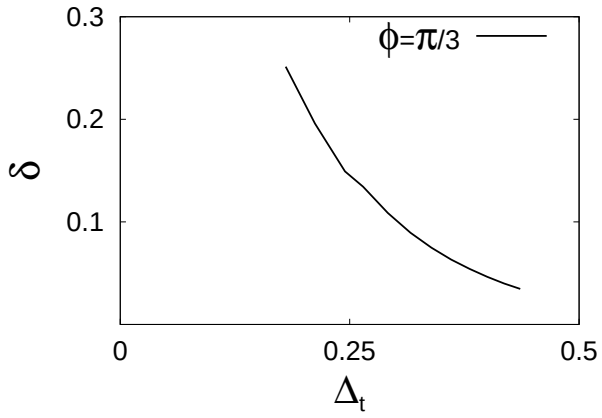

Figure 4.17: The development of the rotation angle, here the opening angle $\phi = 60°$. We assumed that the miscibility gaps stay constant relative to the changes in the supersaturations. Especially, the supersaturations were assumed to be of decreasing difference when Δ_t increases.

$\Delta_1 - \Delta_2$ decreases. One might have qualitatively expected such behaviour, as the asymptotic lateral shift is a parameter which indicates asymmetry in the system, just as the rotational angle.

We come to the steady-state velocity. In principle this is the parameter of main interest as it can tell us about dominance of the growth mode in a competitive regime. However, we just find here that the velocity shows a nearly linear growth for increasing Δ_t. Any further interpretation of the results require extensive studies on various other configurations, which are not in the scope of this thesis. The shown pictures are restricted to parts of the entire shape to show the slight change of

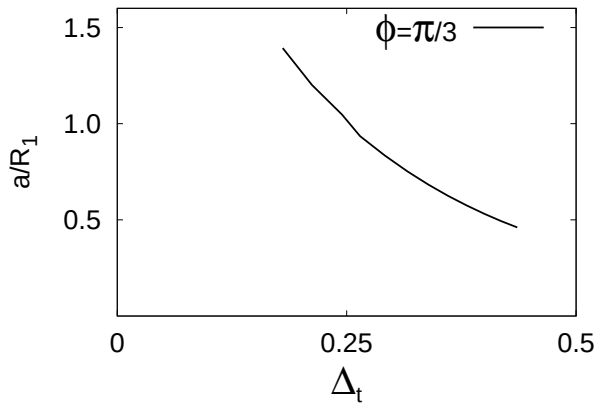

Figure 4.18: The asymptotic lateral shift decreases with increasing temperature Δ_t. Here the opening angle is $\phi = 60°$. The lateral shift here is directed into the left half plane, see Fig. 4.20.

curvature in a vicinity of the tip and have an appreciable spatial resolution of the most interesting part of it.

How specific characteristics of the interface, especially the rotational angle δ and the lateral asymptotic shift a, depend on the various parameters which one could include, e.g. a rigorous dependence of the miscibility gaps on the undercooling, is object of further investigations which we will conduct in the near future.

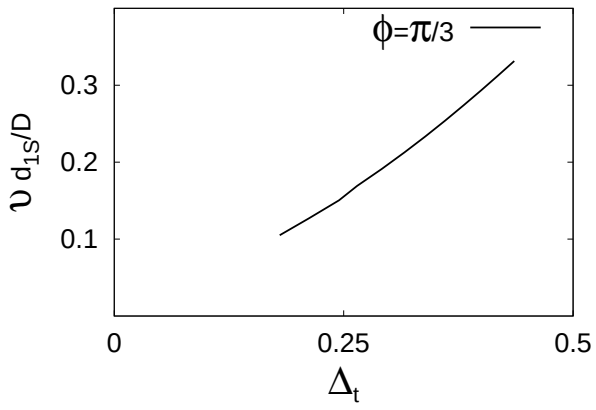

Figure 4.19: The velocity shows a nearly linear behaviour in the considered regime of undercoolings. Again, $\phi = 60°$ and we assumed the miscibility gaps stay constant relative to the changes in the supersaturations, which were assumed to be of decreasing difference when Δ_t grows.

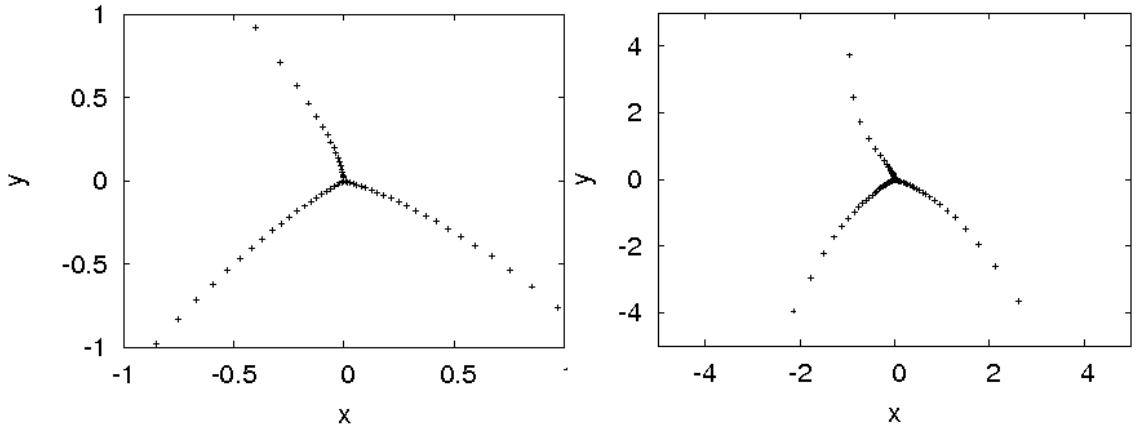

Figure 4.20: An exemplary shape plot, for $\phi = 60°$, with focus on the vicinity of the tip. When we compare the left panel which enlarges the tip area to the right panel, the liquid-liquid interface shows a change of curvature.

4.2.3 Conclusion

Within this chapter, we introduced two specific scenarios of phase transitions limited by chemical diffusion. For eutectoid transformations, we considered the growth of an isolated dendrite. This pattern appears when the initial seed contains both solid phases. Also, recent phase-field studies [11] indicate that already small deviations from the symmetries we impose on the system lead to a qualitatively different pattern. That pattern is probably the generic structure of this transition. Consequently, in the light of these recently obtained results, the solutions we find must be interpreted as special cases due to the highly symmetrized system we assume. This isolated growth

mode is especially interesting as it turns out that in the practically important regime of small supersaturations, it exhibits growth velocites which could dominate the competing growth modes. This is a very important pragmatic aspect, and it is accompanied by a rather theoretical, but as well interesting other feature of the system - the selection mechanism in dendritic growth in eutectoid systems behaves crucially different to that known from classical dendritic growth. We find a selection mechanism which continues operating beyond the opening angle $\phi = \pi/2$ - which corresponds to a smooth tip and is a singular point in classical dendritic growth. Further understanding of the detailed nature of the selection would probably require further analytic work and is beyond the scope of this thesis.

In the field of monotectic transitions, we investigated dendritic growth along the liquid-liquid interface, which appears in metastable decomposed states of the system. This problem exhibits various aspects which render its detailed understanding a demanding task. In contrast to the previously investigated systems, we cannot approach the problem in a comprisingly symmetrized model. Nevertheless, we establish what we call a 'one-sided liquid-iquid symmetric model', which indicates that we assume identical diffusion constants in the liquid phases, but neglect diffusion in the solid phase. Some very comfortable assumptions concerning the relevant phase diagram cannot be applied here. Consequently, we must take care of various internal dependencies.

Independent of these impediments, it is apparent that this system is particularly challenging. In classical dendritic growth, the selection chooses the growth velocity and the tip radius of curvature of the Ivantsov parabola which asymptotically matches the found solutions. In our model, the system also determines the asymptotic lateral shift of the liquid-liquid interface relative to the triple junction and the rotational angle of the triple junction.

We stress here that the results we obtained up to now for the monotectic system only grant first insights to the system. Additional investigation is necessary, especially concerning various intricate dependencies of the found solutions.

5 Summary

The aim of this thesis was to gain insights into various diffusional phase transitions and their relation to dendritic growth, specifically for the appearance of a selection. Our understanding of the prerequisites for the existence of steady-state solutions guided our approaches in all considered problems. The phenomena which we suspected to be crucial for the appearance of selection were included in the preferred representation for the study of dendritic selection problems, by means of the Green's function method. All considered problems have in common that the obtained nonlinear eigenvalue problems in terms of integral equations exhibit a solvability parameter σ. The solvability parameter reflects the solution behaviour of the corresponding system. Specifically, it selects in conjunction with the supersaturation or undercooling the transition velocity and the characteristic length scale of the growing dendritic pattern.

First, we investigated diffusional solid-solid transitions where we take into account elastic effects due to lattice strains and the diffusion of latent heat. In case of coherent phase interfaces, the lattice strains lead to associated stresses which affect the local equilibrium at the moving interface. We consider the fundamental lattice strains to find the essential effect of the elastic interactions, and we distinguish between single and bicrystal growth. The discrimination of single and bicrystal growth here takes into account that a triple junction alone already leads to selection.

We start with systems having a single crystal geometry. The first one is under pure dilatational lattice strain and can be solved entirely by means of a mapping to classical dendritic growth. Exploiting a nontrivial physical analogy allows to transfer the problem to that of dendritic growth with isotropic surface tension, which is known to lack selection. The numerical results support this argumentation. The numerical calculations for systems under pure shear also reveal the absence of steady-state solutions. However, the treatment of superpositions of pure dilatational and pure shear lattice strains, surprisingly exhibit steady-state solutions. The found selection features a fascinating orientation dependence; the superposition leads to steady-state growth in the direction oriented perpendicularly to the largest amplitude of the lattice strain. In the case of large lattice strains aligned parallel to the growth direction, the transition lacks selection. The found steady-state solutions show a velocity scaling $v \sim \sigma\tilde{\Delta}^4$, where $\tilde{\Delta}$ is the undercooling, which is shifted by the elastic hysteresis. Obviously, they obey the same power law as classical dendritic growth. As the found values of the solvability parameters are larger by orders of magnitude, the elastically induced selection leads to higher transition velocities compared to classical dendritic growth. The last scenario we consider in the single crystal geometry corresponds to a vanishing elastic hysteresis. If this solution existed, it would be energetically preferred, but our results suggest absence of selection here.

In the bicrystal geometry, we introduce the limit of a 'weak' triple junction, enabling us to study the influence of elastic effects without an additional selection due to the triple junction. The pure shear lattice strain exhibits a selection here, and yields possibly instable secondary solution branches when taking also the triple junction into account. Like for single crystal systems, we perform calculations for superpositions of pure dilatational and shear lattice strains. Again we

find a strong orientation dependence of the selection. Even though in bicrystal systems strong lattice strains parallel to the growth direction also lead to selection, the range of superpositions is limited. Compared to the case of perpendicular alignment of the strongest lattice strains relative to the growth direction, only 25% of the possible lattice strain configurations lead to steady-state growth. Nevertheless, this limited regime exhibits the larger solvability parameters, i.e. the larger transition velocities. Specifically for bicrystal growth with pure shear lattice strains, we investigate the limit of zero transition velocity. The resulting representation of the problem exhibits an elastic solvability parameter which lacks any thermal quantities, but our numerical studies remain quantitatively inconclusive even close to the point of zero velocity. The qualitative result we can deduct from these studies is the absence of a linear behaviour of the selection close to zero velocity. Both examplarily discussed cases of possible behaviour in the limit $v \to 0$ show a dominant growth behaviour compared to the previously found selection for this elastic configuration.

The second large branch of our calculations concerns transitions which are limited by chemical diffusion. The growth of an isolated eutectoid dendrite appears when the initial seed includes both emerging solid phases. We find a selection mechanism which is crucially different to that observed in classical dendritic growth. While in classical dendritic growth, the opening angle that marks the smooth tip is a singular point of the selection, here the selection persists beyond this point. In addition, we find analytically the asymptotic growth behaviour in the case of small supersaturations. It determines the growth velocity as $v \sim \sigma\Delta^2$, which is faster than in classical dendritic growth. The twinned pattern we found probably represents solutions which only exist within the massive symmetry assumptions we render for the system. We suspect that another isolated dendritic pattern represents the generic solutions which persist when we introduce small deviations to the imposed symmetries.

In a monotectic transition, we investigated the growth of an asymmetric dendrite along the liquid-liquid interface. The geometry consists of the liquid phases which are in equilibrium asymptotically and the growing dendrite. The triple junction of the system is rotated by an angle δ, and the liquid-liquid interface shows a lateral shift relative to the triple junction in equilibrium. In addition to the solvability parameter, we thus need to solve for two additional quantities. The conducted investigations on this system have confirmed the expected behaviour of those quantities which reflect the asymmetry of the system; the rotational angle and the asymptotic lateral shift of the liquid-liquid interface decrease when we reduce the asymmetry of the supersaturations. Also, a nearly linear growth of the transition velocity for increasing undercooling was observed.

Bibliography

[1] M. Abramowitz, I. A. Stegun, and R. H. Romer. *Handbook of Mathematical Functions with Formulas, Graphs, and Mathematical Tables*. 1988.

[2] M. S. Agranovich, Yu. V. Egorov, and M. A. Shubin. *Encyclopedia of Mathematical Sciences - PDEs IX*. Springer, 1991.

[3] M. Asta, C. Beckermann, A. Karma, W. Kurz, R. Napolitano, M. Plapp, G. Purdy, M. Rappaz, and R. Trivedi. Solidification microstructures and solid-state parallels: Recent developments, future directions. *Acta Materialia, Overviews*, 2009.

[4] A. Authier and A Zarembowitch. *International Tables for Crystallography*. 2006.

[5] G.I. Barenblatt and Y.B. Zeldovich. *The mathematical theory of combustion and explosions*. Consultants Bureau,New York, NY, 1985.

[6] D.M. Barnett. *Phys. Stat. Solidi B*, (49):741, 1972.

[7] M. Ben Amar and E. Brener. Theory of pattern selection in three-dimensional nonaxisymmetric dendritic growth. *Phys. Rev. Lett.*, 71:589–592, July 1993.

[8] M. Ben Amar and Y. Pomeau. Theory of dendritic growth in a weakly undercooled melt. *Europhysics Letters*, 2:307, August 1986.

[9] E. Ben-Jacob, Nigel Goldenfeld, B. G. Kotliar, and J. S. Langer. Pattern Selection in Dendritic Solidification. *Phys. Rev. Lett.*, 53(22):2110–2113, Nov 1984.

[10] C. M. Bender and S. A. Orszag. *Advanced Mathematical Methods for Scientists and Engineers*. New York: McGraw-Hill, 1978.

[11] G. Boussinot and E. A. Brener. *unpublished*.

[12] J. P. Boyd. The Devil's Invention : Asymptotic, Superasymptotic and Hyperasymptotic Series. *Acta Applicandae Mathematicae*, 56:1–89, 1999.

[13] E. Brener. Needle-crystal solution in three-dimensional dendritic growth. *Phys. Rev. Lett.*, 71:3653–3656, November 1993.

[14] E. Brener, T. Ihle, H. Müller-Krumbhaar, Y. Saito, and K. Shiraishi. Fluctuation effects on dendritic growth morphology. *Physica A*, 204:96–110, March 1994.

[15] E. Brener and D. Temkin. Noise-induced sidebranching in the three-dimensional nonaxisymmetric dendritic growth. *Phys. Rev. E*, 51:351–359, January 1995.

[16] E. A. Brener, C. Huter, D. Pilipenko, and D. E. Temkin. Velocity Selection Problem in the Presence of the Triple Junction. *Phys. Rev. Lett.*, 99:105701, 2007.

[17] E. A. Brener, V. I. Marchenko, and R. Spatschek. Influence of strain on the kinetics of phase transitions in solids. *Phys. Rev. E*, 75:444, 2007.

[18] E. A. Brener and V. I. Mel'Nikov. Pattern selection in two-dimensional dendritic growth. *Advances in Physics*, 40:53–97, January 1991.

[19] E.A. Brener, S.V. Iordanskii, and V.I. Marchenko. Elastic effects on the kinetics of a phase transition. *Phys. Rev. Lett.*, 82:1506–1509, 1999.

[20] E.A. Brener and V.I. Marchenko. Formation of nucleation centers in a crystal. *JETP Letters*, 56(7):381–385, Oct 1992.

[21] Richard C. Brower, David A. Kessler, Joel Koplik, and Herbert Levine. Geometrical Approach to Moving-Interface Dynamics. *Phys. Rev. Lett.*, 51(13):1111–1114, Sep 1983.

[22] Richard C. Brower, David A. Kessler, Joel Koplik, and Herbert Levine. Geometrical models of interface evolution. *Phys. Rev. A*, 29(3):1335–1342, Mar 1984.

[23] G. Caginalp. An analysis of a phase field model of a free boundary. *Archive for Rational Mechanics and Analysis*, 92:205–245, September 1986.

[24] B. Caroli, C. Caroli, B. Roulet, and J. S. Langer. Solvability condition for needle crystals at large undercooling in a nonlocal model of solidification. *Phys. Rev. A*, 33:442–452, January 1986.

[25] J. B. Collins and H. Levine. *Phys. Rev. B*, 31:6119, 1985.

[26] S.R. Coriell, W.F. Mitchell, B.T. Murray, J.B. Andrews, and Y. Arikawa. Analysis of monotectic growth: infinite diffusion in the l2 phase. *Journal of Crystal Growth*, (179), 1997.

[27] M. C. Cross and P. C. Hohenberg. Pattern formation outside of equilibrium. *Reviews of Modern Physics*, 65:851–1112, 1993.

[28] C.W. (1976a) Cryer. *MRC report*, 1657, 1976.

[29] C.W. (1976a) Cryer. *MRC report*, 1693, 1976.

[30] H.-B. Cui, J.-J. Guo, Y.-Q. Su, H.-S. Ding, S.-P. Wu, W.-S. Bi, D.-M. Xu, and H.-Z. Fu. Microstructure evolution of Cu-Pb monotectic alloys during directional solidification. *Trans. Nonferrous Met. Soc. China*, (16), 2006.

[31] S. H. Curnoe and A. E. Jacobs. Statics and dynamics of domain patterns in hexagonal-orthorhombic ferroelastics. *Phys. Rev. B*, 63(9):094110, Jan 2001.

[32] K. R. Elder, M. Grant, N. Provatas, and J. M. Kosterlitz. Sharp Interface Limits of Phase-Field Models. *APS Meeting Abstracts*, page 25010, March 2000.

[33] G. Fix. *Research notes in mathematics, Pitman, New York, 1983*.

[34] M. E. Glicksman, J. D. Ayers, and R. J. Schaefer. Dendritic Growth—A Test of Theory. *Met. Trans. A*, page 1747, 1976.

[35] M. E. Glicksman and S. C. Huang. Boundary-layer analysis for the convection/diffusion transition in dendritic growth. *Advances in Space Research*, 1:25–35, 1981.

[36] I. S. Gradshteyn and I. M. Rhyzik. *Table of integrals, series, and products*. Academic Press, 1980.

[37] M. Humi and W. Miller. *2nd Course In ODE's For Scientists And Engineers*. New York: Springer, 1988.

[38] G.P. Ivantsov. *Dokl. Akad. Nauk USSR*, 58, 1947.

[39] K. A. Jackson and J. D. Hunt. Lamellar And Rod Eutectic Growth. *Trans. Metall. Soc. AIME*, 236:1129, 1966.

[40] K. Kassner and C. Misbah. Growth of lamellar eutectic structures: the axisymmetric state. *Phys. Rev. A*, (44), 1991.

[41] K. Kassner and C. Misbah. Spontaneous parity-breaking transition in directional growth of lamellar eutectic structures. *Phys. Rev. A*, 44(10):6533–6543, Nov 1991.

[42] O. D. Kellog. *Foundations of potential theory*. Springer Berlin, 1929.

[43] D. Kessler and H. Levine. *Acta Metall.*, 36:2693, 1988.

[44] D. A. Kessler, J. Koplik, and H. Levine. Geometrical models of interface evolution. III. Theory of dendritic growth. *Phys. Rev. A*, 31:1712–1717, March 1985.

[45] D. A. Kessler, J. Koplik, and H. Levine. Pattern selection in fingered growth phenomena. *Advances in physics*, (37):255–339, 1988.

[46] David A. Kessler, Joel Koplik, and Herbert Levine. Geometrical models of interface evolution. II. Numerical simulation. *Phys. Rev. A*, 30(6):3161–3174, Dec 1984.

[47] I.I. Kolodner. *Comm. Pure and Appl. Math.*, 9, 1956.

[48] M. D. Kruskal and H. Segur. Asymptotics beyond all orders. *Physica D Nonlinear Phenomena*, 28, September 1987.

[49] L. D. Landau and E. M. Lifshitz. *Theory of elasticity*. Oxford: Pergamon Press, 1987.

[50] J. Langer, G. Grinstein, and G. Mazenko. *Directions in condensed matter physics*. World Scientific, 1986.

[51] J. S. Langer. Studies in the theory of interfacial stability - II. Moving symmetric model. *Acta Metallurgica*, 25:1121–1137, 1977.

[52] J. S. Langer. Instabilities and pattern formation in crystal growth. *Rev. Mod. Phys.*, 52(1):1–28, Jan 1980.

[53] J. S. Langer and Turski L. A. Studies in the theory of interfacial stability - I. Stationary symmetric model. *Acta Metallurgica*, 25:1113–1119, 1977.

[54] J. S. Langer and H. Müller-Krumbhaar. Mode selection in a dendritelike nonlinear system. *Phys. Rev. A*, 27:499–514, January 1983.

[55] J.S. Langer. Lectures In The Theory Of Pattern Formation, Les Houches Summerschool. 1986.

[56] K. Malen. *Phys. Stat. Solidi B*, (44):661, 1971.

[57] D. I. Meiron. Selection of steady states in the two-dimensional symmetric model of dendritic growth. *Phys. Rev. A*, 33:2704–2715, April 1986.

[58] H. Müller-Krumbhaar and E. Brener. *Phase Transformations in Materials*. 2001.

[59] W. W. Mullins and R. F. Sekerka. Morphological stability of a particle growing by diffusion or heat flow. *J. of Appl. Phys.*, 34:323, 1963.

[60] W. W. Mullins and R. F. Sekerka. Stability of a planar interface during solidification of a dilute binary alloy. *J. of Appl. Phys.*, 35:444, 1964.

[61] N.I. Mushkelishvili. *Some Basic Problems of Mathematical Theory of Elasticity*. 1953.

[62] G.E. Nash. Capillarity-limited steady-state dendritic growth part one - theoretical development. *NRL Report*, 7679, 1974.

[63] B. Nestler, A.A. Wheeler, L. Ratke, and C. Stoecker. Phase-field model for solidification of a monotectic alloy with convection. *Physica D*, (141), 2000.

[64] B. et. al Nestler. Phase-field model for solidification of a monotectic alloy with convection. *Physica D*, 141:133–154, 2000.

[65] O.A. Oleinik. A method of solution of the general stefan problem. *Doklady Akademii Nauk SSSR*, (135), 1960.

[66] K. O'Neill. Boundary integral equation solution of moving boundary phase change problems. *International Journal for Numerical Methods in Engineering*, 19(12):1825–1850, 2005.

[67] V. L. Pokrovskii and I. M. Khalatnikov. On the problem of above-barrier reflection of high-energy particles. *JETP*, 13:12071210, 1961.

[68] J. Pollack. *Materials Science and Metallurgy*. 1988.

[69] D. A. Porter and K. E. Easterling. *Phase Transformations In Metals And Alloys*. 1992.

[70] I. A. Privorotskii. Contribution to the theory of domain structures in magnets and ferroelectrics. *JETP*, 33(4):1525–1536, 1970.

[71] L. Rubinstein. The Stefan problem. *AMS Transl. math. Monographs*, 27, 1971.

[72] S.C. Sarson and J.A. Charles. Monotectic systems. *Materials science and technology*, 1993.

[73] Birgit Schappel. Eine Randintegralmethode zur Lösung der Helmholtz-Gleichung in zweidimensionalen polygonal berandeten Gebieten. *Diploma Thesis, Universität Mainz*, 2000.

[74] R. Spatschek. *37th IFF Spring School - Computational Condensed Matter Physics*. 2006.

[75] R. Spatschek and M. Fleck. Influence of stress on interface kinetics. *Philosophical Magazine Letters*, 87:909–914, 2007.

[76] R. Spatschek, C. Mueller-Gugenberger, E. Brener, and B. Nestler. Phase field modeling of fracture and stress-induced phase transitions. *Phys. Rev. E*, 75(6, Part 2), 2007.

[77] J. Stefan. On the theory of ice formation, particularly ice formation in the Arctic ocean. *S-B Wien Akad.*, 98, 1889.

[78] J. Stefan. On the theory of formation of ice, particularly in the polar region. *Annalen der Physik und Chemie*, 1891.

[79] C. Stoecker and L. Ratke. A new 'Jackson-Hunt' model for monotectic composite growth. *Journal of Crystal Growth*, (203), 1999.

[80] D.E. Temkin. Growth of the needle-crystal formed in a supercooled melt. *Dokl. Akad. Nauk. SSSR*, 1960.

[81] M. van Dyke. Perturbation methods in fluid mechanics /Annotated edition. *NASA STI/Recon Technical Report A*, 75:46926, 1975.

[82] N. Wang and B. Wei. Phase separation and structural evolution of undercooled Fe-Sn monotectic alloy. *Materials Science and Engineering A*, (345), 2003.

[83] Y.H. Wen, Y. Wang, L.A. Bendersky, and Long-Qing Chen. Microstructural evolution during the [alpha]2 to [alpha]2+O transformation in Ti-Al-Nb alloys: phase-field simulation and experimental validation. *Acta Materialia*, 48(16):4125–4135, October 2000.

[84] Y.H. Wen, Y. Wang, and Long-Qing Chen. Effect of elastic interaction on the formation of a complex multi-domain microstructural pattern during a coherent hexagonal to orthorhombic transformation. *Acta Materialia*, 47(17):4375–4386, November 1999.

[85] Y.H. Wen, Y. Wang, and Long-Qing Chen. Phase-field simulation of domain structure evolution during a coherent hexagonal-to-orthorhombic transformation. *Philosophical Magazine A*, 80(9):1967–1982, January 2000.

[86] Y.H. Wen, Y. Wang, and Long-Qing Chen. Influence of an applied strain field on microstructural evolution during the [alpha]2 to O-phase transformation in Ti-Al-Nb system. *Acta Materialia*, 49(1):13–20, January 2001.

[87] S. C. Wilde and S. Langdon. Boundary element methods for acoustics. *Lecture notes, Department of Mathematics at Reading University*, 2007.

A Appendix

A.1 Basics about Green's Theorem and the Green's Function Method

Before we give the Green's identities here, we need to take into account that those require bounded domains. Since we operate on unbounded domains, there are additional constraints on the considered functions [42]. For

$$\int_V (u\nabla^2 v - \nabla u \nabla v) d^3x = \int_{\partial V} u(\nabla v)\vec{n} d f \tag{A.1}$$

and also for

$$\int_V (u\nabla^2 v - v\nabla^2 u) d^3x = \int_{\partial V} \left(u\frac{\partial v}{\partial n} - v\frac{\partial u}{\partial n} \right) d f, \tag{A.2}$$

one demands that ru, $r^2 \partial u/\partial x_i$, rv and $r^2 \partial v/\partial x_i$ are bounded in absolute value for all sufficiently large r, where r is a radius from any fixed point. In our concerned calculations, this problem is avoided by subtracting the boundary values of the corresponding fields.

The next important piece of basics for the Green's function method is the Lagrange identity:

$$v\mathcal{L}[u] - u\mathcal{L}^\dagger[v] = \nabla \vec{J}(u, v). \tag{A.3}$$

J is an expression in u, v with derivations of no higher order than $r - 1$, when r is the order of derivation in the linear differential operator $\mathcal{L}$.

Also note here that when in general non-selfadjoint operators are considered, it holds $\mathcal{L}g = -\delta(x - x')$ as function of x, and $\mathcal{L}^\dagger g = -\delta(x - x')$ as function of x', here g is the Green's function of $\mathcal{L}$.

We see immidiatly that the integration of the Lagrange identity of the operators of our interest in the corresponding domains is the first step towards a integral representation of each considered problem. If the considered system lacks volume inhomogeneties, the remainder $-u\mathcal{L}^\dagger[v] = \nabla \vec{J}(u, v)$ always leads to a boundary integral, reducing the dimension of the problem by one.

Another point we shall mention is the behaviour of the required integrals when the points of observation are exactly on the boundaries. Assuming that the respective integral may be taken, a prefactor $\phi/2\pi$ will enter in two-dimensional problems. Here, ϕ is the angle that measures the part of a circle which we can draw at the point of observation that is in the domain of definition. Consequently, when we are on the boundary of a smooth curve, this will be $\phi = \pi$ in two dimensions when we consider a model which is one-sided with respect to that point of observation. Analogue, this prefactor is trivially 1 in case of fully symmetric models, where only one domain of definition remains.

A.2 Derivation of the Integral Representations for the Monotectic System

Here we present the explicit calculations which lead to the 1-sided liquid-liquid model, subsections A.2.1 and A.2.2, and the 1-sided symmetric liquid-liquid model, subsection A.2.3.

A.2.1 Derivation of the Integral Representations for the Concentration Fields

For the closed representation of the problem, the formal elimination of the concentration fields by means of the Green's function technique is essential. We start here with the formal solution of the concentration fields by Green's identities.

We use the concentrations $\overline{c} = c - c_\infty$, where c_∞ denotes the concentration in each phase when we look at the asymptotic regime $y \to +\infty$, where the two liquid phases are in equilibrium. For phase L_1, we denote $c_\infty = c_{12}$, and phase L_1 has an asymptotic concentration as $c_\infty = c_{21}$. The usage of these concentrations is most comfortable for the subsequent calculations.

We point out that in the calculations presented here, we do not use mathematically positive oriented integrals, which would mean the enclosing curve is passed counterclockwise and the normal points out of the enclosed area, but the community - familiar sense of the contour, with a normal pointing into the enclosed phase. This yields a sign in front of the integral representation. The representation becomes more clearly arranged when we define the operator of the diffusion equation as

$$\mathcal{L}_{\vec{x}}[\overline{c}] = \nabla^2_{\vec{x}}\overline{c} + \frac{2}{l_D}\frac{\partial}{\partial y}\overline{c} = 0, \tag{A.4}$$

and the Green's function satisfies

$$\mathcal{L}_{\vec{x}}[g] = -\delta(\vec{r} - \vec{r}'), \tag{A.5}$$

$$\mathcal{L}^\dagger_{\vec{x}'}[g] = -\delta(\vec{r} - \vec{r}'). \tag{A.6}$$

The resulting representation can be organized as shown in the following calculation,

$$\overline{c}(\vec{x}) = \int_{V'(L1)} gL[\overline{c}] - \overline{c}L^\dagger[g]dV' \tag{A.7}$$

$$\overline{c}(\vec{x}) = \int_{V'(L1)} g\left(\nabla'^2\overline{c} + \frac{2}{l_D}\frac{\partial}{\partial y'}\overline{c}\right) - \overline{c}\left(\nabla'^2 g - \frac{2}{l_D}\frac{\partial}{\partial y'}g\right)dV' \tag{A.8}$$

$$\overline{c}(\vec{x}) = \int_{V'(L1)} g\nabla'^2\overline{c} - \overline{c}\nabla'^2 g + \frac{2}{l_D}\left(\nabla'(\vec{e}_y\overline{c}g)\right)dV' \tag{A.9}$$

$$\overline{c}(\vec{x}) = -\int_{\partial V'(L1)} (g\nabla'\overline{c} - \overline{c}\nabla' g)\vec{n}' + \frac{2}{l_D}\overline{c}g\vec{n}'\vec{e}_y dS'. \tag{A.10}$$

By Eqs. (A.7) we obtain the formal solution for the field $\overline{c}$. Next, we shall discuss which parts of the boundary contribute to the integral representation. The notation for each part of the relevant boundary is given in fig. A.1. The boundary Γ_{1t}, which is at $y \to \infty$, gives by $\overline{c}_{|\Gamma(1t)} = 0$ and $(\nabla\overline{c})_{|\Gamma(1t)} = 0$ zero contribution to the integral. When we consider the contribution along the

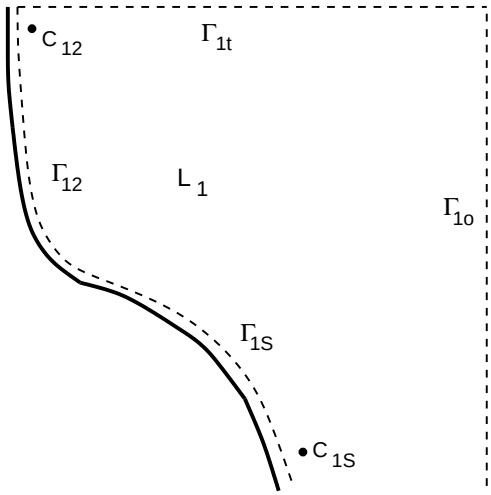

Figure A.1: A sketch of the boundary of phase L_1. The triple junction is located at $(0, 0)$.

boundary Γ_{1o}, we remember that the Green's function tends to zero for distances $\|\vec{r} - \vec{r}'\| \to \infty$, we also skip these integrals. Thus, the formal solution in phase 1, for a point of observation not on the boundary, is

$$\begin{aligned} \bar{c}(\vec{x}) &= -\int d\Gamma'_{12}\left[g\nabla'\bar{c}_{\Gamma'_{12}} - \bar{c}_{\Gamma'_{12}}\nabla g + \frac{2}{l_D}\bar{c}_{\Gamma'_{12}} g\vec{e}_y\right]\vec{n}' \\ &- \int d\Gamma'_{1S}\left[g\nabla'\bar{c}_{\Gamma'_{1S}} - \bar{c}_{\Gamma'_{1S}}\nabla g + \frac{2}{l_D}\bar{c}_{\Gamma'_{1S}} g\vec{e}_y\right]\vec{n}' \end{aligned} \tag{A.11}$$

Analogue we write for $\bar{c}$ in the liquid phase L_2:

$$\bar{c}(\vec{x}) = -\int_{\partial V'(L2)} (g\nabla'\bar{c} - \bar{c}\nabla' g)\vec{n} + \frac{2}{l_D}\bar{c}g\vec{n}'\vec{e}_y, \tag{A.12}$$

the notation for each part of the relevant boundary as well is given in fig. A.2.

As we can again skip the integrals belonging to the boundary Γ_{2o} and at $y \to \infty$, we write down the resulting integral representation of the concentration field in phase L_2:

$$\begin{aligned} \bar{c}(\vec{x}) &= -\int d\Gamma'_{21}\left[g\nabla'\bar{c}_{\Gamma'_{21}} - \bar{c}_{\Gamma'_{21}}\nabla' g + \frac{2}{l_D}\bar{c}_{\Gamma'_{21}} g\vec{e}_y\right]\vec{n} \\ &- \int d\Gamma'_{2S}\left[g\nabla'\bar{c}_{\Gamma'_{2S}} - \bar{c}_{\Gamma'_{2S}}\nabla' g + \frac{2}{l_D}\bar{c}_{\Gamma'_{2S}} g\vec{e}_y\right]\vec{n}' \end{aligned} \tag{A.13}$$

With properly defined formal representations and domains of the concentration fields, we can calculate the resulting system of governing equations in all detail. We stress again that we conduct this lengthy calculation as this is the first occasion where we apply a 1-sided model, and the introduction in section 2.4 only discusses symmetric two-sided models.

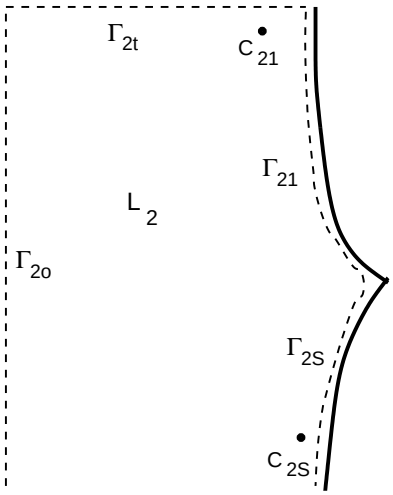

Figure A.2: A sketch of the boundary of phase L_2.

A.2.2 Explicit Boundary Integral Formulation

We stress that this paragraph is dedicated to the detailed calculation of the closed representation for the liquid-liquid 1-sided model. By liquid-liquid 1-sided model we label the system which neglects diffusion in the solid phase and takes into account diffusion in both liquid phases, which are treated formally independent. As we have not yet discussed the derivation of the resulting integral equations for a 1-sided case, these exhaustively detailed description shall especially serve as basis to get familiar with the Green's function method in a more general approach.

The outcome of this paragraph is summarized in 'Closed representation of the one-sided model'. When we compare the representation we obtain in the subsequent calculations to those we get within the so-called symmetric model, see section 2.4, this shows the great advantages of the latter. We start from dimensional concentration fields, which we just introduced as

$$\bar{c} = c - c_{21}$$

in the left liquid phase L_2, and

$$\bar{c} = c - c_{12}$$

in the liquid phase L_1, and also label the miscibility gaps as

$$\begin{aligned} \Delta c_{2S} &= c_{2S} - c_{S2} \\ \Delta c_{1S} &= c_{1S} - c_{S1} \\ \Delta c_{21} &= c_{21} - c_{12}. \end{aligned} \tag{A.14}$$

The local equilibria read as

$$\begin{aligned}
\Gamma_{12}: \bar{c} &= -\frac{\gamma_{12}T_m}{m_{12}L_{21}}\kappa \\
\Gamma_{1S}: \bar{c} &= (c_{1S}-c_{12}) - \frac{\gamma_{1S}T_m}{m_{12}L_{21}}\kappa \\
\Gamma_{21}: \bar{c} &= -\frac{\gamma_{12}T_m}{m_{21}L_{21}}\kappa \\
\Gamma_{2S}: \bar{c} &= (c_{2S}-c_{21}) - \frac{\gamma_{2S}T_m}{m_{2S}L_{2S}}\kappa,
\end{aligned} \tag{A.15}$$

where we again give the quantities involved - the absolute slope of the coexistence lines in the phase diagram, $m_{ij} = \|dT/dc_{ij}\|$, the effective latent heats L_{ij} and the surface energy densities γ_{ij}. Concerning the definition of the effective latent heats, we refer to [40]. The moving boundary condition is given by the mass conservation, where we can exchange $\bar{c}$ and c.

$$\begin{aligned}
\Gamma_{21}: \upsilon_n(c_{21}-c_{12}) &= -D\left(\nabla c_{|\Gamma_{21}} - \nabla c_{|\Gamma_{12}}\right)\vec{n} \\
\Gamma_{2S}: \upsilon_n(c_{2S}-c_{S2}) &= -D\left(\nabla c_{|\Gamma_{2S}}\right)\vec{n} \\
\Gamma_{1S}: \upsilon_n(c_{1S}-c_{S1}) &= -D\left(\nabla c_{|\Gamma_{1S}}\right)\vec{n}
\end{aligned} \tag{A.16}$$

When we write down the representation of the concentration field $\bar{c}$ on the interface, we have to take into account that we get a prefactor $1/2$ as explained in [73]. Thus we obtain, referring to Eq. (A.13)

$$\begin{aligned}
&\tfrac{1}{2}\ \bar{c}_{\Gamma(i)} \\
&= -\int_{\Gamma'(iS)}\left[g(\nabla'\bar{c})_{\Gamma'(iS)} - \bar{c}_{\Gamma'(iS)}\nabla' g + \frac{2}{l_D}\vec{e}_y\bar{c}_{\Gamma'(iS)}g\right]\vec{n}'_{iS}\,ds' \\
&- \int_{\Gamma'(ij)}\left[g(\nabla'\bar{c})_{\Gamma'(ij)} - \bar{c}_{\Gamma'(ij)}\nabla' g + \frac{2}{l_D}\vec{e}_y\bar{c}_{\Gamma'(ij)}g\right]\vec{n}'_{ij}ds',
\end{aligned} \tag{A.17}$$

where $i,j = 1,2$ and $\vec{n}_{ij} = -\vec{n}_{ji}$. Now we insert the known values of the considered fields. Since we separately define the integral representations for both liquid phases, we cannot eliminate both normal projections of the gradients of the concentrations by mass conservation, Eq. (A.16). We choose $(\nabla\bar{c})_{\Gamma(21)}\vec{n}$ from both normal projections of the gradients as remaining unknown here, leading to the following expressions. In phase L_1, we obtain

$$\begin{aligned}
&\tfrac{1}{2}\ \bar{c}_{\Gamma(1)} \\
&= -\int_{\Gamma'(1S)} g\left(\frac{-\upsilon_{n'}}{D}\Delta c_{1S}\right) - \left((c_{1S}-c_{12}) - \frac{\gamma_{1S}T_m}{m_{1S}L_{1S}}\kappa'\right)\left[\nabla' g - \frac{2}{l_D}\vec{e}_y g\right]\vec{n}'\,ds' \\
&- \int_{\Gamma'(12)} g\left(\frac{\upsilon_{n'}}{D}\Delta c_{21} + \nabla'\bar{c}_{\Gamma'(21)}\vec{n}'\right) - \left(-\frac{\gamma_{12}T_m}{m_{12}L_{21}}\kappa'\right)\left[\nabla' g - \frac{2}{l_D}\vec{e}_y g\right]\vec{n}'\,ds'.
\end{aligned} \tag{A.18}$$

and analogue in phase L_2

$$\begin{aligned}
&\tfrac{1}{2} \quad \overline{c}_{\Gamma(2)} \\
&= \quad -\int_{\Gamma'(2S)} g\left(\frac{-\upsilon_{n'}}{D}\Delta c_{2S}\right) - \left((c_{2S} - c_{21}) - \frac{\gamma_{2S} T_m}{m_{2S} L_{2S}}\kappa'\right)\left[\nabla' g - \frac{2}{l_D}\vec{e}_y g\right]\vec{n}' ds' \\
&- \quad \int_{\Gamma'(21)} g(\nabla'\overline{c})_{\Gamma(21)}\vec{n}' - \left(-\frac{\gamma_{12} T_m}{m_{21} L_{21}}\kappa'\right)\left[\nabla' g - \frac{2}{l_D}\vec{e}_y g\right]\vec{n}' ds'.
\end{aligned} \tag{A.19}$$

We introduce dimensionless coordiantes, $x \to xR_1, y \to yR_1$, the normalized concentrations $c = (c - c_{21})/(\Delta c_{2S})$, $c = (c - c_{12})/(\Delta c_{1S})$ for phase L_2 and L_1, the Peclet number $p_1 = R_1\upsilon/2D$ and the supersaturation on Γ_{2S} is $\Delta_2 = (c_{2S} - c_{21})/\Delta c_{2S}$, on Γ_{1S} we label it as $\Delta_1 = (c_{1S} - c_{12})/\Delta c_{1S}$. By κ' we denote $\kappa(x')$, and the capillarity lengths here are defined as

$$\begin{aligned}
d_{12} &= \frac{\gamma_{12} T_m}{\Delta c_{21} L_{12} m_{12}}, \\
d_{21} &= \frac{\gamma_{12} T_m}{\Delta c_{21} L_{12} m_{21}}, \\
d_{1S} &= \frac{\gamma_{1S} T_m}{\Delta c_{1S} L_{1S} m_{1S}}, \\
d_{2S} &= \frac{\gamma_{2S} T_m}{\Delta c_{2S} L_{2S} m_{2S}}.
\end{aligned} \tag{A.20}$$

The explicit writing of $(\nabla' g)$ is

$$\nabla g' = \frac{1}{2\pi l_D}\, e^{-(y-y')/l_D}\left[K_0\left(\frac{\|\vec{r} - \vec{r}'\|}{l_D}\right)\vec{e}_y + \frac{(\vec{r} - \vec{r}')}{\|\vec{r} - \vec{r}'\|}K_1\left(\frac{\|\vec{r} - \vec{r}'\|}{l_D}\right)\right],$$

where $K_{0,1}$ denotes the modififed Bessel function of zeroth or first order, respectively. The resulting representation for the concentration in phase L_2 on the interfaces Γ_{21} and Γ_{2S} reads as

$$\begin{aligned}
&\tfrac{1}{2} \quad c_{\Gamma(2)} \\
&= \quad \frac{p_1}{2\pi}\int_{-\infty}^{0} dx' e^{-p_1(y-y')}\Bigg(2K_0(p_1\eta) \\
&+ \quad \frac{ds}{dx'}\vec{n}'\left(\Delta_2 - \frac{d_{2S}}{R_1}\kappa'\right)\left[\frac{(\vec{r} - \vec{r'})}{\eta}K_1(p_1\eta) - K_0(p_1\eta)\vec{e}_y\right]\Bigg) \\
&- \quad \frac{1}{2\pi}\int_{-a/R_1}^{0} dx' \frac{ds}{dx'} e^{-p_1(y-y')}\Bigg(K_0(p_1\eta)(\nabla c)_{\Gamma(21)}\vec{n}' \\
&- \quad p_1\frac{\Delta c_{21}}{\Delta c_{2S}}\left(-\frac{d_{21}}{R_1}\kappa'\right)\left[\frac{(\vec{r} - \vec{r'})}{\eta}K_1(p_1\eta) - K_0(p_1\eta)\vec{e}_y\right]\vec{n}'\Bigg),
\end{aligned} \tag{A.21}$$

here we define $\eta = \|\vec{r} - \vec{r}'\|$, by a we label the asymptotic lateral shift of the $L_1 - L_2$-interface as illustrated in fig. 4.11.Correspondingly, in phase L_1, we express the concentration on the interfaces

Γ_{12} and Γ_{1S} as

$$\begin{aligned}
&\tfrac{1}{2} \quad c_{\Gamma(1)} \qquad\qquad (A.22)\\
&= \quad \frac{p_1}{2\pi}\int_0^\infty dx' e^{-p_1(y-y')}\Bigg(2K_0(p_1\eta)\\
&+ \quad \left(\Delta_1 - \frac{d_{1S}}{R_1}\kappa'\right)\left[\frac{-\frac{dy}{dx'}(x-x')+(y-y')}{\eta}K_1(p_1\eta) - K_0(p_1\eta)\right]\Bigg)\\
&+ \quad \frac{p_1}{2\pi}\int_{-a/R_1}^0 dx' e^{-p_1(y-y')}\left(\frac{ds}{dx'}K_0(p_1\eta)\left(2\frac{(c_{21}-c_{12})}{\Delta c_{1S}} + \frac{\nabla' c_{\Gamma(21)}\vec{n}'}{p_1}\right)\right.\\
&- \quad \left.\frac{\Delta c_{21}}{\Delta c_{1S}}\left(-\frac{d_{12}}{R_1}\kappa'\right)\left[\frac{(\vec{r}-\vec{r'})}{\eta}K_1(p_1\eta) - K_0(p_1\eta)\vec{e}_y\right]\vec{n}'\right),
\end{aligned}$$

With some useful substitutions, namely

$$\begin{aligned}
\vec{n}'\vec{e}_y ds' &= dx'\\
\frac{(\vec{r}-\vec{r'})}{\eta}\vec{n}' ds' &= \frac{-\frac{dy}{dx'}(x-x')+(y-y')}{\eta}dx',
\end{aligned}$$

we achieve the final representation of the concentration c on the interfaces Γ_{21} and Γ_{2S} as

$$\begin{aligned}
&\tfrac{1}{2} \quad c_{\Gamma(2)} \qquad\qquad (A.23)\\
&= \quad \frac{p_1}{2\pi}\int_{-\infty}^0 dx' e^{-p_1(y-y')}\Bigg(2K_0(p_1\eta)\\
&+ \quad \left(\Delta_2 - \frac{d_{2S}}{R_1}\kappa'\right)\left[\frac{-\frac{dy}{dx'}(x-x')+(y-y')}{\eta}K_1(p_1\eta) - K_0(p_1\eta)\right]\Bigg)\\
&- \quad \frac{1}{2\pi}\int_{-a/R_1}^0 dx' e^{-p_1(y-y')}\left(\frac{ds}{dx'}K_0(p_1\eta)(\nabla' c)_{\Gamma(21)}\vec{n}'\right.\\
&- \quad \left.p_1\frac{\Delta c_{21}}{\Delta c_{2S}}\left(-\frac{d_{21}}{R_1}\kappa'\right)\left[\frac{-\frac{dy}{dx'}(x-x')+(y-y')}{\eta}K_1(p_1\eta) - K_0(p_1\eta)\right]\right).
\end{aligned}$$

and for Γ_{12} and Γ_{1S} we obtain

$$\begin{aligned}
&\tfrac{1}{2} \quad c_{\Gamma(1)} \qquad (A.24)\\
&= \quad \frac{p_1}{2\pi}\int_0^\infty dx' e^{-p_1(y-y')}\Bigg(2K_0(p_1\eta)\\
&+ \quad \left(\Delta_1 - \frac{d_{1S}}{R_1}\kappa'\right)\left[\frac{-\frac{dy}{dx'}(x-x')+(y-y')}{\eta}K_1(p_1\eta) - K_0(p_1\eta)\right]\Bigg)\\
&+ \quad \frac{p_1}{2\pi}\int_{-a/R_1}^0 dx' e^{-p_1(y-y')}\left(\frac{ds}{dx'}K_0(p_1\eta)\left(2\frac{(c_{21}-c_{12})}{\Delta c_{1S}} + \frac{\nabla' c_{\Gamma(21)}\vec{n}'}{p_1}\right)\right.\\
&+ \quad \left.\frac{\Delta c_{21}}{\Delta c_{1S}}\left(-\frac{d_{12}}{R_1}\kappa'\right)\left[\frac{-\frac{dy}{dx'}(x-x')+(y-y')}{\eta}K_1(p_1\eta) - K_0(p_1\eta)\right]\right),
\end{aligned}$$

Equations (A.23) and (A.24) state the representations of the concentration fields on the interfaces. They let us eliminate the concentrations in the local equilibria in the corresponding interfaces and thus lead to the necessitated interface equations. We express the local equilibria on these interfaces in dimensionless notation as

$$\begin{aligned}
\Gamma_{21}: \; c &= -\frac{\Delta c_{21}}{\Delta c_{2S}}\frac{d_{21}}{R_1}\kappa, \qquad (A.25)\\
\Gamma_{2S}: \; c &= \Delta_2 - \frac{d_{2S}}{R_1}\kappa,\\
\Gamma_{12}: \; c &= -\frac{\Delta c_{21}}{\Delta c_{1S}}\frac{d_{12}}{R_1}\kappa,\\
\Gamma_{1S}: \; c &= \Delta_1 - \frac{d_{1S}}{R_1}\kappa,
\end{aligned}$$

where the prefactor $\Delta c_{21}/\Delta c_{iS}$, $i = 1, 2$, comes from normalizing the local equilibria in the liquid phases L_2 by Δc_{2S} and in L_1 by Δc_{1S}. Consequently, for the interface equations for $y(x)$ we yield on Γ_{21}

$$\begin{aligned}
&- \quad \frac{\Delta c_{21}}{\Delta c_{2S}}\frac{d_{21}}{2R_1}\kappa \qquad (A.26)\\
&= \quad \frac{p_1}{2\pi}\int_{-\infty}^0 dx' e^{-p_1(y-y')}\Bigg(2K_0(p_1\eta)\\
&+ \quad \left(\Delta_2 - \frac{d_{2S}}{R_1}\kappa'\right)\left[\frac{-\frac{dy}{dx'}(x-x')+(y-y')}{\eta}K_1(p_1\eta) - K_0(p_1\eta)\right]\Bigg)\\
&- \quad \frac{1}{2\pi}\int_{-a/R_1}^0 dx' e^{-p_1(y-y')}\frac{ds}{dx'}\Bigg(K_0(p_1\eta)(\nabla' c)_{\Gamma(21)}\vec{n}'\\
&- \quad p_1\frac{\Delta c_{21}}{\Delta c_{2S}}\left(-\frac{d_{21}}{R_1}\kappa'\right)\left[\frac{-\frac{dy}{dx'}(x-x')+(y-y')}{\eta}K_1(p_1\eta) - K_0(p_1\eta)\right]\Bigg),
\end{aligned}$$

and on Γ_{2S} we have

$$\begin{aligned}
&\frac{1}{2}\quad\left(\Delta_2-\frac{d_{2S}}{R_1}\kappa\right) \qquad\qquad (A.27)\\
&=\quad\frac{p_1}{2\pi}\int_{-\infty}^{0}dx'e^{-p_1(y-y')}\Bigg(2K_0(p_1\eta)\\
&+\quad\left(\Delta_2-\frac{d_{2S}}{R_1}\kappa'\right)\left[\frac{-\frac{dy}{dx'}(x-x')+(y-y')}{\eta}K_1(p_1\eta)-K_0(p_1\eta)\right]\Bigg)\\
&-\quad\frac{1}{2\pi}\int_{-a/R_1}^{0}dx'e^{-p_1(y-y')}\frac{ds}{dx'}\Bigg(K_0(p_1\eta)(\nabla' c)_{\Gamma(21)}\vec{n}'\\
&-\quad p_1\frac{\Delta c_{21}}{\Delta c_{2S}}\left(-\frac{d_{21}}{R_1}\kappa'\right)\left[\frac{-\frac{dy}{dx'}(x-x')+(y-y')}{\eta}K_1(p_1\eta)-K_0(p_1\eta)\right]\Bigg).
\end{aligned}$$

For phase L_1, the interface equations are

$$\begin{aligned}
&-\quad\frac{\Delta c_{21}}{\Delta c_{1S}}\frac{d_{12}}{2R_1}\kappa \qquad\qquad (A.28)\\
&=\quad\frac{p_1}{2\pi}\int_{0}^{\infty}dx'e^{-p_1(y-y')}\Bigg(2K_0(p_1\eta)\\
&+\quad\left(\Delta_1-\frac{d_{1S}}{R_1}\kappa'\right)\left[\frac{-\frac{dy}{dx'}(x-x')+(y-y')}{\eta}K_1(p_1\eta)-K_0(p_1\eta)\right]\Bigg)\\
&+\quad\frac{p_1}{2\pi}\int_{-a/R_1}^{0}dx'e^{-p_1(y-y')}\Bigg(\frac{ds}{dx'}K_0(p_1\eta)\left(2\frac{(c_{21}-c_{12})}{\Delta c_{1S}}+\frac{\nabla c_{\Gamma(21)}\vec{n}'}{p_1}\right)\\
&+\quad\frac{\Delta c_{21}}{\Delta c_{1S}}\left(-\frac{d_{12}}{R_1}\kappa'\right)\left[\frac{-\frac{dy}{dx'}(x-x')+(y-y')}{\eta}K_1(p_1\eta)-K_0(p_1\eta)\right]\Bigg)
\end{aligned}$$

on Γ_{12} and, for Γ_{1S}

$$\begin{aligned}
&\frac{1}{2}\quad\left(\Delta_1-\frac{d_{1S}}{R_1}\kappa\right) \qquad\qquad (A.29)\\
&=\quad\frac{p_1}{2\pi}\int_{0}^{\infty}dx'e^{-p_1(y-y')}\Bigg(2K_0(p_1\eta)\\
&+\quad\left(\Delta_1-\frac{d_{1S}}{R_1}\kappa'\right)\left[\frac{-\frac{dy}{dx'}(x-x')+(y-y')}{\eta}K_1(p_1\eta)-K_0(p_1\eta)\right]\Bigg)\\
&+\quad\frac{p_1}{2\pi}\int_{-a/R_1}^{0}dx'e^{-p_1(y-y')}\Bigg(\frac{ds}{dx'}K_0(p_1\eta)\left(2\frac{(c_{21}-c_{12})}{\Delta c_{1S}}+\frac{\nabla c_{\Gamma(21)}\vec{n}'}{p_1}\right)\\
&+\quad\frac{\Delta c_{21}}{\Delta c_{1S}}\left(-\frac{d_{12}}{R_1}\kappa'\right)\left[\frac{-\frac{dy}{dx'}(x-x')+(y-y')}{\eta}K_1(p_1\eta)-K_0(p_1\eta)\right]\Bigg)
\end{aligned}$$

The equations (A.26),(A.27),(A.28) and (A.29) state the complete problem we consider.

A.2.3 The Derivation of the One-Sided Liquid-Liquid Symmetric Model

We recall, see e.g. [66], [73] or [87] , that

$$\begin{aligned}
\bar{c}_1(\vec{x}) &= -\int_{\partial V'1} ds' \left(G\nabla'\bar{c}_1 - \bar{c}_1\nabla' G + \frac{2}{l_D}\bar{c}_1 G\vec{e}_y \right)\vec{n}' \quad | \quad \vec{x} \in V1 \\
\frac{1}{2}\cdot\bar{c}_1(\vec{x}) &= -\int_{\partial V'1} ds' \left(G\nabla'\bar{c}_1 - \bar{c}_1\nabla' G + \frac{2}{l_D}\bar{c}_1 G\vec{e}_y \right)\vec{n}' \quad | \quad \vec{x} \in \partial V1 \\
0\cdot\bar{c}_1(\vec{x}) &= -\int_{\partial V'1} ds' \left(G\nabla'\bar{c}_1 - \bar{c}_1\nabla' G + \frac{2}{l_D}\bar{c}_1 G\vec{e}_y \right)\vec{n}' \quad | \quad \vec{x} \in R^2_{\setminus\bar{V}1}
\end{aligned} \tag{A.30}$$

$$\begin{aligned}
\bar{c}_2(\vec{x}) &= -\int_{\partial V'2} ds' \left(G\nabla'\bar{c}_2 - \bar{c}_2\nabla' G + \frac{2}{l_D}\bar{c}_2 G\vec{e}_y \right)\vec{n}' \quad | \quad \vec{x} \in V2 \\
\frac{1}{2}\cdot\bar{c}_2(\vec{x}) &= -\int_{\partial V'2} ds' \left(G\nabla'\bar{c}_2 - \bar{c}_2\nabla' G + \frac{2}{l_D}\bar{c}_2 G\vec{e}_y \right)\vec{n}' \quad | \quad \vec{x} \in \partial V2 \\
0\cdot\bar{c}_2(\vec{x}) &= -\int_{\partial V'2} ds' \left(G\nabla'\bar{c}_2 - \bar{c}_2\nabla' G + \frac{2}{l_D}\bar{c}_2 G\vec{e}_y \right)\vec{n}' \quad | \quad \vec{x} \in R^2_{\setminus\bar{V}2},
\end{aligned} \tag{A.31}$$

where we defined $\bar{c}_i = c(L_i) - c(L_i, y \to \infty)$, $\bar{V}$ is the union of V and its boundary ∂V, and the orientation of the line integral is counterclockwise with the normal pointing into the considered area. The volume indices here correspond to the indices of the liquid phases, i.e. $V1$ is the domain of liquid phase L_1, and the entire boundary of liquid phase L_1 is denoted by $\partial V1$. In the light of the symmetries which apply here to the two liquid phases, the merging of the domains of definition by means of simply adding the field representations leads to the 1-sided liquid-liquid symmetric model:

$$\begin{aligned}
(\bar{c}_1 + 0\cdot\bar{c}_2)(\vec{x}) &= -\int_{\partial V'1} ds' \left(G\nabla'\bar{c}_1 - \bar{c}_1\nabla' G + \frac{2}{l_D}\bar{c}_1 G\vec{e}_y \right)\vec{n}' \\
&- \int_{\partial V'2} ds' \left(G\nabla'\bar{c}_2 - \bar{c}_2\nabla' G + \frac{2}{l_D}\bar{c}_2 G\vec{e}_y \right)\vec{n}' \quad | \quad \vec{x} \in V1
\end{aligned} \tag{A.32}$$

$$\begin{aligned}
\left(\frac{1}{2}\bar{c}_1 + \frac{1}{2}\bar{c}_2\right)(\vec{x}) &= -\int_{\partial V'1} ds' \left(G\nabla'\bar{c}_1 - \bar{c}_1\nabla' G + \frac{2}{l_D}\bar{c}_1 G\vec{e}_y \right)\vec{n}' \\
&- \int_{\partial V'2} ds' \left(G\nabla'\bar{c}_2 - \bar{c}_2\nabla' G + \frac{2}{l_D}\bar{c}_2 G\vec{e}_y \right)\vec{n}' \quad | \quad \vec{x} \in \partial V1 \cap \partial V2
\end{aligned} \tag{A.33}$$

$$\begin{aligned}
\left(0\cdot\bar{c}_1 + \frac{1}{2}\bar{c}_2\right)(\vec{x}) &= -\int_{\partial V'1} ds' \left(G\nabla'\bar{c}_1 - \bar{c}_1\nabla' G + \frac{2}{l_D}\bar{c}_1 G\vec{e}_y \right)\vec{n}' \\
&- \int_{\partial V'2} ds' \left(G\nabla'\bar{c}_2 - \bar{c}_2\nabla' G + \frac{2}{l_D}\bar{c}_2 G\vec{e}_y \right)\vec{n}' \quad | \quad \vec{x} \in \partial V2_{\setminus\partial V1}
\end{aligned} \tag{A.34}$$

$$\left(\frac{1}{2}\bar{c}_1 + 0\cdot\bar{c}_2\right)(\vec{x}) = -\int_{\partial V'1} ds'\left(G\nabla'\bar{c}_1 - \bar{c}_1\nabla'G + \frac{2}{l_D}\bar{c}_1 G\vec{e}_y\right)\vec{n}' - \int_{\partial V'2} ds'\left(G\nabla'\bar{c}_2 - \bar{c}_2\nabla'G + \frac{2}{l_D}\bar{c}_2 G\vec{e}_y\right)\vec{n}' \quad | \quad \vec{x}\in\partial V1_{\setminus\partial V2} \tag{A.35}$$

$$(0\cdot\bar{c}_1 + \bar{c}_2)(\vec{x}) = -\int_{\partial V'1} ds'\left(G\nabla'\bar{c}_1 - \bar{c}_1\nabla'G + \frac{2}{l_D}\bar{c}_1 G\vec{e}_y\right)\vec{n}' - \int_{\partial V'2} ds'\left(G\nabla'\bar{c}_2 - \bar{c}_2\nabla'G + \frac{2}{l_D}\bar{c}_2 G\vec{e}_y\right)\vec{n}' \quad | \quad \vec{x}\in V2 \tag{A.36}$$

A.3 Expression of $\delta\tilde{F}^{el}$ in Terms of the Strains in the Initial Phase

This part of the appendix is dedicated to the tedious calculation which yields the representation of the elastic contribution of the difference of the modified free energies at the phase interface. The necessitated expression only depends on the lattice-strain induced stresses σ^{ϵ}_{ik} and the strains in the reference phase α, $u^{(\alpha)}_{ik}$.

We start with the explicit notation of $\delta\tilde{F}^{el} = \tilde{F}_{(\alpha)} - \tilde{F}_{(\beta)}$,

$$\delta\tilde{F}^{el} = \tilde{F}_{(\alpha)} - \tilde{F}_{(\beta)} = \left[0.5\sigma^{(\alpha)}_{ik}u^{(\alpha)}_{ik} - \sigma^{(\alpha)}_{nn}u^{(\alpha)}_{nn} - 2\sigma^{(\alpha)}_{n\tau}u^{(\alpha)}_{n\tau}\right] - \left[0.5\sigma^{(\beta)}_{ik}(u^{(\beta)}_{ik} - \epsilon_{ik}) - \sigma^{(\beta)}_{nn}u^{(\beta)}_{nn} - 2\sigma^{(\beta)}_{n\tau}u^{(\beta)}_{n\tau}\right]$$

. We give the intermediate steps, beginning with the elimination of $u_{\tau\tau}$ by means of the coherency condition,

$$u^{(\alpha)}_{\tau\tau} = u^{(\beta)}_{\tau\tau} = u_{\tau\tau},$$

which yields

$$\tilde{F}_\alpha - \tilde{F}_\beta = -0.5\sigma^{(\alpha)}_{nn}u^{(\alpha)}_{nn} - \sigma^{(\alpha)}_{n\tau}u^{(\alpha)}_{n\tau} + 0.5\sigma^{(\alpha)}_{\tau\tau}u_{\tau\tau} + 0.5\sigma^{(\beta)}_{nn}u^{(\beta)}_{nn} + \sigma^{(\beta)}_{n\tau}u^{(\beta)}_{n\tau} - 0.5\sigma^{(\beta)}_{\tau\tau}u_{\tau\tau} + 0.5\sigma^{(\beta)}_{zz}\epsilon_{zz} + 0.5\sigma^{(\beta)}_{nn}\epsilon_{nn} + \sigma^{(\beta)}_{n\tau}\epsilon_{n\tau} + 0.5\sigma^{(\beta)}_{\tau\tau}\epsilon_{\tau\tau}, \tag{A.37}$$

and also using that

$$\sigma^{(\alpha)}_{ni} = \sigma^{(\beta)}_{ni} = \sigma_{ni},$$

we obtain

$$\tilde{F}_\alpha - \tilde{F}_\beta = 0.5\left(\sigma^{(\beta)}_{ik}\epsilon_{ik}\right) + 0.5\left(\sigma_{nn}(u^{(\beta)}_{nn} - u^{(\alpha)}_{nn}) + 2\sigma_{n\tau}(u^{(\beta)}_{n\tau} - u^{(\alpha)}_{n\tau}) + (\sigma^{(\alpha)}_{\tau\tau} - \sigma^{(\beta)}_{\tau\tau})u_{\tau\tau}\right). \tag{A.38}$$

The jump of the strains at the interface, specifically

$$u^{(\beta)}_{nn} - u^{(\alpha)}_{nn} = \epsilon_{nn} + \frac{\nu}{1-\nu}(\epsilon_{\tau\tau} + \epsilon_{zz})$$

and

$$u^{(\beta)}_{n\tau} - u^{(\alpha)}_{n\tau} = \epsilon_{n\tau},$$

lead to

$$\tilde{F}_\alpha - \tilde{F}_\beta = \sigma_{nn}\epsilon_{nn} + 2\sigma_{n\tau}\epsilon_{n\tau} + 0.5(\sigma^{(\beta)}_{\tau\tau}\epsilon_{\tau\tau} + \sigma^{(\beta)}_{zz}\epsilon_{zz} + \sigma_{nn}\left(\frac{\nu}{1-\nu}(\epsilon_{\tau\tau}+\epsilon_{zz})\right) + (\sigma^{(\alpha)}_{\tau\tau} - \sigma^{(\beta)}_{\tau\tau})u_{\tau\tau}). \tag{A.39}$$

Here we use the jump condition of the stresses at the interface, namely

$$\sigma^{(\beta)}_{\tau\tau} = \sigma^{(\alpha)}_{\tau\tau} - \frac{E}{1-\nu^2}(\epsilon_{\tau\tau} + \nu\epsilon_{zz}), \tag{A.40}$$

to express the stress σ^{ϵ}_{ik} after some intermediate calculations,

$$\sigma^{(\beta)}_{zz} = \frac{E}{(1+\nu)(1-2\nu)}\left((1-\nu) - \epsilon_{zz} + \nu((u^{(\beta)}_{nn} - \epsilon_{nn}) + (u_{\tau\tau} - \epsilon_{\tau\tau}))\right) \tag{A.41}$$

$$\sigma^{(\beta)}_{zz} = \frac{E}{(1+\nu)(1-2\nu)} + \left(-(1-\nu)\epsilon_{zz} + \nu\left(u^{(\alpha)}_{nn} + \frac{\nu}{1-\nu}(\epsilon_{\tau\tau}+\epsilon_{zz}) + u_{\tau\tau} - \epsilon_{\tau\tau}\right)\right) \tag{A.42}$$

$$\sigma^{(\beta)}_{zz} = \frac{E}{(1+\nu)(1-2\nu)}\left(\nu(u^{(\alpha)}_{nn} + u_{\tau\tau})\right) \quad \left(= \sigma^{(\alpha)}_{zz}\right) \tag{A.43}$$

$$+\frac{E}{(1+\nu)(1-2\nu)}\left(-(1-\nu)\epsilon_{zz} + \nu(\frac{\nu}{1-\nu}(\epsilon_{\tau\tau}+\epsilon_{zz}) - \epsilon_{\tau\tau})\right),$$

as

$$\sigma^{(\beta)}_{zz} = \sigma^{(\alpha)}_{zz} + \frac{E}{(1+\nu)(1-2\nu)}\left(-(1-\nu)\epsilon_{zz} + \nu(\frac{\nu}{1-\nu}(\epsilon_{\tau\tau}+\epsilon_{zz}) - \epsilon_{\tau\tau})\right). \tag{A.44}$$

Up to here, we obtained a representation of $\delta\tilde{F}^{el}$ independent of $u^{(\beta)}_{ik}$ and $\sigma^{(\beta)}_{ik}$, which reads as

$$\begin{aligned}\tilde{F}_\alpha - \tilde{F}_\beta = \quad & \sigma_{nn}\epsilon_{nn} + 2\sigma_{n\tau}\epsilon_{n\tau} + 0.5\left[\sigma^{(\alpha)}_{\tau\tau}\epsilon_{\tau\tau} + \sigma^{(\alpha)}_{zz}\epsilon_{zz} + \sigma_{nn}\frac{\nu}{1-\nu}(\epsilon_{\tau\tau}+\epsilon_{zz}) + \frac{E}{1-\nu^2}(\epsilon_{\tau\tau}+\nu\epsilon_{zz})u_{\tau\tau}\right] \\ + \quad & 0.5\left(-\frac{E}{1-\nu^2}(\epsilon_{\tau\tau}+\nu\epsilon_{zz})\epsilon_{\tau\tau} + \frac{E}{(1+\nu)(1-2\nu)}\left[-(1-\nu)\epsilon_{zz} - \nu\epsilon_{\tau\tau} + \frac{\nu^2}{1-\nu}(\epsilon_{\tau\tau}+\epsilon_{zz})\right]\epsilon_{zz}\right)^{***}\end{aligned} \tag{A.45}$$

where the terms in the brackets marked by $(***)$ equals

$$-\frac{E}{1-\nu^2}(\epsilon^2_{\tau\tau} + \epsilon^2_{zz} + 2\nu\epsilon_{zz}\epsilon_{\tau\tau}),$$

which yields

$$\begin{aligned}\tilde{F}_\alpha - \tilde{F}_\beta \quad = \quad & \sigma_{nn}\epsilon_{nn} + 2\sigma_{n\tau}\epsilon_{n\tau} + 0.5\left[\sigma^{(\alpha)}_{\tau\tau}\epsilon_{\tau\tau} + \sigma^{(\alpha)}_{zz}\epsilon_{zz} + \sigma_{nn}\frac{\nu}{1-\nu}(\epsilon_{\tau\tau}+\epsilon_{zz}) + \frac{E}{1-\nu^2}(\epsilon_{\tau\tau}+\nu\epsilon_{zz})u_{\tau\tau}\right] \\ - \quad & 0.5\frac{E}{1-\nu^2}(\epsilon^2_{\tau\tau} + \epsilon^2_{zz} + 2\nu\epsilon_{zz}\epsilon_{\tau\tau}).\end{aligned} \tag{A.46}$$

Using Hooke's law, we rewrite the stress tensor in terms of the strain tensor and obtain,

$$\begin{aligned} \tilde{F}_\alpha - \tilde{F}_\beta &+ 0.5\frac{E}{1-\nu^2}(\epsilon_{\tau\tau}^2 + \epsilon_{zz}^2 + 2\nu\epsilon_{zz}\epsilon_{\tau\tau}) = \\ \sigma_{nn}\epsilon_{nn} + 2\sigma_{n\tau}\epsilon_{n\tau} &+ 0.5\left[\sigma_{\tau\tau}^{(\alpha)}\epsilon_{\tau\tau} + \sigma_{zz}^{(\alpha)}\epsilon_{zz} + \sigma_{nn}\frac{\nu}{1-\nu}(\epsilon_{\tau\tau}+\epsilon_{zz}) + \frac{E}{1-\nu^2}(\epsilon_{\tau\tau}+\nu\epsilon_{zz})u_{\tau\tau}\right]. \end{aligned}$$

This does not really look better, but we need to find the representation of σ_{ik}^{ϵ} in terms of the lattice strains in this expression. For this purpose, we first have to blow up the notation, precisely

$$\begin{aligned} \tilde{F}_\alpha - \tilde{F}_\beta &+ 0.5\frac{E}{1-\nu^2}(\epsilon_{\tau\tau}^2 + \epsilon_{zz}^2 + 2\nu\epsilon_{zz}\epsilon_{\tau\tau}) = \\ \frac{E}{(1+\nu)(1-2\nu)}\left[(1-\nu)u_{nn} + \nu u_{\tau\tau}\right]\epsilon_{\tau\tau} &+ \frac{E}{2(1+\nu)(1-2\nu)}\left[(1-\nu)u_{\tau\tau} + \nu u_{nn}^{(\alpha)}\right]\epsilon_{\tau\tau} \\ + \frac{E}{2(1+\nu)(1-2\nu)}[\nu(u_{nn}^{(\alpha)} + u_{\tau\tau})]\epsilon_{zz} &+ \frac{E}{2(1+\nu)(1-2\nu)}\frac{\nu}{2(1-\nu)}[(1-\nu)u_{nn}^{(\alpha)} + \nu u_{\tau\tau}](\epsilon_{\tau\tau}+\epsilon_{zz}) \\ + \frac{E}{2(1+\nu)(1-2\nu)}\frac{1-2\nu}{2(1-\nu)}u_{\tau\tau}(\epsilon_{\tau\tau}+\nu\epsilon_{zz}) &+ 2\frac{E}{1+\nu}\epsilon_{n\tau}u_{n\tau}. \end{aligned}$$

We remember the definition of the lattice stresses σ_{ik}^{ϵ},

$$\sigma_{n\tau}^{\epsilon} = \frac{E}{1+\nu}\epsilon_{n\tau}, \tag{A.47}$$

$$\sigma_{\tau\tau}^{\epsilon} = \frac{E}{(1+\nu)(1-2\nu)}\left[(1-\nu)\epsilon_{\tau\tau} + \nu(\epsilon_{nn}+\epsilon_{zz})\right], \tag{A.48}$$

$$\sigma_{nn}^{\epsilon} = \frac{E}{(1+\nu)(1-2\nu)}\left[(1-\nu)\epsilon_{nn} + \nu(\epsilon_{\tau\tau}+\epsilon_{zz})\right], \tag{A.49}$$

to obtain

$$\begin{aligned} \tilde{F}_\alpha - \tilde{F}_\beta &+ 0.5\frac{E}{1-\nu^2}(\epsilon_{\tau\tau}^2 + \epsilon_{zz}^2 + 2\nu\epsilon_{zz}\epsilon_{\tau\tau}) = \\ 2\sigma_{n\tau}^{\epsilon}u_{n\tau} &+ \frac{E}{(1+\nu)(1-2\nu)}\left[u_{nn}((1-\nu)\epsilon_{nn} + 0.5\nu\epsilon_{\tau\tau} + 0.5\nu\epsilon_{zz} + 0.5\frac{\nu}{1-\nu}((1-\nu)(\epsilon_{\tau\tau}+\epsilon_{zz})))\right] \\ &+ \frac{E}{(1+\nu)(1-2\nu)}\left[u_{\tau\tau}\nu\epsilon_{nn} + 0.5(1-\nu)\epsilon_{\tau\tau} + 0.5\nu\epsilon_{zz} + 0.5\frac{\nu^2}{1-\nu}(\epsilon_{\tau\tau}+\epsilon_{zz}) + 0.5\frac{1-2\nu}{1-\nu}(\epsilon_{\tau\tau}+\nu\epsilon_{zz})\right], \end{aligned} \tag{A.50}$$

what we can express in a more comfortable way as

$$\tilde{F}_\alpha - \tilde{F}_\beta + 0.5\frac{E}{1-\nu^2}(\epsilon_{\tau\tau}^2 + \epsilon_{zz}^2 + 2\nu\epsilon_{zz}\epsilon_{\tau\tau}) = \sigma_{nn}^{\epsilon}u_{nn}^{(\alpha)} + \sigma_{\tau\tau}^{\epsilon}u_{\tau\tau} + 2\sigma_{n\tau}^{\epsilon}u_{n\tau}.$$

Consequently, the difference of the elastic contributions of the modified free energies reads as

$$\delta\tilde{F}^{el} = \sigma_{nn}^{\epsilon}u_{nn}^{(\alpha)} + \sigma_{\tau\tau}^{\epsilon}u_{\tau\tau} + 2\sigma_{n\tau}^{\epsilon}u_{n\tau} - 0.5\frac{E}{1-\nu^2}(\epsilon_{\tau\tau}^2 + \epsilon_{zz}^2 + 2\nu\epsilon_{zz}\epsilon_{\tau\tau}). \tag{A.51}$$

At this point, we achieved the desired representation $\delta\tilde{F}^{el}\left[u_{ik}^{(\alpha)}, \sigma_{ik}^{\epsilon}\right](x, y(x))$. The next step is the

transformation to cartesian coordinates. The corresponding expressions,

$$\begin{aligned}\epsilon_{nn} &= n_x^2\epsilon_{xx} + 2n_xn_y\epsilon_{xy} + n_y^2\epsilon_{yy},\\ \epsilon_{\tau\tau} &= n_y^2\epsilon_{xx} - 2n_xn_y\epsilon_{xy} + n_x^2\epsilon_{yy},\\ \epsilon_{n\tau} &= n_xn_y\epsilon_{xx} + 2(n_y^2 - n_x^2)\epsilon_{xy} - n_xn_y\epsilon_{yy},\end{aligned}$$

suggest the definition of the auxiliary functions

$$A(n_x, n_y) = n_y^2(\bar{\epsilon}_{xx} - \bar{\epsilon}_{yy}) - 2\bar{\epsilon}_{xy}n_xn_y \tag{A.52}$$

$$B = A^2 + 2\nu A\bar{\epsilon}_{zz} + 2A\bar{\epsilon}_{yy}, \tag{A.53}$$

where we define

$$\epsilon_{ik} = \epsilon\bar{\epsilon}_{ik},$$

such that ϵ denotes the magnitude of the lattice strain. Consequently, we write the difference of the chemical potential in the two phases as

$$\delta\tilde{F}^{el} = \sigma_{ik}^{\epsilon}u_{ik}^{(\alpha)} - \frac{E\epsilon^2}{2(1-\nu^2)}\left(B(\vec{x}) - (\bar{\epsilon}_{yy}^2 + \bar{\epsilon}_{zz}^2 + 2\nu\bar{\epsilon}_{yy}\bar{\epsilon}_{zz})\right), \tag{A.54}$$

which is just the required formulation which we use.

A.4 Numerical Implementation for the Coupled Elastic-Diffusional Solid-Solid Transition

In this chapter we will briefly describe the implementation of the governing equation for the elastic-diffusional problem which we treat in chapter 3. Apart from the implementation of the approximated governing equation, this section provides the explicit representation of the strains $u_{ik}^{(\alpha)}$ which we obtained in section 3.2.2. There we preferred a more compact style for a better overview, but the expressions we obtained need to be described in all detail. For the implementation of the approximated governing equation we use,

$$\begin{aligned}&-\sigma\kappa + \frac{T_{eq}c_p}{pL^2}\left[\sigma_{ik}^{\epsilon}u_{ik}^{(\alpha)} - \frac{E\epsilon^2B(\vec{x})}{2(1-\nu^2)}\right]\\ &= -\frac{1}{\pi}\int_{-\infty}^{\infty}dx'\log\left[\frac{(x-x')^2 + (y(x)-y(x'))^2}{(x-x')^2 + \left(-\frac{x^2}{2} + \frac{x'^2}{2}\right)^2}\right]^{1/2},\end{aligned} \tag{A.55}$$

where $d_0/pR = \sigma$, it is advantegeous to define the stresses σ_{ik}^{ϵ} and strains $u_{ik}^{(\alpha)}$ different, as a few prefactors will cancel. By B we define

$$B(\vec{x}) = B(n_x, n_y) = A^2 + 2\nu A\bar{\epsilon}_{zz} + 2A\bar{\epsilon}_{yy},$$

where the function A is defined as

$$A = n_y^2\left(\bar{\epsilon}_{xx} - \bar{\epsilon}_{yy}\right) - 2\bar{\epsilon}_{xy}n_xn_y.$$

For the strains σ^{ϵ}_{ik}, we introduce

$$\begin{aligned}
\epsilon_{ik} &= \epsilon\bar{\epsilon}_{ik} \\
\Sigma_{xx} &= \frac{1}{1-2\nu}((1-\nu)\bar{\epsilon}_{xx} + \nu(\bar{\epsilon}_{yy} + \bar{\epsilon}_{zz})) \\
\Sigma_{yy} &= \frac{1}{1-2\nu}((1-\nu)\bar{\epsilon}_{yy} + \nu(\bar{\epsilon}_{xx} + \bar{\epsilon}_{zz})) \\
\Sigma_{xy} &= \bar{\epsilon}_{xy},
\end{aligned}$$

where the Σ_{ik} and the stresses are related as

$$F_i = \sigma^{\epsilon}_{ik} n_k = \frac{E\epsilon}{1+\nu}\Sigma_{ik} n_k. \tag{A.56}$$

Consequently, we write the forces densities due to the eigenstrains as

$$\begin{aligned}
F_x &= \frac{E\epsilon}{1+\nu}(\Sigma_{xx} n_x + \Sigma_{xy} n_y) = \frac{E\epsilon}{1+\nu} f_x \\
F_y &= \frac{E\epsilon}{1+\nu}(\Sigma_{xy} n_x + \Sigma_{yy} n_y) = \frac{E\epsilon}{1+\nu} f_y,
\end{aligned}$$

where we also introduced f_x, f_y, which we use in Eqs. (A.57). The strains $u^{(\alpha)}_{ik}$ are eliminated in terms of the unknown interface $(x, y(x))$ as

$$\begin{aligned}
u_{xx} &= \frac{1+\nu}{4\pi(1-\nu)E}\int ds' \frac{1}{|\vec{r}-\vec{r}'|^4} \times \\
&\Big((F_x(x-x') + F_y(y-y'))((y-y')^2 - (x-x')^2) - 2(1-2\nu)|\vec{r}-\vec{r}'|^2 F_x(x-x')\Big)
\end{aligned}$$

$$\begin{aligned}
u_{yy} &= \frac{1+\nu}{4\pi(1-\nu)E}\int ds' \frac{1}{|\vec{r}-\vec{r}'|^4} \times \\
&\Big((F_x(x-x') + F_y(y-y'))((x-x')^2 - (y-y')^2) - 2(1-2\nu)|\vec{r}-\vec{r}'|^2 F_y(y-y')\Big)
\end{aligned}$$

$$\begin{aligned}
u_{xy} &= -\frac{1+\nu}{4\pi(1-\nu)E}\int ds' \frac{1}{|\vec{r}-\vec{r}'|^4} \times \\
&\Big(2(x-x')(y-y')(F_x(x-x') + F_y(y-y')) + (1-2\nu)|\vec{r}-\vec{r}'|^2(F_x(y-y') + F_y(x-x'))\Big),
\end{aligned}$$

and we introduce $I_{ik} = u_{ik}^{(\alpha)}/\epsilon$,

$$\begin{aligned}
I_{xx} &= \frac{1}{4\pi(1-\nu)} \int ds' \frac{1}{|\vec{r}-\vec{r}'|^4} \times \\
&\quad \Big((f_x(x-x') + f_y(y-y'))((y-y')^2 - (x-x')^2) - 2(1-2\nu)|\vec{r}-\vec{r}'|^2 f_x(x-x') \Big) \\
I_{yy} &= \frac{1}{4\pi(1-\nu)} \int ds' \frac{1}{|\vec{r}-\vec{r}'|^4} \times \\
&\quad \Big((f_x(x-x') + f_y(y-y'))((x-x')^2 - (y-y')^2) - 2(1-2\nu)|\vec{r}-\vec{r}'|^2 f_y(y-y') \Big) \\
I_{xy} &= -\frac{1}{4\pi(1-\nu)} \int ds' \frac{1}{|\vec{r}-\vec{r}'|^4} \times \\
&\quad \Big(2(x-x')(y-y')(f_x(x-x') + f_y(y-y')) + (1-2\nu)|\vec{r}-\vec{r}'|^2 (f_x(y-y') + f_y(x-x')). \Big)
\end{aligned}$$

The achieved notation for $\delta\tilde{F}^{el}$ thus reads as

$$\delta\tilde{F}^{el} = \frac{E\epsilon^2}{1+\nu}\Sigma_{ik}I_{ik} - \frac{E\epsilon^2}{2(1+\nu)(1-\nu)}\left(\bar{\epsilon}_{\tau\tau}^2 + \bar{\epsilon}_{zz}^2 + 2\nu\bar{\epsilon}_{zz}\bar{\epsilon}_{\tau\tau}\right), \tag{A.57}$$

and the representation in the code reads as

$$\frac{T_{eq}c_p}{pL^2}\delta\tilde{F}^{el} = \alpha\Sigma_{ik}I_{ik} - \alpha\frac{1}{2(1-\nu)}\left(\bar{\epsilon}_{\tau\tau}^2 + \bar{\epsilon}_{zz}^2 + 2\nu\bar{\epsilon}_{zz}\bar{\epsilon}_{\tau\tau}\right), \tag{A.58}$$

where

$$\alpha = \frac{T_{eq}c_pE\epsilon^2}{pL^2(1+\nu)}. \tag{A.59}$$

We remind us of the formal representation we choose for convenience in the discussion of the results. We define $\Phi = 2(1-\nu^2)/(E\epsilon^2(\bar{\epsilon}_{yy}^2 + \bar{\epsilon}_{zz}^2 + 2\nu\bar{\epsilon}_{yy}\bar{\epsilon}_{zz}))$ to obtain

$$\begin{aligned}
&- \quad \sigma\kappa + \frac{\Delta_{el}}{p}\Phi\left[\sigma_{ik}^{\epsilon}u_{ik}^{(\alpha)} - \frac{E\epsilon^2 B(\vec{x})}{2(1-\nu^2)}\right] \\
&= \quad -\frac{1}{\pi}\int_{-\infty}^{\infty} dx' \log\left[\frac{(x-x')^2 + (y(x)-y(x'))^2}{(x-x')^2 + \left(-\frac{x^2}{2} + \frac{x'^2}{2}\right)^2}\right]^{1/2}.
\end{aligned} \tag{A.60}$$

B Acknowledgements

First, I thank Prof. Dr. Heiner Müller-Krumbhaar for the fascinating topic and providing an excellent research environment. Advice and support in all concerns greatly helped and motivated me. I profited from his long experience not only in this specific field of science, and I thank him for the fruitful discussions.

Next, I would like to express my gratitude to Dr. Efim Brener. His intuition for the most essential aspects of the considered systems is unparalleled. He constantly supported me and teached me what thoroughness and perseverance in science mean. I greatly benefit from his clear and efficient approach to scientific problems.

I thank Prof. Dr. Walter Selke for agreeing to be the second referee of this thesis.

I have the pleasure of thanking a large group of colleagues of the IFF theoretical institutes for rendering such a pleasant atmosphere and various soccer games. In particular I thank Dr. Phivos Mavropoulos, Dr. Marjana Lezaic and Dr. Yuriy Mokrousov - I enjoyed the late trips home when the discussions were very entertaining. Also I thank Dr. Theo Costi for his very helpful offer to put corrections on the manuscript and Dr. Herbert Schober for his sense of irony which rendered discussions very enjoyable. The expertise of the technical staff left no problem unsolved.

I thank Dr. Clemens Gugenberger who teached me efficient ways of programming. I took great advantage of his comprising computational and numerical expertise and he always had an open door for my questions. Apart from that, he greatly helped me with the corrections on this manuscript, and I consider myself lucky to enjoy our friendship.

I thank my friend and colleague Michael Fleck, with whom I shared the office and many scientific and non-scientific discussions which I greatly appreciated. I owe him to a major part enjoying the working atmosphere, and he also helped me with the manuscript.

I thank Dr. Guillaume Boussinot. His enthusiasm for new physical problems is infectious and I really enjoy our discussions.

I thank Dr. Denis Pilipenko who has a large numerical expertise and who discussed with me important numerical issues.

I would like to thank Luise Snyders who is the heart of the institute for her organizational help.

I thank my girlfriend Julia Acker. I deeply enjoy our relationship and appreciate our common views on fundamental issues of life and her ability to see through me.

My very best thanks go to my family. They have supported me in all concerns over the entire studies and always made me clear what is really important. I dedicate this thesis to my parents Annegret and Friedhelm and my sister Meike.

C Publications

Parts of this thesis are published in the following journals:

- E. A. Brener, C. Hüter, D. Pilipenko, D. E. Temkin, Velocity Selection Problem in the Presence of the Triple Junction, Phys. Rev. Lett. 99, 105701 (2007). (Chapter 4)
- D. Pilipenko, E. A. Brener and C. Hüter, Theory of dendritic growth in the presence of lattice strain, Phys. Rev. E 78, 060603 (2008). (Chapter 3)
- E. A. Brener, G. Boussinot, C. Hüter, M. Fleck, D. Pilipenko, R. Spatschek and D. E. Temkin, Pattern formation during diffusional transformations in the presence of triple junctions and elastic effects, J. Phys. Condens. Matter 21, 464106 (2009) (Chapter 3 and 4)
- M. Fleck, C. Hüter, D. Pilipenko, R. Spatschek and E. A. Brener, Pattern formation during diffusion limited transformations in solids, Philosophical Magazine 90, 265-286 (2010). (Chapter 3)
- E. A. Brener, M. Fleck, C. Hüter, H. Müller-Krumbhaar, D. Pilipenko, D. E. Temkin and R. Spatschek, Pattern Formation: From the Macro- to the Nanoscale, NIC Symposium 3, 183-190 (2010) (Chapter 4)

Curriculum Vitae

Name: Claas Hüter

Date of birth May 27th, 1980
Place of birth Düsseldorf, Germany
Nationality German
Address: Institut für Festkörperforschung
Forschungszentrum Jülich
Leo-Brandt-Straße
52025 Jülich
Germany
e-mail: maryjaneparker@gmx.net

Education:

03/2007 – 03/2010	Dissertation in condensed matter physics: Pattern formation during diffusional transformations in the presence of triple junctions and lattice strain: Green's function methods Supervisor: Prof. Dr. Heiner Müller-Krumbhaar Research Conducted at the Institut für Festkörperforschung Forschungszentrum Jülich, Germany Dissertation submitted at the RWTH Aachen University, Germany
10/2005 – 10/2006	Diploma in condensed matter physics: Diffusion-limited propagation of a melting zone along a grain boundary Supervisor: Prof. Dr. Heiner Müller-Krumbhaar Institut für Festkörperforschung Forschungszentrum Jülich, Germany
10/2000 – 12/2006	Studying physics at the RWTH Aachen University, Germany
08/1999 – 08/2000	Civil service at the geriatric psychiatry, Rheinische Landeskliniken Süchteln, Germany
06/1999	Abitur at the Erasmus-von-Rotterdam Gymnasium Viersen, Germany